

Coherent production of neutral pions on ^{12}C and ^{40}Ca

PhD thesis

Lotte S. Fog*

Nuclear Physics Group

Department of Physics and Astronomy

University of Glasgow

© Lotte S. Fog 2001

November 22, 2001

*Email: lottef@physics.gla.ac.uk

ProQuest Number: 13818889

All rights reserved

INFORMATION TO ALL USERS

The quality of this reproduction is dependent upon the quality of the copy submitted.

In the unlikely event that the author did not send a complete manuscript and there are missing pages, these will be noted. Also, if material had to be removed, a note will indicate the deletion.



ProQuest 13818889

Published by ProQuest LLC (2018). Copyright of the Dissertation is held by the Author.

All rights reserved.

This work is protected against unauthorized copying under Title 17, United States Code
Microform Edition © ProQuest LLC.

ProQuest LLC.
789 East Eisenhower Parkway
P.O. Box 1346
Ann Arbor, MI 48106 – 1346

GLASGOW
UNIVERSITY
LIBRARY:

12404
COPY 1

Abstract

Neutral pion photo-production is a useful tool to investigate several aspects of nuclear physics. Information can be extracted on the matter distribution, the pion-nucleus interaction and the medium modifications of the pion production process. In the present experiment, neutral pions were produced on ^{12}C and ^{40}Ca at the tagged photon facility at MAMI. The pion decay photons were detected using the detector array TAPS, a highly segmented detector array built to detect light mesons.

The differential and integrated cross sections for coherent photo-production of neutral pions from ^{12}C and ^{40}Ca were measured in the incident photon energy range 135-380 MeV. The diffraction-like pattern of the differential cross section was demonstrated. Comparisons with the plane and distorted wave impulse approximation models show the importance of including a description of the final state interactions in the theoretical models but suggest that the magnitude of the pion-nucleus interaction is underestimated in the DWIA model. Comparisons with the recent delta resonance energy model suggest that modifications of the process due to changes to the properties of the Δ in the nuclear medium were present but that modifications are needed to the parameterisation of the Δ properties used in the DREN model.

Acknowledgements

I would like to thank my supervisors, Prof. R. O. Owens, for his efforts and for teaching me a lot about supervision, and Dr. J. C. McGeorge, for his support and continuous help throughout the project. Without him, this thesis would not have been finished.

I am also grateful to:

Ruth and Andi, for their friendship and for lots of help with annoying things in the analysis,

the other members of the Glasgow experimental nuclear physics group, for help with lots of things and for friendship in the past four years,

Andrew Long, for interfering,

Marco, Martin and the other collaborators in Gießen and in Mainz, for their efforts before and during the experiment and in Glasgows' pubs,

the staff at MAMI, for providing the facilities for the experiment,

my parents, for their support,

Mark, and good friends in Edinburgh, for trying to keep me sane for the duration of this project, and

EPSRC, for funding my tuition fees.

Declaration

The data presented in this thesis were obtained in collaboration with colleagues from Institut für Kernphysik, Mainz, II Physikalisches Institut, Gießen and the nuclear structure group, Glasgow University. This thesis is my own work.

Lotte S. Fog

Contents

1	Introduction	12
2	Theory	16
2.1	Pions	16
2.2	Neutral pion production on a nucleon	17
2.3	Neutral pion production on a nucleus	18
2.4	The plane wave impulse approximation	20
2.5	The distorted wave impulse approximation	21
2.6	The delta resonance energy model	22
3	The experiment	27
3.1	MAMI	28
3.2	The photon tagger	30
3.3	The targets	31
3.4	TAPS	32
3.5	The NaI detectors	36
3.6	Detector read-out	36
3.7	Execution of the experiment	38
4	Data analysis	39
4.1	Steps of the analysis	39
4.2	Calibration of the detectors	40
4.2.1	Energy calibrations	40
4.2.2	Changes in the energy calibration during the data runs	42
4.2.3	Time alignment	42
4.3	Identification of photons	43
4.3.1	Pulse shape analysis	43
4.3.2	The CPV detectors I	48
4.3.3	Selection of clusters	50

4.4	Cluster properties	51
4.4.1	Methods of cluster position reconstruction	51
4.4.2	Correction to the position reconstruction	60
4.5	Selection of pions	62
4.5.1	Pion kinematics and missing energy	62
4.5.2	The CPV detectors II	64
4.5.3	Selection of pions	67
4.5.4	Selection of coherent events	72
4.6	The maximum likelihood method	81
4.7	TAPS detection efficiency	86
4.8	Cross sections	89
4.9	Errors in the cross sections	90
4.10	Data from the NaI detectors	93
5	Results and discussion	97
5.1	^{40}Ca	97
5.1.1	Comparison with other experimental data	98
5.1.2	Comparison with theoretical models	99
5.1.3	The nuclear excitation process	102
5.2	^{12}C	117
5.2.1	Comparison with other experimental data	117
5.2.2	Comparison with theoretical models	118
5.2.3	The nuclear excitation process	119
5.3	Conclusion	136
A	Tables of cross sections	138
B	Derivation of formulae	146
B.1	The reconstructed pion mass	146
B.2	The X formula	147

List of Figures

1	Feynman diagrams contributing to neutral pion production	17
2	The form factors used in the theoretical calculations	19
3	The π^-p cross section	21
4	Schematic diagram of the interactions included in the delta resonance energy model.	23
5	Theoretical calculations of σ for ^{40}Ca	24
6	Theoretical calculations of $\frac{d\sigma}{d\Omega}$ for $E_\gamma = 200$ MeV for ^{40}Ca	25
7	Theoretical calculations of $\frac{d\sigma}{d\Omega}$ for $E_\gamma = 350$ MeV for ^{40}Ca	26
8	Experimental set-up	27
9	MAMI lay-out	29
10	A TAPS element	33
11	A TAPS block (schematic)	34
12	The forward wall (schematic)	34
13	TAPS set-up (schematic)	35
14	TAPS read-out	37
15	A TAPS cosmic muon energy deposition spectrum	41
16	A TAPS wide versus narrow gate energy spectrum	44
17	Spectrum of PSA radius versus PSA angle	46
18	Spectrum of PSA radius versus PSA angle projected onto the angle-axis	47
19	Veto detector pattern for ^{12}C data for blocks A-F	49
20	Veto detector pattern for ^{12}C data for the FW	49
21	Numbering used in frac methods of position reconstruction	52
22	Distribution of reconstructed positions in element D54 for various methods of position reconstruction	55
23	Spectrum of average reconstructed versus simulated entry point for various methods of position reconstruction	55
24	Reconstructed pion mass spectrum for various methods of position reconstruction	56

25	Reconstructed pion mass spectrum for various ways of using the logarithmic position reconstruction method	58
26	Reconstructed pion mass using various ways of implementing various logarithmic position reconstruction methods	59
27	A TAPS block (schematic) with the coordinate system used to correct the reconstructed cluster position	61
28	Missing energy distribution for the ^{12}C data	63
29	The effect of using the CPV detectors on the pion missing energy distribution	66
30	Spectrum of the reconstructed pion mass for ^{12}C	68
31	Spectrum of the reconstructed pion mass for ^{40}Ca	69
32	Spectrum of the time difference between the two pion decay photons for ^{12}C .	70
33	Spectrum of the time difference between the tagging electron and TAPS trigger for ^{12}C	71
34	Spectrum of the missing energy resolution for ^{12}C	72
35	Missing energy spectrum for ^{12}C for $30 < \theta_\pi < 35^\circ$ and $150 < E_\gamma < 155$ MeV.	75
36	Missing energy spectrum for ^{12}C for $30 < \theta_\pi < 35^\circ$ and $220 < E_\gamma < 240$ MeV.	76
37	Missing energy spectrum for ^{12}C for $50 < \theta_\pi < 55^\circ$ and $320 < E_\gamma < 340$ MeV.	77
38	Missing energy spectrum for ^{12}C for $90 < \theta_\pi < 95^\circ$ and $320 < E_\gamma < 340$ MeV.	78
39	Apparent peak position of the missing energy distribution for ^{12}C	79
40	Flow diagram of the Maximum Likelihood Method	83
41	Reconstructed pion mass using the X formula and the MLM	84
42	Missing energy distribution using the X formula and the MLM	85
43	Reconstructed pion mass - simulation compared with data for ^{12}C	87
44	Plot of TAPS detection efficiency for neutral pions for various pion lab angles for ^{12}C	88

45	Plot of TAPS detection efficiency for neutral pions for various incident photon energies for ^{12}C	88
46	NaI Time spectrum for ^{12}C	93
47	NaI Energy spectrum for ^{12}C	94
48	NaI Energy spectrum for ^{40}Ca	95
49	Differential cross sections for ^{40}Ca for $135 < E_\gamma < 155$ MeV	106
50	Differential cross sections for ^{40}Ca for $155 < E_\gamma < 190$ MeV	107
51	Differential cross sections for ^{40}Ca for $190 < E_\gamma < 260$ MeV	108
52	Differential cross sections for ^{40}Ca for $260 < E_\gamma < 340$ MeV	109
53	Differential cross sections for ^{40}Ca for $340 < E_\gamma < 380$ MeV	110
54	Differential cross section for ^{40}Ca at $E_\gamma = 200$ MeV	111
55	Differential cross section for ^{40}Ca at $E_\gamma = 290$ MeV	112
56	Differential cross section for ^{40}Ca at $E_\gamma = 350$ MeV	113
57	Differential cross section for ^{40}Ca at $160 < E_\gamma < 170$ MeV	114
58	Integrated cross section for ^{40}Ca	115
59	Integrated cross section for ^{40}Ca	116
60	Differential cross sections for ^{12}C for $135 < E_\gamma < 155$ MeV	123
61	Differential cross sections for ^{12}C for $155 < E_\gamma < 190$ MeV	124
62	Differential cross sections for ^{12}C for $190 < E_\gamma < 260$ MeV	125
63	Differential cross sections for ^{12}C for $260 < E_\gamma < 340$ MeV	126
64	Differential cross sections for ^{12}C for $340 < E_\gamma < 380$ MeV	127
65	Differential cross section for ^{12}C at $E_\gamma = 200$ MeV	128
66	Differential cross section for ^{12}C at $E_\gamma = 290$ MeV	129
67	Differential cross section for ^{12}C at $E_\gamma = 350$ MeV	130
68	Differential cross sections for ^{12}C at $\theta_\pi = 60^\circ$	131
69	Integrated cross section for ^{12}C	132
70	Integrated cross section for ^{12}C	133
71	An estimate of the upper limit to the differential cross section for non-coherent nuclear excitation 4.4 MeV events for ^{12}C	134

List of Tables

1	MAMI data	28
2	Target data	31
3	BaF ₂ data	32
4	TAPS set-up details	33
5	NaI data	36
6	Some of the cuts applied to select pions	67
7	Processes contributing to π^0 -production.	73
8	Fit methods used to fit E_{miss} distributions	80
9	Estimate of the systematic error in the fit to the missing energy distribution	92
10	Positions of the first maximum and minimum in the differential cross section for ^{40}Ca	103
11	Positions of the second maximum and minimum in the differential cross section for ^{40}Ca	104
12	Positions of the third maximum and minimum in the differential cross section for ^{40}Ca	105
13	Positions of the first maximum and minimum in the differential cross section for ^{12}C	121
14	Positions of the second maximum and minimum in the differential cross section for ^{12}C	122
15	$^{12}\text{C} \frac{d\sigma}{d\Omega}$	139
16	$^{12}\text{C} \frac{d\sigma}{d\Omega}$	140
17	$^{12}\text{C} \frac{d\sigma}{d\Omega}$	141
18	$^{40}\text{Ca} \frac{d\sigma}{d\Omega}$	142
19	$^{40}\text{Ca} \frac{d\sigma}{d\Omega}$	143
20	$^{40}\text{Ca} \frac{d\sigma}{d\Omega}$	144

21 Integrated cross sections for ^{12}C and ^{40}Ca 145

1 Introduction

Photo-production of neutral pions is a useful tool for studying several aspects of nuclear physics. Information can be obtained on the matter distribution of the nucleus, on the medium modifications of the pion production process inside the nucleus and on the interactions between the pion and the nucleus (the final state interactions).

Investigating the reaction where the nucleus is left in its ground state after the interaction (the coherent reaction) is particularly interesting as the production amplitudes from all the nucleons add coherently and the theoretical description simplifies. The information on the nuclear matter distribution complements the already existing data from electron scattering [1]: whereas the electron interacts mostly with the protons in the nucleus and information about the charge distribution can be extracted from electron scattering experiments, the pion photo-production process occurs on all the nucleons, allowing information on the matter distribution to be extracted from neutral pion production experiments.

Several theoretical descriptions of the neutral pion photo-production process exist in the literature. The plane wave impulse approximation (PWIA) describes the reaction neglecting the medium modifications of the production process, multiple interactions inside the nucleus and the final state interactions, treating the production process on the nucleus simply as the sum of the production amplitudes on the individual nucleons. It assumes that the wavefunction of the pion is a plane wave. More sophisticated treatments exist in the distorted wave impulse approximation (DWIA) [2], where the final state interactions are described phenomenologically, and the Δ -hole model [3], which attempts to describe the medium modifications. A more recent model, the delta resonance energy model (DREN) [2], includes descriptions of the medium modifications, multiple interactions and the final state interactions. Data from the present experiment are compared with theoretical predictions from the plane and distorted wave impulse approximations and from the delta resonance energy model.

Relatively few attempts have been made to measure the coherent neutral pion production cross section. This is because the required high duty factor source of monochromatic or tagged photons and the pion detector array needed to perform comprehensive exper-

iments are both large scale technical developments. Both these areas have seen major developments over the past ten years. Several high-duty factor electron accelerators at energies in the range 100 MeV-10 GeV are now in operation around the world and several of these have been equipped to produce tagged photon beams with good energy resolution.

Since neutral pions must be observed via their decay photons, the technical problem is that of assembling a sufficiently large array of individual photon detectors with sufficiently good energy and position resolution so the pion decay photons can be observed with high efficiency and the pion momentum can be reconstructed from the photon momenta. It is only in the last few years that highly segmented arrays of scintillators suitable for this purpose have become available.

The first measurements of the neutral pion production reaction were made by Schrack et al. [4] in 1962. These measurements used the photon beam from a 170 MeV electron synchrotron and no attempt was made to determine the energy of the photons. The total pion production yield due to all photon energies above the pion production threshold was measured. The photon detectors used plastic scintillators to observe the electron-positron pairs produced in thin lead converters. This gave no information on the pion energy and the angular resolution was approximately 20° FWHM. Nevertheless, Schrack et al. observed clear signs of the diffraction structure in the neutral pion angular distributions using targets of Cu, Cd and Pb.

Limited data on neutral pion production on ^4He in the Δ resonance region was obtained by detecting the α particle by Lefrançois et al. [5]. The incident photon energy dependence of the neutral pion production cross section for pion lab angles below 10° was measured by Bellinghausen et. al. [6] [7] and Belousov et. al. [8].

A series of measurements of the integrated π^0 -production cross section in the threshold region was carried out in the 1980's by Argan et al. [9], Glavanakov et al. [10], Mazzucato et al. [11] and Jammes et al. [12]. Because the non-coherent cross section is expected to be small in the threshold region, these measurements could be carried out with relatively simple detectors which did not determine the energy of the pion. Typically, lead-glass Cherenkov detectors positioned closely around the target detected the pion decay photons

in coincidence. Measurements were made on several light nuclei (the heaviest target nucleus was ^{40}Ca) and the results confirmed the importance of the pion-nucleus interaction as the measurements were typically 20 % larger than the values predicted from the PWIA.

In the measurement by Jammes et al. [12], the integrated cross section was measured for incident photon energies up to 170 MeV. However, as no attempt was made to separate the coherent and non-coherent cross sections, the contribution of the non-coherent processes to the cross section for incident photon energies above about 160 MeV meant that the results for higher incident photon energies were of limited use.

At higher incident photon energies, a separation of coherent and non-coherent events in the experimental data is essential to obtain results which can be compared with theoretical predictions. ^4He has no excited nuclear states. Measurements of π^0 production on helium were carried out by Tieger et al. [13], using untagged bremsstrahlung, and Bellini et al. [14], relying on a pion detector with poor energy resolution. The results from these measurements are in agreement with more recent results by Rambo et al. [15] using the tagged photon beam at Mainz and the TAPS (Two Arm Photon Spectrometer) photon detector array.

TAPS, a highly segmented array of BaF_2 elements, is the best π^0 detector available in Europe at the present time. The measurements on helium were made in the incident photon energy range 200-400 MeV and for all pion lab angles, and the results were used to fix the parameterisation of the Δ -nucleus interaction used in the DREN model [2]. Because ^4He is an atypical nuclear system, this parameterisation may require modification if the model is used to account for results on other nuclei.

For $A > 4$ nuclei, relatively few measurements of differential cross sections of neutral pion production have been carried out. Arends et. al. [16] measured differential cross sections on ^{12}C using a 500 MeV synchrotron, but did not attempt to separate coherent and non-coherent events.

Differential cross sections for ^{12}C and ^{40}Ca for incident photon energies of 158-168 MeV and integrated cross sections for ^{12}C for incident photon energies from threshold to 168 MeV, were measured by Koch et al. [17] [18] using lead-glass detectors. The

energy resolution of the lead-glass detectors was relatively poor and separation between coherent and non-coherent events could not be achieved by selecting the energy difference between the incident photon and the pion. This separation was attempted by selecting events according to the opening angle of the two pion decay photons. While this method allowed the coherent cross section to be estimated, it implied a reduction in the number of detected events by approximately a factor of 10, introducing significant statistical errors in the cross section.

Schmitz [19] measured the integrated cross sections for ^{12}C , using BaF_2 and NaI detectors to detect the two pion decay photons. However, whereas the energy resolution obtained in this experiment was significantly better than the resolution in the experiment of Koch et al., allowing for a separation of coherent and non-coherent events, data was obtained for only one value of the pion lab angle, $\theta_\pi = (60 \pm 10)^\circ$.

More recently, TAPS, a detector array consisting of many individual BaF_2 elements, has become available. The first data on π^0 photo-production on ^{12}C and ^{40}Ca using TAPS was obtained by Krusche [20]. Differential cross sections were measured, using 320 TAPS elements, for the energy range 200-390 MeV but no measurements were made close to threshold.

The present data, also obtained using TAPS, represents the first complete measurement of differential and integrated cross sections for ^{12}C and ^{40}Ca in the incident photon energy range 135 - 380 MeV. For the present experiment, TAPS consisted of 526 BaF_2 elements, covering a wider angular range than that obtained in [20]. As was the case in [20], separation of coherent and non-coherent events was attempted by a comparison between the incident photon energy and the total pion energy.

2 Theory

This chapter provides a very general introduction to pions and a brief description of some of the models used to describe pion production. interaction must be introduced into the calculation.

2.1 Pions

The pion was proposed by Yukawa [21] in 1935. It was then known that the photon was the exchange particle of the electro-magnetic force, and Yukawa described a particle which would be the exchange particle of the strong nuclear force in a similar way. Just as virtual photons are exchanged between charged particles interacting electro-magnetically, virtual pions would be exchanged between nucleons interacting via the strong nuclear force.

One difference is that the electro-magnetic force has infinite range, whereas the strong nuclear force was known to have a range of a few fermi. Hence, where the photon is massless, the pion would have finite mass. Using the relationships:

$$\hbar = \delta E \delta t , \quad (1)$$

$$\hbar c \approx 200 \text{MeV}/c^2 \quad (2)$$

and

$$\delta E = m_x c^2 \quad (3)$$

where \hbar is Planck's constant divided by 2π , δE the energy exchanged in time δt , m_x the mass of the exchanged particle and c the speed of light, an estimate of the maximum distance δx the exchanged particle can travel in time δt is:

$$\delta x = c \delta t = c \frac{\hbar}{\Delta E} = \frac{c \hbar}{m_x c^2} \approx \frac{200 \text{MeV}}{m_x c^2} \quad (4)$$

If the distance traveled by the exchanged particle is 1 fm, its mass is approximately 200 MeV/ c^2 .

Yukawa named this particle the meson ('meso' means middle in Greek, as its mass is between that of leptons and baryons).

There are several kinds of meson (π, ρ, ω, \dots). The pi meson, or pion, is the lightest meson and is the main exchange particle between neighbouring nucleons. The heavier mesons are involved in the exchange of the strong nuclear force at shorter range.

There are three kinds of pion (π^-, π^0 and π^+) with charges $-e, 0$ and e , where e is the charge of the electron. The lifetime of the π^0 is $8.4 \cdot 10^{-17}$ s and its main decay channel (branching ratio 98.798 %) is to two photons.

2.2 Neutral pion production on a nucleon

The main Feynman diagrams contributing to coherent neutral pion photo-production on a nucleon are shown in fig. 1.

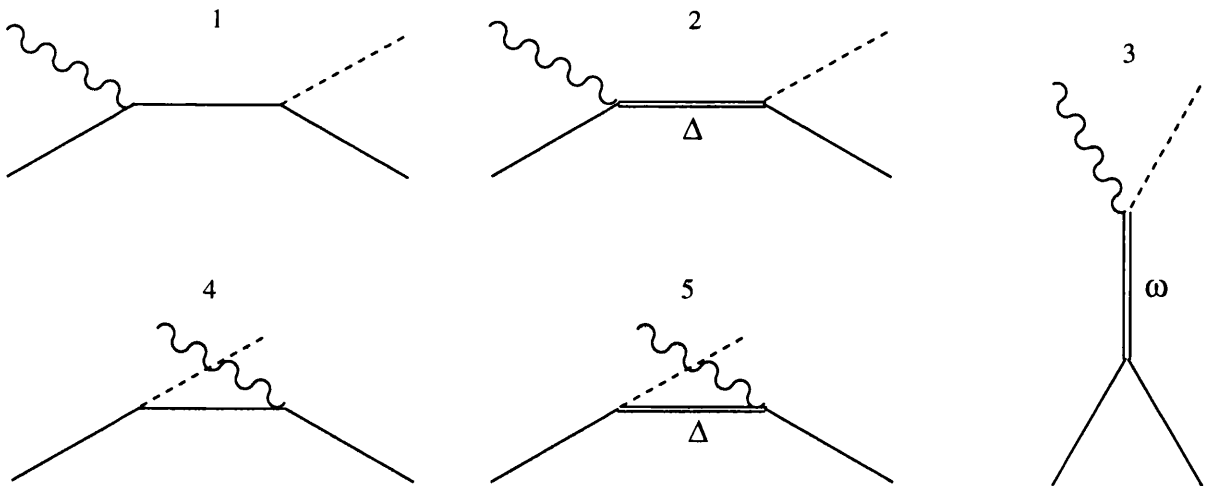


Figure 1: The main Feynman diagrams contributing to neutral pion production on a nucleon.

It can be shown that the neutral pion production amplitudes due to the processes shown in diagrams 1 and 4 in fig. 1 almost cancel [22]. The mass of the Δ is 1232 MeV, about 300 MeV greater than that of the proton and the neutron. As the pion is emitted before the photon is absorbed in the process shown in diagram 5, requiring the Δ particle

to be more than 400 MeV off its mass shell, the contribution due to this process is very small. As the mass of the ω (782 MeV) is much greater than the energy available in the present experiment, the contribution to the production process due to diagram 3 is also very small.

The production process is therefore dominated by the process shown in diagram 2 at all incident photon energies except very close to the π^0 production threshold. As the spin of the Δ is $\frac{3}{2}$, the pion must have an orbital angular momentum of $1\hbar$ in the process shown in diagram 2. Close to threshold, there is not enough available energy for the pion to have an orbital angular momentum, hence the contribution due to diagram 2 vanishes [22] and the cross section is determined by the other processes shown in fig. 1.

A recently developed model describing the pion production on a nucleon, the unitary isobar model (UIM) [2], describes the π^0 production process including both the diagrams shown in fig. 2 and processes involving higher resonances (N^* etc). The models described in sections 2.4 - 2.6 use the UIM to describe the neutral pion production process.

2.3 Neutral pion production on a nucleus

The production amplitudes on the individual nucleons must be combined to obtain the production amplitude on the nucleus. When the initial and final states of the nucleus are identical, the production amplitude on the nucleus can be written as a coherent sum of the production amplitudes on the nucleons - this reaction is therefore called the coherent reaction. However, there is a phase difference due to the different positions of the nucleons inside the nucleus. The production amplitude on the nucleus is proportional to the square of the nuclear matter form factor, F , in the same way as the electron scattering amplitude on a nucleus is proportional to the square of the electric form factor. The form factors used in the theoretical models compared with the present result are shown as a function of the momentum transfer from the photon to the nucleus, q , in fig. 2. They are based on the assumption that the matter distribution has the same shape as the charge distribution.

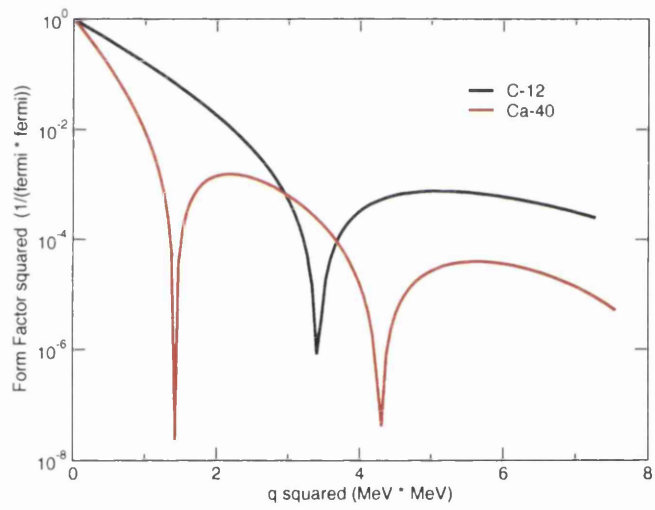


Figure 2: The matter form factors used in the theoretical calculations [23] used in this work.

2.4 The plane wave impulse approximation

The plane wave impulse approximation (PWIA) is a very simple approximation used to describe neutral pion production. In the PWIA it is assumed that the incident photon only interacts with one nucleon and that there is no interaction between the pion and the nucleus so that the wavefunction of the pion can be described as a plane wave.

The coherent cross section obtained using the PWIA is:

$$\frac{d\sigma_{PWIA}}{d\Omega}(E_\gamma, \theta_\pi^*) = \frac{s}{m_N^2} A^2 F^2(q) \frac{d\sigma_E}{d\Omega}(E_\gamma^*, \theta_\pi^{**}) \quad (5)$$

where E_γ is the incident photon energy, θ_π^* is the pion polar angle in the photon-nucleus centre-of-mass frame, s the square of the total energy of the photon-nucleon pair, m_N the nucleon mass, A the atomic mass number, F the nuclear matter form factor, q the momentum transfer from the photon to the nucleus, E_γ^* the photon energy and θ_π^{**} the pion angle in the photon-nucleon centre-of-mass frame and $\frac{d\sigma_E}{d\Omega}$ the elementary cross section.

For spin-zero nuclei, the initial and final state of the nucleus is 0^+ , hence spin-flip processes can not contribute. Only spin-independent processes contribute and the elementary cross section $\frac{d\sigma_E}{d\Omega}$ can be written as:

$$\frac{d\sigma_E}{d\Omega}(E_\gamma^*, \theta_\pi^{**}) = \frac{k'}{2k} |f_2(E_\gamma^*, \theta_\pi^{**})|^2 \sin^2(\theta_\pi^{**}) \quad (6)$$

where k' and k are the momenta of the pion and the photon in the pion-nucleon centre-of-mass system and f_2 is the Chew-Goldberger-Low-Nambu (CGLN) amplitude (see [2] for details).

The PWIA describes all the basic characteristics of the cross section: its magnitude is proportional to the square of the number of nucleons, and the shape of the differential cross section is described by the square of the form factor and modulated by the $\sin^2(\theta_\pi^{**})$ term. These features have been shown to have some validity in existing data [20].

The PWIA does not include a description of the interaction between the pion and the nucleus as the pion travels away from the nucleus (the final state interaction, or FSI).

The PWIA is therefore not expected to give a detailed description of the reaction, as the pion interacts strongly with the nucleus.

2.5 The distorted wave impulse approximation

The DWIA (Distorted Wave Impulse Approximation) includes a description of the FSI. Fig. 3 shows the (π^-p) cross section. Although the process discussed in the present work involves a π^0 and not a π^- , qualitatively the strength of the interaction between the pion and the nucleons is expected to be similar to that shown in fig. 3. For pion energies up to about 50 MeV, or incident photon energies up to about 180 MeV, the interaction between the pion and the nucleus is not very strong and can be accounted for by treating it as a mean field in which the motion of the pion can be calculated. For pion energies above about 50 MeV, however, the interaction is too strong for this approximation to be valid and the Δ which is created in the interaction must be introduced into the calculation.

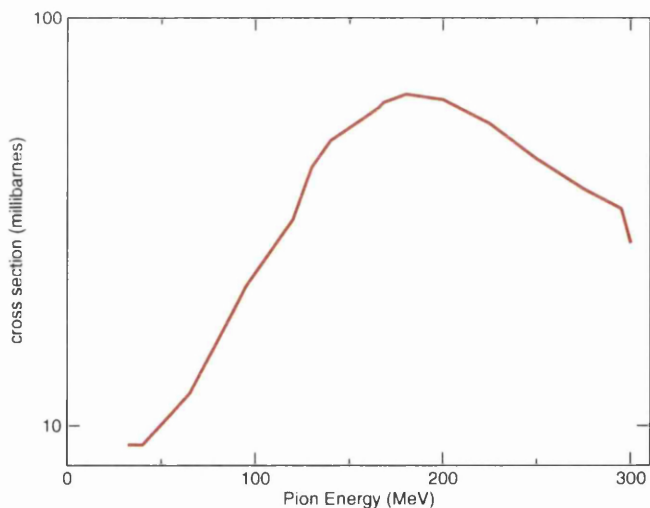


Figure 3: Theoretical prediction for the π^-p cross section. Fig. from [24]

Older calculations [25] parameterised the pion-nucleus interaction using an optical potential and then solved the Klein-Gordon equation in position coordinate space to obtain the distorted wavefunction of the pion. More recent calculations [26] [27] are carried out in momentum space. This has two advantages: the Fermi motion of the

nucleons inside the nucleus can be taken into account and the distortion of the pion wavefunction can be related directly to the pion-nucleus interaction.

The cross section from the DWIA is greater than that from the PWIA just above threshold but then decreases at higher incident photon energy due to absorption of the pion. The maxima and minima are shifted towards smaller pion lab angles. Because the pion-nucleus potential is attractive, the pion momentum is larger just after the pion has been produced than after it has left the nucleus. It is the value of the momentum transfer at the interaction point which is relevant when evaluating the nuclear matter form factor. Since the momentum transfer increases with pion lab angle, a particular value of the form factor is reached at a smaller pion angle when the effect of the attractive pion-nucleus interaction is included in the description of the process (see fig. 2).

2.6 The delta resonance energy model

In the DWIA, it is assumed that the pion is produced on one nucleon and that the effect of the other nucleons can be described as a mean field in which the pion production takes place.

The properties of the Δ particle which takes part in the production process are assumed to be the same as those of a free Δ particle. However, the Δ particle interacts strongly with the other nucleons inside the nucleus. In the Δ -hole model [28], modifications of the properties of the Δ particle have been taken into account using a complex potential to parameterise the interaction of the Δ -hole (the Δ and the missing nucleon) with the nucleus. The Δ -hole model has been used with some success to treat pion and photon induced nuclear reactions at Δ excitation energies. The Δ -hole model predicts that the peak of the cross section for pion photo-production will be shifted down from the Δ -peak and that the peak cross section will be reduced compared with the DWIA calculation.

A recent model, the delta resonance energy (DREN) model, takes final state interactions, multiple interactions inside the nucleus and Δ medium modifications into account. A description of the processes where the Δ decays to a nucleon and a pion inside the nu-

cleus, and the pion then produces another delta on a nucleon, and so on, is included. This reaction is shown in fig. 4. The interaction between the Δ and the nucleus is described as in ref. [28] using a complex Δ self-energy which modifies the effective mass of the Δ . A single parameterisation of the Δ self-energy is assumed to be suitable for calculations on all nuclei. The parameters used to calculate the results from the DREN theory presented in this work were obtained by fitting data on the ${}^4\text{He}(\gamma, \pi^0)$ reaction.

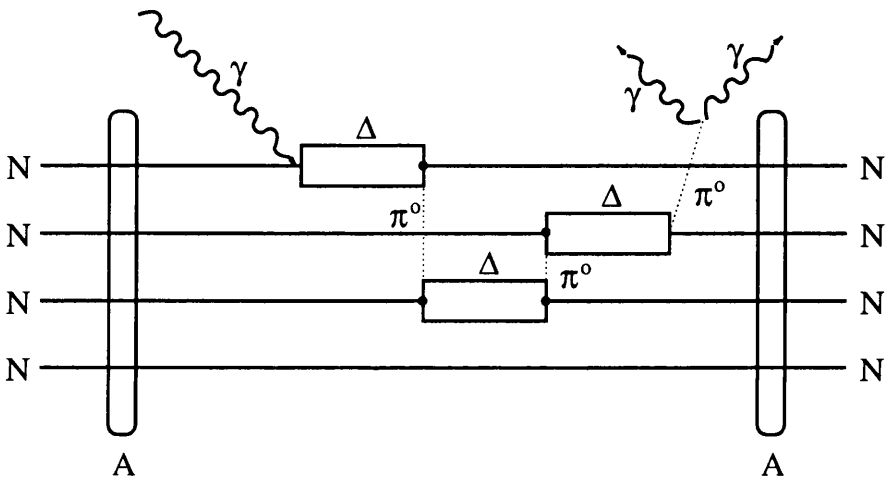


Figure 4: A schematic diagram of the interaction modelled in the DREN model. Diagram from [19]

Theoretical predictions for the differential cross section for ${}^{40}\text{Ca}$ for $E_\gamma = 200$ MeV and for $E_\gamma = 350$ MeV are shown in figures 6 and 7. At $E_\gamma = 200$ MeV, the magnitude of the differential cross section predicted by the DREN is about 25 % smaller than that predicted by the PWIA and the DWIA models, indicating that the combined effect of medium modifications and allowing for multiple interactions is quite significant.

At $E_\gamma = 350$ MeV, the differential cross sections predicted by the three models are very different. The positions of the minima and maxima are very similar in the DWIA and the DREN model, but rather different in the PWIA. The positions of the minima and maxima are determined by the final state interactions, which are incorporated in the DWIA and the DREN model but neglected in the PWIA. The magnitude of the differential

cross section predicted by the three models are all rather different. This is because the magnitudes are determined by both the final state interactions and the modification of the pion production process inside the nucleus by the nuclear medium, and so is described differently by all 3 models.

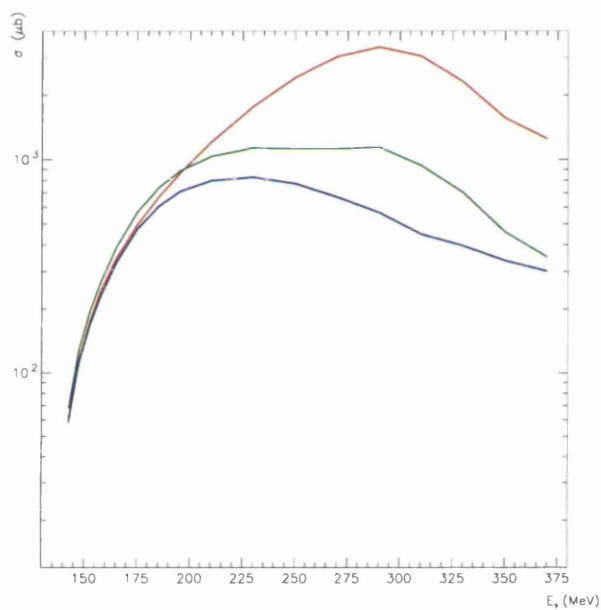


Figure 5: Theoretical calculations of σ for ^{40}Ca . Red-PWIA; green-DWIA; blue-DREN, all from [23]

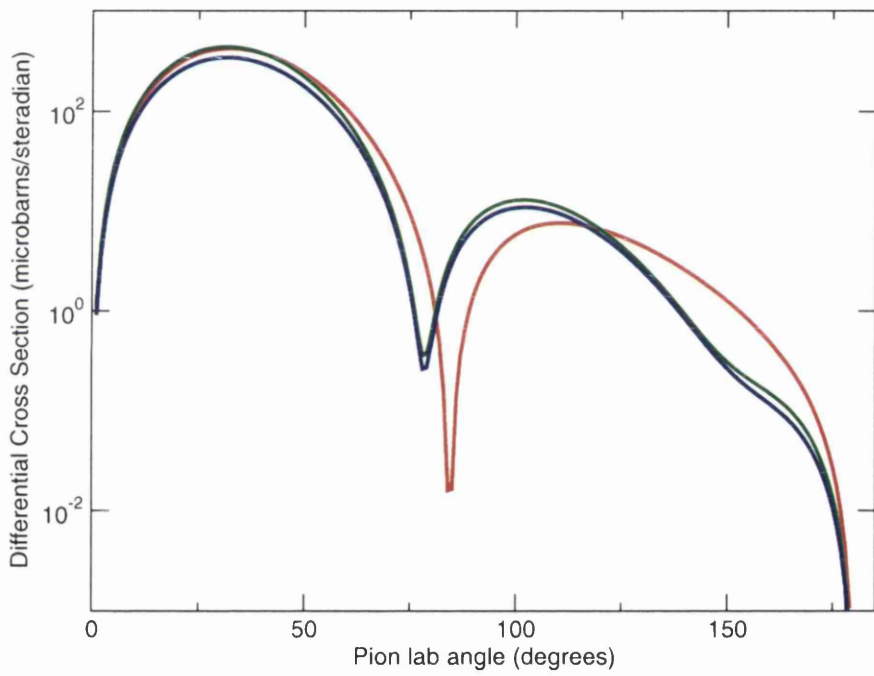


Figure 6: Theoretical calculations of $\frac{d\sigma}{d\Omega}$ for ^{40}Ca for $E_\gamma = 200$ MeV. red-PWIA; green-DWIA; blue-DREN , all from [23]

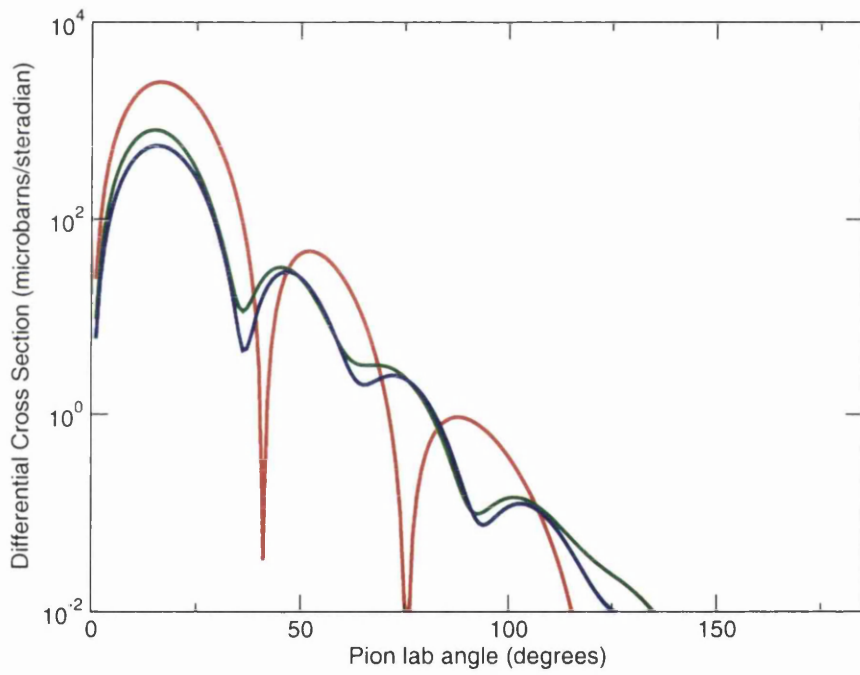


Figure 7: Theoretical calculations of $\frac{d\sigma}{d\Omega} {}^{40}\text{Ca}$ for $E_\gamma = 350$ MeV. red-PWIA; green-DWIA; blue-DREN, all from [23]

3 The experiment

The experimental set-up used to measure the (γ, π^0) -reaction on nuclei is shown in fig. 8.

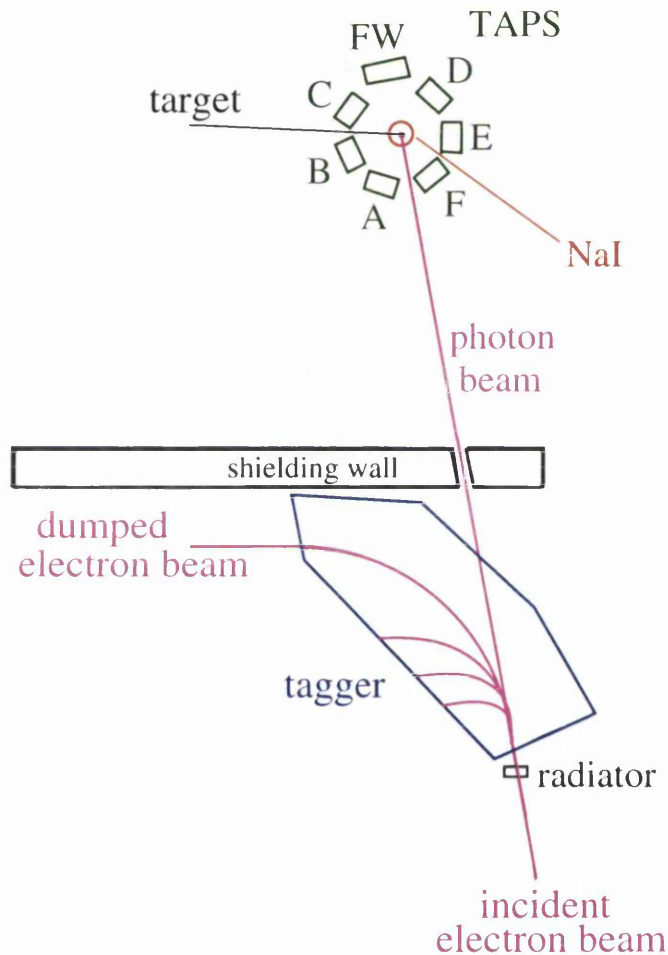


Figure 8: Experimental set-up

The Mainz Microtron (MAMI) provided an electron beam. Using the photon tagger, the electrons were made to produce photons of known energy, which were incident on the target, where some of them produced neutral pions.

The pion decayed most often to two photons, and in some of the events, the nucleus was left in an excited state, emitting a nuclear decay photon as it returned to its ground state. Some of the the pion decay photons were detected by the detector array (TAPS),

positioned around the target in the horizontal plane. Two NaI detectors, one above and one below the target, were used for detection of nuclear decay photons.

3.1 MAMI

The Mainz Microtron B (MAMI B) [29] is an electron accelerator consisting of an electron injector and three Race Track Microtrons (RTM's) (see fig. 9 and table 1). The electrons are led from an injector into each of the RTM's in turn. The RTM's are recirculating accelerators. The electron beam is led repeatedly in trajectories of increasing radius through accelerating cavities.

The electron energy obtained from RTM 3 can be varied in steps of 15 ± 0.5 MeV. The duty factor is 100 % and the maximum current is $100 \mu\text{A}$.

Table 1: MAMI data

Accelerator	Maximum electron energy (MeV)
Electron injector	3.5
RTM 1	14.35
RTM 2	179.7
RTM 3	855.0

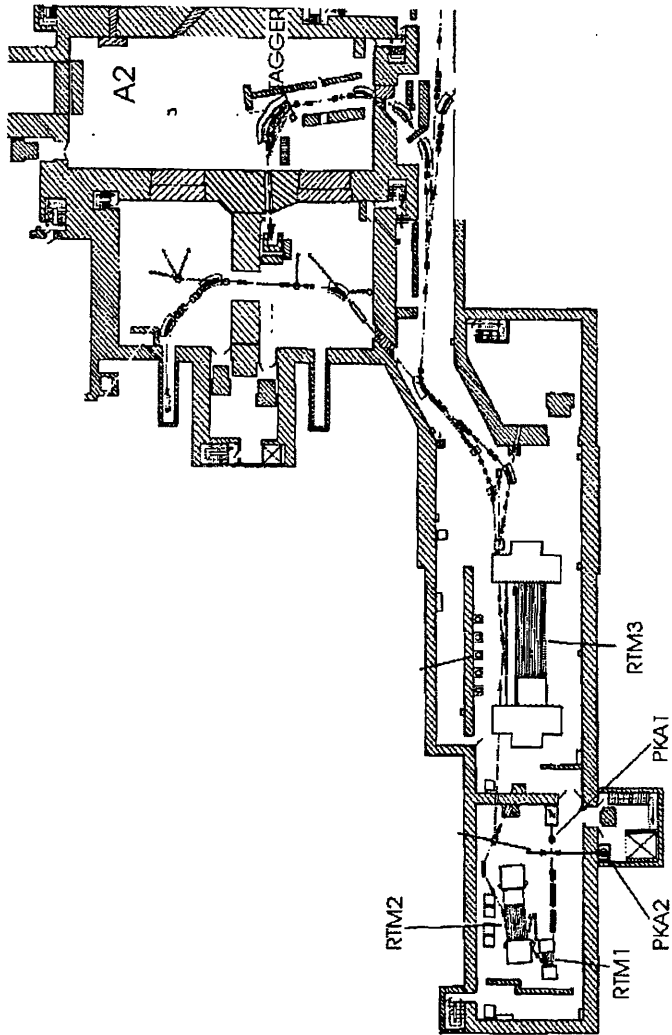


Figure 9: MAMI lay-out

3.2 The photon tagger

There are no easily available sources of monochromatic photons with energies above about 10 MeV. To provide a source of photons of known energy, the photon tagging method [30] [31] was used.

The electron beam was incident on a thin nickel radiator. The electrons were scattered in the electric field of the nickel atoms and emitted bremsstrahlung photons which were then collimated to provide a photon beam.

The residual electrons were deviated by the field of a magnetic spectrometer. This was designed so that electrons of a particular energy pass through the same point in the ‘focal plane’ of the field where they were detected by an assembly of 353 scintillators. The position of the struck detector along the focal plane determined the electron energy. The scintillators partially overlap each other such that any electron incident on the focal plane will pass through at least 2 scintillators. A coincidence between neighbouring channels is demanded in the read-out. Pulses from each tagger channel are fed to a scaler and a TDC which is started by the experimental trigger (see section 3.6).

By demanding a time coincidence between the products of a reaction induced by a tagged photon and the corresponding electron, the photon energy E_γ can be calculated from:

$$E_\gamma = E_e - E_e' \quad (7)$$

where E_e and E_e' are the electron energies before and after the emission of the photon.

The energy of the electron beam used for the present experiment was 405 MeV, providing tagged photons with an energy ranging from 135 to 380 MeV. The intrinsic tagger electron energy resolution is about 100 keV. The tagged photon energy resolution is determined by the width of the electron detector but is approximately 1 MeV for an electron beam energy of 405 MeV.

3.3 The targets

^{nat}C and ^{nat}Ca were used as targets. Natural C and Ca were used as they contain a high proportion of ^{12}C and ^{40}Ca (98.90 and 96.94 % [32]). The lengths of the targets are about $\frac{1}{10}$ of a radiation length. This is a compromise between having high enough density of $\frac{\text{nucleons}}{\text{cm}^2}$ to provide enough pion yield, and a low enough density that the pion decay photons do not have too high a probability of pair production and other atomic processes in the target (see section 4.7).

Information about the targets is summarised in table 2. The target used in the experiment was placed in an evacuated beam pipe made of 5 mm thick clear plastic. This ensured that the Ca target did not absorb a significant amount of water and reduced the probability of the pion decay photons interacting with the air molecules. The target used in the experiment was placed in the geometrical centre of TAPS with an accuracy of 2 mm.

Table 2: Target data

Target	Thickness (mm)	Surface density (g/cm ²)	Beam time (hrs)
^{12}C	25.00 ± 0.01	4.257	34
^{40}Ca	50.00 ± 0.01	1.551	136

3.4 TAPS

The initially-named Two Arm Photon Spectrometer, now Traveling Around Photon Spectrometer, TAPS, was built by a European collaboration to detect light neutral mesons (π^0 and η) via their main decay mode into two photons (98.8 % for π^0 's and 38.8 % for η 's).

TAPS at present consists of 512 individual BaF_2 detector elements. The hexagonal elements are 25.0 cm long (12 radiation lengths X_0) and have an inscribed circle radius of 59 mm. [33] (see fig. 10). The elements are wrapped in PTFE and aluminium foil to reflect the light internally in each element. Some information about BaF_2 is summarised in table 3. BaF_2 has a reasonably good energy resolution and a very good time resolution. The scintillation light has a slow and a fast component which allows pulse shape analysis (see section 4.3.1).

Table 3: BaF_2 data. E_γ is in GeV.

wavelengths (fast component)	195,210 nm
wavelength (slow component)	320 nm
fractional resolution of photon energy E_γ (FWHM)	0.59% $E_\gamma^{-0.5}$
time resolution (FWHM)	0.85 ns

Each element is fitted with a charged particle veto (CPV) detector which can help to identify charged particles (see fig. 10). The CPV detectors are made from 5 mm thick NE102A and are read out separately from the TAPS elements.

For the experiment, the elements were used in a set-up of 6 8-by-8 blocks labeled A-F and a 138-element rectangular block (the forward wall, FW) (see figures 11, 12 and 13). The set-up is summarised in table 4, where r is the distance from the geometric centre of the front face of each detector assembly to the centre of the target and θ the angle from the beam direction. All the detector assemblies were positioned in the horizontal plane.

Table 4: TAPS set-up details

block	A	B	C	FW	D	E	F
r (cm)	55.5	55.2	55.6	68.8	55.6	55.1	55.4
θ ($^\circ$)	152.4	103.0	54.0	0.0	-54.1	-103.8	-152.6

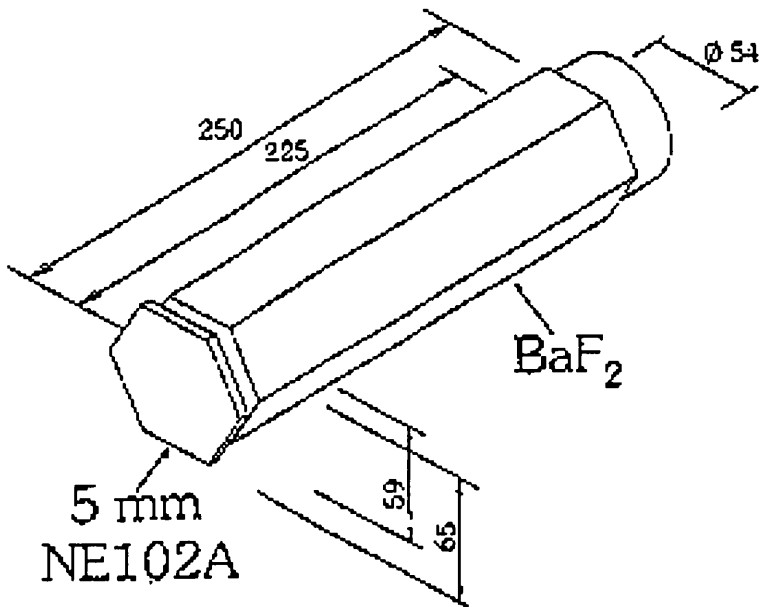


Figure 10: A TAPS element

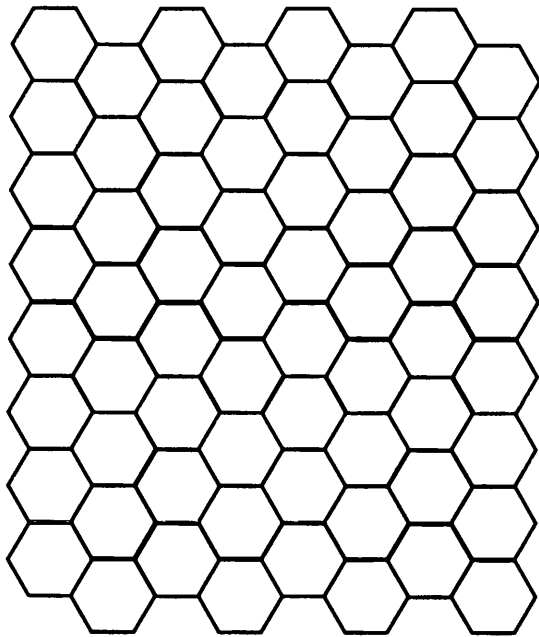


Figure 11: A TAPS block: frontal view (schematic)

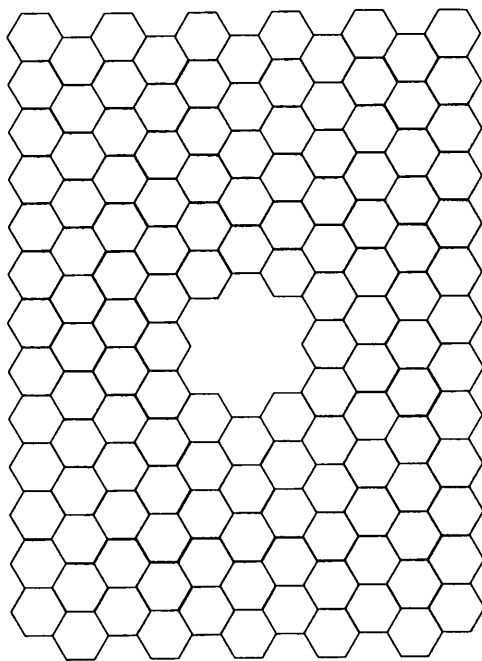


Figure 12: The forward wall: frontal view (schematic)

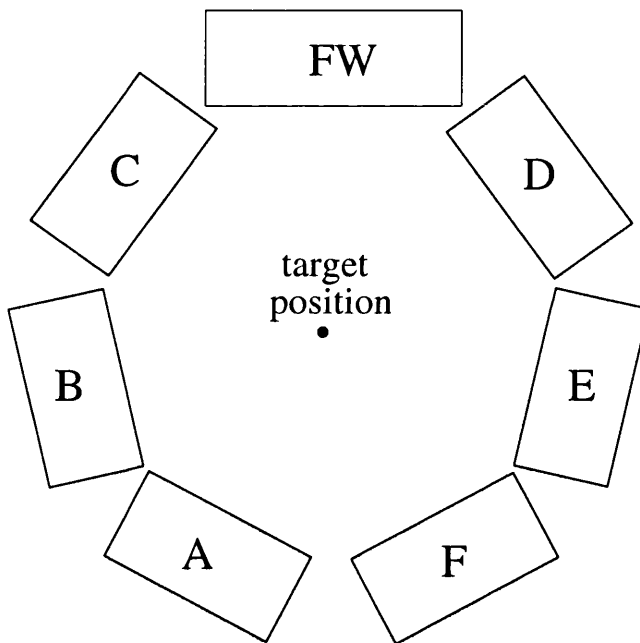


Figure 13: TAPS set-up: seen from above (schematic)

3.5 The NaI detectors

Two NaI detectors (one of the make Bicron, one Harshaw) were used for detecting nuclear decay photons from the targets. Each NaI detector contained a NaI crystal in an Aluminium casing. The energy deposited in each detector was read out with 7 photo-tubes.

Table 5: NaI data

	Bicron	Harshaw
Model	9.37414/73	5-2117
Length (cm)	23.81	25.40
Diameter (cm)	24.76	25.5
Distance from beam (cm)	11.50	11.50
Solid angle (steradians)	1.94	2.07
Dynamic Range (MeV)	0-23.2	0-23.5

The NaI detectors were positioned above and below the target, as close to the target as possible without interfering with the line of sight from the target to the outer edges of TAPS.

3.6 Detector read-out

The pulses from each TAPS element were passed through a splitter to a leading edge discriminator (LED), a constant fraction discriminator (CFD) and to two charge to digital converters (QDC's), one with a short (50 ns) and one with a long (2 μ s) gate. The LED's were used to trigger the read-out and had a threshold of 10 MeV; the CFD's were used to get accurate timing information when the elements had been triggered and the had low thresholds, usually about 0.5-1.0 MeV. The RDV modules provided the logic gates.

Three inputs were allowed to trigger the read-out for the data-taking runs:

1) The presence of two LED signals from separate TAPS blocks was taken as indicating a π^0 event in TAPS (the FW was treated as one block). Since the maximum photon energy

was 380 MeV, the minimum opening angle between the two pion decay photons was $\approx 42^\circ$. Only very few pions resulted in both their decay photons hitting the same block.

2) A single LED signal. This was done for diagnostic purposes and this trigger was scaled down by a factor of 100.

3) A pulser to provide a continuous monitor of the QDC pedestal.

A simplified diagram of the readout is shown in fig. 14.

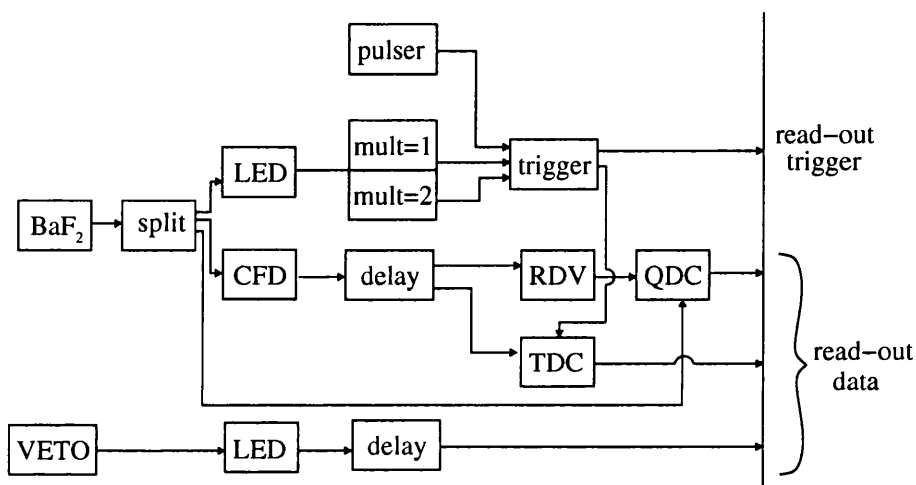


Figure 14: TAPS read-out

3.7 Execution of the experiment

Several different combinations of the electron beam current and of the TAPS trigger set-up were used in the experiment.

To acquire data on neutral pion production, the beam current was about 30 nA and the trigger was the standard TAPS trigger (see section 3.6). The data runs, that is the runs where data on neutral pion production was collected, were carried out in two periods of 10 days with 14 days between the two periods.

Before and after each data run, cosmic calibration runs were carried out (see section 4.2.1). In these runs, there was no beam and the TAPS elements were made to trigger on cosmic muons passing through them.

During the data runs, tagging efficiency runs were carried out. In the tagging efficiency runs, the beam was used with a very small current (about 0.07 pA) and lead glass detector positioned in the beam to detect photons. TAPS was not used in the tagging efficiency runs. The fraction of tagging electrons which produced bremsstrahlung photons which passed through the collimator, the tagging efficiency ϵ_{tagg} , was determined by eq. 8:

$$\epsilon_{tagg} = \frac{N_{\gamma}^{det}}{N_e^{prod}} \quad (8)$$

For each tagger channel, N_{γ}^{det} is the number of events in the lead glass detector coincident with that tagger channel (i.e. in the prompt peak of the tagger TDC spectrum) and N_e^{prod} is the number of residual electrons in that channel recorded in the tagger scalers. ϵ_{tagg} was typically about 30 %. Tagging efficiency runs were carried out at different times to monitor the changes in tagging efficiency during the data runs. The tagging efficiency runs were analysed and 18 tagging efficiency calibration files were produced each containing values for the tagging efficiency for each tagger channel.

4 Data analysis

4.1 Steps of the analysis

This section outlines the steps in the analysis.

The energy deposited in the detectors was read out by QDC's (charge to digital converters). The output of the QDC's is in channels. A translation from QDC channel number to energy - an energy calibration - was needed. The energy signals from the TAPS elements were integrated in the QDC using both a narrow and a wide (50 ns and 2 μ s) logic signal as gate. The energies deposited in these two time intervals - the wide and the narrow gate energy - required separate energy calibrations. Energy calibrations were also carried out for the two NaI detectors using radioactive sources. Systematic changes in the energy calibration during the data runs were investigated.

The time signals from the TAPS elements and the tagger were read out by TDC's (time to digital converters). The TDC's also output channel numbers. The TDC outputs from the tagger were aligned and time calibrations - translations from TDC channel number to time - were produced for the TAPS elements.

Once the energy calibration had been carried out, the photons could be separated from heavier particles like mesons and baryons by comparing the wide and narrow gate energy signals - by pulse shape analysis (PSA). To exclude heavier particles, PSA cuts were determined for every TAPS element. The outputs from the veto detectors were also examined. Selection criteria for which TAPS elements could constitute part of a cluster were developed.

The photon cluster energy was reconstructed, and several different ways of reconstructing the position of the cluster were investigated. A systematic error also arose from the position reconstruction: a correction for this was applied.

The so-called missing energy of the pion was reconstructed. The use of the veto detectors was reconsidered. Cuts in timing and reconstructed pion mass were applied in the data to select pions and fits were made to the missing energy distributions to determine the coherent part of the cross section.

The maximum likelihood method, a method which uses all the information available to obtain the most likely values of the pion energy and momentum, was applied to the data and the results were investigated. The efficiency with which TAPS detected pions was calculated using GEANT 3.21 simulations.

Finally, the cross sections and their associated errors were evaluated and the data from the NaI detectors were investigated.

4.2 Calibration of the detectors

4.2.1 Energy calibrations

Energy calibrations can be carried out in various ways: using radioactive sources, firing the tagged photon beam straight into the elements, or detecting cosmic radiation. Available radioactive sources provide photons with energies up to about 10 MeV, considerably below the region of interest. The set-up of the TAPS blocks made it difficult to move them into the photon beam. The initial energy calibrations were therefore carried out using cosmic rays.

Muons, secondary reaction products from cosmic rays, are generated in the upper atmosphere from cosmic rays. A typical TAPS muon energy deposition spectrum is shown in fig. 15. Muons were detected in calibration runs before and after each data run by triggering the data acquisition on a single hit in any TAPS element with a minimum energy of 10 MeV. The energy deposited by the muons has a Landau distribution with a well-defined peak.

The channel numbers of the pedestal (the channel number corresponding to zero energy deposition) and the peak channel, known in MeV [34], allowed a calibration to be produced for each TAPS element. A pedestal pulser, which triggered read-out of all elements when no energy was deposited, was used during the data runs. The pedestal pulser triggered pedestal (PPP) was, however, slightly greater than the pedestal observed when data was obtained using the main pion trigger (the ‘true’ pedestal), possibly due to an increase in the channel number when all QDC’s were gated at the same time. This discrepancy occurred more frequently in elements using the first two input channels of

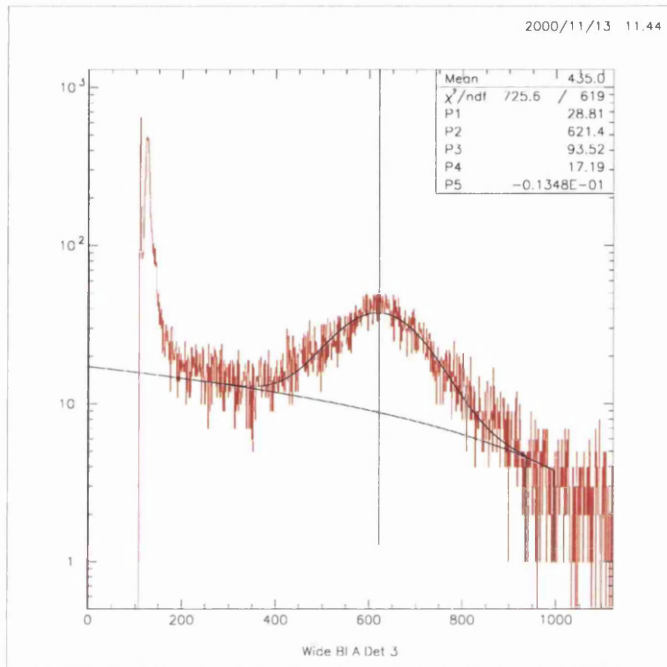


Figure 15: A TAPS cosmic muon energy deposition spectrum. The peak is fitted with a Gaussian distribution on a linear background. The pedestal is the sharp peak seen at the left hand side of the spectrum.

the 8 channel QDC. The discrepancy was constant throughout the run.

The pedestals were determined by eye. The cosmic peak position was determined by fitting a Gaussian peak on a linear background (see fig. 15).

Although energy calibrations using cosmic muons have been commonly used with TAPS for a number of years, the photon energy equivalent to the peak position of the muon energy deposition spectrum is not well known [34] [35] [36]. The calibration using the cosmic muons effectively aligned the relative QDC gains of the elements but did not produce the correct absolute energy calibration for the TAPS elements. To obtain the absolute calibration, 38 MeV was used as the energy of the peak position in the energy deposition spectrum of cosmic muons. The mass of the π^0 was reconstructed using the measured cluster energies and the photon lab opening angle ψ (see section 4.5.1). The cluster energies (see section 4.4.1) were multiplied by a factor of 1.05 to shift the peak of

the reconstructed pion mass distribution to the tabulated value.

4.2.2 Changes in the energy calibration during the data runs

The PPP's were used to monitor changes in the pedestals during the data runs. The pedestals were found to drift over a period of several days by up to 10 channels and to jump suddenly, typically by 10 channels, during data runs.

The gain of the elements also varied. This was most prominent in the elements in the FW - in all the elements in blocks A-F the gain changes were random and less than 3 percent. The elements in the FW close to the beam line showed the greatest gain changes: the gains of those immediately next to the beam pipe decreased by about 10 percent during a data run. This change was probably due to the high (about 80000 Hz, ten times higher than a typical element in blocks A-F) count rate in those FW elements. Those elements whose gains decreased considerably in the first data-taking run had regained the gain values from the start of the first run quite accurately at the start of the second data-taking run. They then underwent a similar change in gain in the second data-taking period.

The pedestal values could be observed throughout the data-taking runs, but the gain values could only be determined from the cosmic runs before and after each data-taking run. 4 energy calibration files were produced for each data run - some pedestal values changed for each new calibration file. The initial and final gain values were used for the first and last calibration files and an average of the initial and final gain values were used for the two calibration files in the middle of each data run.

4.2.3 Time alignment

Values of the TDC gain, a translation from TDC channel number to ns, had been produced by previous work on the TAPS set-up [37].

Time alignments were carried out for both the tagger and for the TAPS elements.

For the tagger time alignment, data from the tagging efficiency run, where the photon beam was fired into a large Pb-glass detector at a very low intensity (approximately 0.07

pA), was used (see section 3.7). The time differences between the pulses in each tagging spectrometer channel (tagger channel) and the Pb-glass detector were used to align the tagger TDC spectra.

For the TAPS elements, the time difference between the time signals from each individual element and the OR signal from all the tagger channels was used to align the TDC spectra.

During the data runs, the peaks in the time spectra for both the tagger and TAPS showed both gradual changes and sudden jumps of up to several ns. Three time calibration files were made for the tagger, and 12 for TAPS, to describe these changes as accurately as possible [38].

Particles with finite mass move slower than photons. When the PSA had been carried out and could be used to exclude mesons and baryons, the time alignment for TAPS was repeated to get more accurate alignment values for the photons. The corrections needed in this second time alignment were typically less than 1 percent of the alignment value.

4.3 Identification of photons

4.3.1 Pulse shape analysis

Since the relative strength of the long decay time component in BaF₂ is greater compared with the short for particles with a higher rate of energy loss, pulse shape analysis could be carried out. When plotting the wide versus the narrow gate energy, each event can be described by polar coordinates (see fig. 16):

$$\alpha = \text{atan}\left(\frac{E_{\text{narrow}}}{E_{\text{wide}}}\right) \quad (9)$$

$$r = \sqrt{(E_{\text{narrow}})^2 + (E_{\text{wide}})^2} \quad (10)$$

The wide and narrow gate energies were calibrated such that the photons and electrons had $\alpha \approx 45^\circ$. Heavier particles have smaller values of α . This difference can be used to separate light and heavy particles in some events.

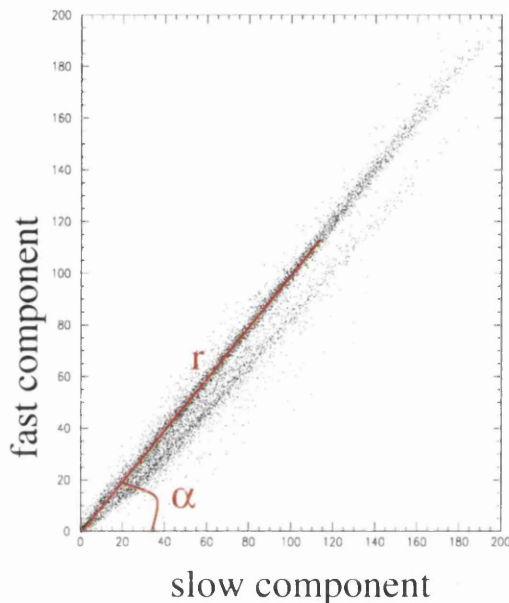


Figure 16: Pulse Shape Analysis: the narrow versus the wide energy

In fig. 17, the photons form a ridge at $\alpha = 45^\circ$, protons appear in banana shapes at lower α . Charged pions also appear in banana shapes, in between the photon ridge and the proton banana. The (α, r) plot was sliced into 12 bins in r and projected onto the α -axis (see fig. 18). Each projection was fitted with a Gaussian around the photon peak at $\alpha = 45^\circ$. From these fits, a cut could be applied for each element to cut off heavier particles (see fig. 18). The cut was defined to be a distance of 3 sigma below the peak value, where sigma is the width of the fitted Gaussian. Events which appeared on the left hand of the cut were discarded.

The photon ridge was found to bend towards low α at low r values, probably because the pedestals of the narrow gate spectra were overestimated, and towards either lower or higher α at high r values, depending on whether the narrow or wide gate signal saturated at the lower channel number.

PSA analysis was used only for particles with energies between 10 and 150 MeV to avoid the regions where the photon ridge might bend. Outside this region, no PSA was

carried out as the separation could not be done reliably and events were not discarded. The cut is shown by the white dashed line in fig. 17. Of the particles with energies between 10 and 150 MeV, particles which appeared on the right hand side of the white line were selected as photons, particles on the left hand side were discarded.

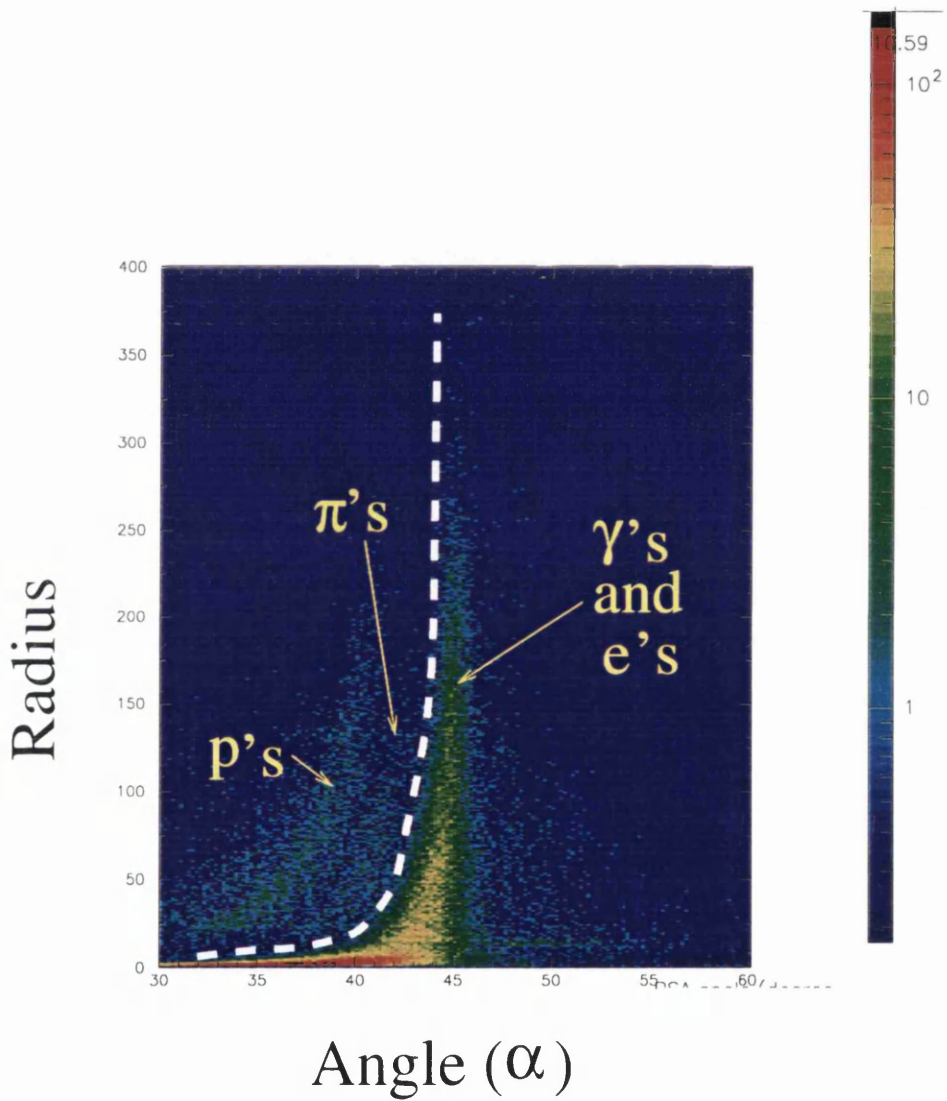


Figure 17: PSA radius versus PSA angle for one TAPS element. Photons, pions and protons can be identified for intermediate energies. Protons can only be identified and discarded in the analysis for the energy 10 - 150 MeV as the photon ridge can bend outside these energy boundaries.

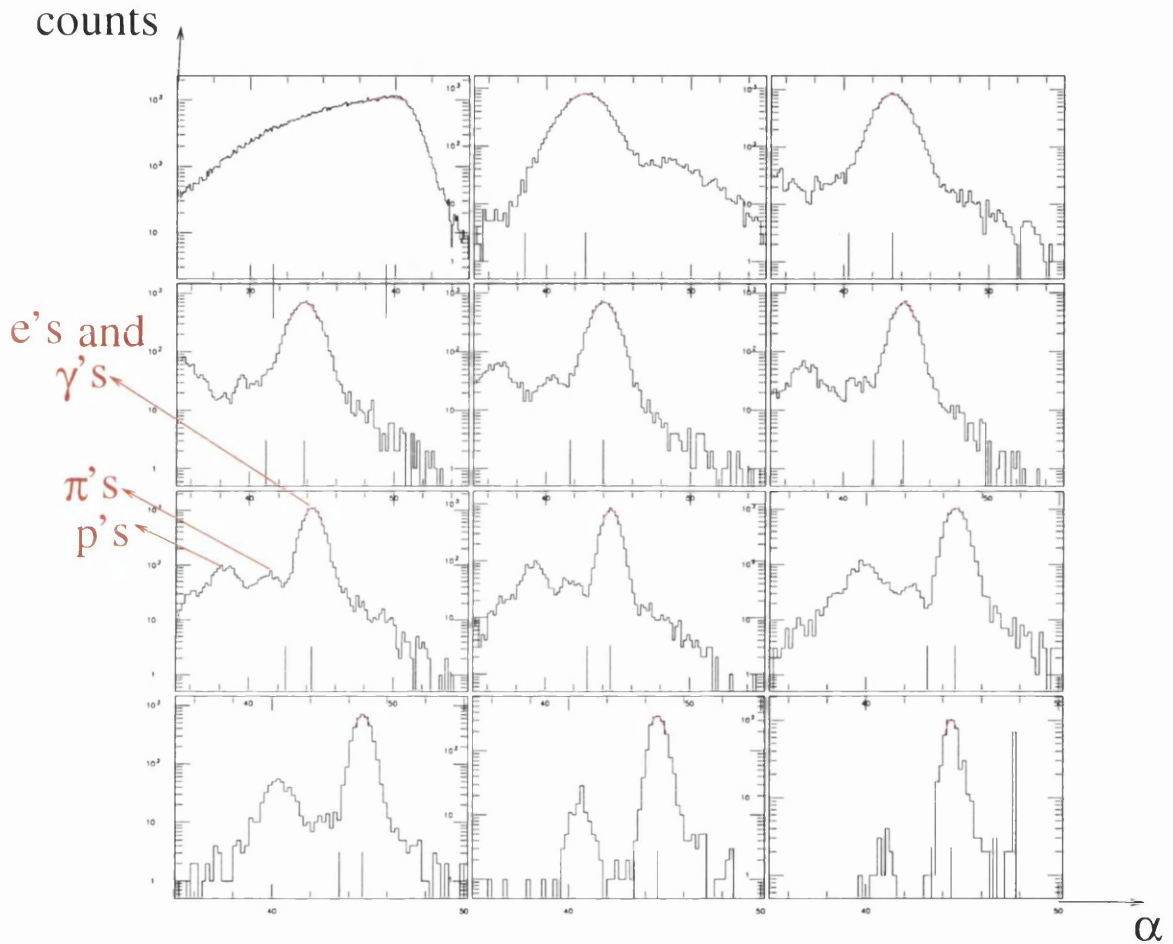


Figure 18: PSA (α, r) plot, sliced in 12 bins of r and projected onto the α axis. Plots are in bins of increasing r . The r bins range from 0-10 MeV in the top left hand plot to 237.5-380 MeV in the bottom right. For low values of r , particles cannot be identified: for intermediate values of r , particles can be separated into (photons and electrons), (pions) and (protons). For high values of r , the separation between photons and electrons, and heavier particles is possible for some TAPS elements (like the one shown) but not all. The vertical lines under each spectrum mark the fitted peak position and the 3-sigma cut-off.

4.3.2 The CPV detectors I

Each TAPS element was fitted with a charged particle veto (CPV, see section 3.4) detector mounted on its front face to help identify charged particles.

The CPV detectors were only read out by a pattern unit, hence no information about the energy deposition distribution was available. The threshold for the CPV detector should be set at the same energy for all the CPV detectors to ensure a constant efficiency for identifying charged particles for all the CPV detectors. This was attempted using radioactive sources.

Spectra showing the CPV pattern for the ^{12}C data are shown in figures 19 and 20. The CPV detectors were numbered from 1 to 522, with numbers 1-64 mounted on block A, 65-128 on block B, and similarly for blocks C-F. CPV detectors numbered 385-522 were mounted on the FW. The shape of the spectrum shows the highest number of counts in the CPV's mounted on the FW and on blocks C and D, as the distribution of the charged particles is greater for smaller pion lab angles. The CPV detectors were labeled in horizontal rows of 8 such that the rows consisted of detectors no. 1-8, 9-16 and so on. The systematic variation in the number of counts every 8 detectors in a block is due to one end of the row being at a more forward angle than the other end of the row. The rows at the top and bottom of each block are further away from the target than the rows close to the centre of the block. The CPV detectors further from the target cover a smaller solid angle than those close to it and have a smaller number of counts. The numbering system for the CPV detectors in the FW is not straightforward but generally the CPV detectors with a high number of counts are those in the centre of the FW.

Some CPV detectors did not output any signals. These were exclusively mounted on the TAPS detectors in the edges of detector assemblies. Some CPV detectors had very high count rates, due to faulty electronic modules and cabling. These were also all on TAPS elements in edges of detector assemblies. The remaining CPV detectors show a variation in count rates of a factor of 2. This is due to the difficulty in setting the thresholds correctly without access to the pulse height distribution.

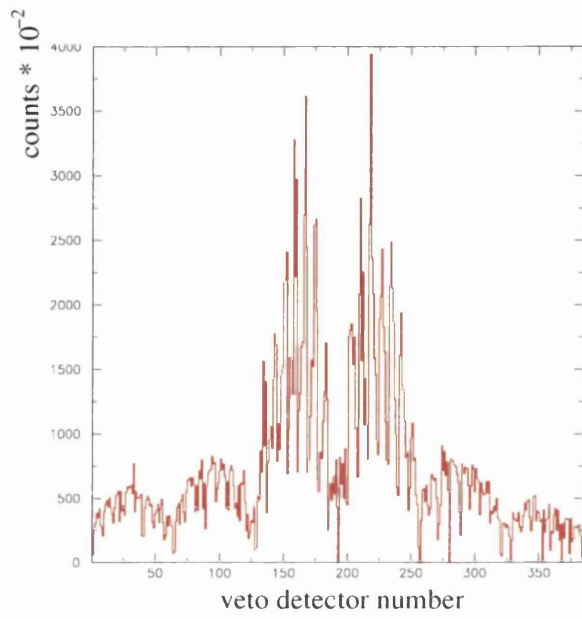


Figure 19: CPV pattern for ^{12}C data for blocks A-F

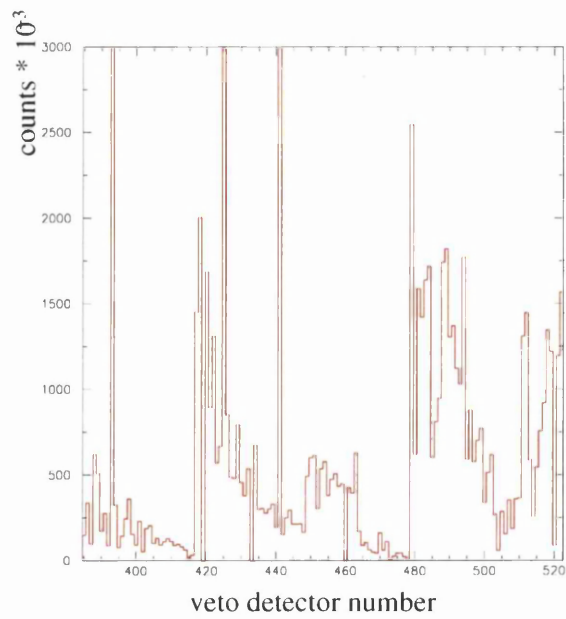


Figure 20: CPV pattern for ^{12}C data for the FW

4.3.3 Selection of clusters

When an electro-magnetic shower forms in TAPS, it often propagates through several elements, a so-called cluster, consisting of a central element (that with the greatest energy deposition), and neighbours (the remaining cluster members). All elements in the same cluster had to be physically next to at least one other cluster member.

In the analysis, an accepted cluster was required to have a minimum energy (15 MeV). The central element had to have a minimum of 10 MeV and the neighbours had to have a minimum of 1 MeV deposited energy each. The thresholds for the cluster and the central element were set so as to not discard pion decay photons while discarding low energy photons produced in the target by other processes, e.g. pair production in the target. The neighbouring element threshold was set low so as to determine the cluster energy as accurately as possible.

Elements at the edge of a TAPS block (edge elements) were not used as central elements in clusters, only as neighbours. This was done to improve the energy resolution as a significant part of the shower spreads to neighbouring elements in most events and so would not be detected if the neighbouring elements were missing. 44 % of the elements were edge elements. Excluding events where one of the central elements was an edge element led to a reduced number of events but a significantly improved energy and position resolution.

4.4 Cluster properties

4.4.1 Methods of cluster position reconstruction

The entry position (x,y) of a particle on the surface of a TAPS block can be reconstructed from the energy depositions in the central and the neighbouring elements. x and y are the horizontal and vertical distances of the entry point from the centre of the TAPS block. A good reconstruction method obtains the correct mean position when averaged over many events, with a small rms error in the distribution of reconstructed positions.

A range of position reconstruction methods were investigated for both simulated and real data. In previous analyses, two different methods of photon entry position reconstruction have been used: they relied on linear and logarithmic weighting of the energies (the “lin” and “log” methods) in each element [39] [35]. The reconstructed y position of the photon y_{rec}^γ is expressed as a weighted sum of the y positions of the elements y_i (with similar expressions for x_{rec}^γ):

$$y_{rec}^\gamma = \sum weight_i y_i \quad (11)$$

where the weights were

$$weight_{lin} = \frac{E_i}{E_{total}} \quad (12)$$

$$weight_{log} = \max(0, \log \frac{E_i}{E_{total}} + W) \quad (13)$$

where the summation takes place over all the elements i in the cluster, E_i is the energy deposited in element i and E_{total} is the total energy deposited in the cluster. The TAPS cluster energy was calculated by adding the energy depositions in all the TAPS elements which were members of the cluster. W is a constant which essentially decides the minimum energy deposit used in the reconstruction: it has usually been set so that the threshold used in the calculation matched the detector hardware threshold.

New methods of position reconstruction were investigated. The energy depositions were weighted with a power function (the ‘power’ method):

$$weight_{power} = \left(\frac{E_i}{E_{total}} \right)^P \quad (14)$$

where values from $P=0.1$ to $P=0.9$ were used. Values of P less than 1.0 were used to give elements with small energy depositions relatively large weights compared with the lin method. This is also a characteristic of the log method.

Another method ignores the greatest energy deposition and uses only the ring of 6 elements around the one with the greatest energy deposition (the “frac6” method) (see fig. 21):

$$F_1 = \left(\frac{(E_6 + E_7 + E_2) - (E_3 + E_4 + E_5)}{E_2 + E_3 + E_4 + E_5 + E_6 + E_7} \right) \quad (15)$$

$$F_2 = \left(\frac{(E_7 + E_2 + E_3) - (E_4 + E_5 + E_6)}{E_2 + E_3 + E_4 + E_5 + E_6 + E_7} \right) \quad (16)$$

$$F_3 = \left(\frac{(E_2 + E_3 + E_4) - (E_5 + E_6 + E_7)}{E_2 + E_3 + E_4 + E_5 + E_6 + E_7} \right) \quad (17)$$

$$y_{rec,frac6}^\gamma = c_{y1}(F_2 + 0.5(F_1 + F_3)) + y_1 \quad (18)$$

where y_1 is the y position of the central element, c_{y1} is a constant and the factor of 0.5 comes from projecting the unit vectors along the non-vertical axes of symmetry onto the vertical (y) direction.

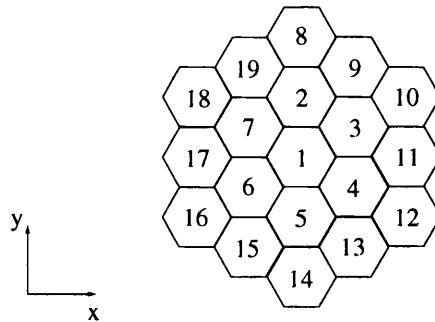


Figure 21: Numbering used in the frac6 and frac18 position reconstruction methods

Using more detailed information the two rings around the detector element can be used (the “frac18” method) (see fig. 21) using fractions like:

$$F_1 = \left(\frac{E_{top} - E_{bottom}}{E_{top} + E_{bottom}} \right) \quad (19)$$

where

$$E_{top} = E_7 + E_2 + E_3 + E_{18} + E_{19} + E_8 + E_9 + E_{10} \quad (20)$$

and

$$E_{bottom} = E_4 + E_5 + E_6 + E_{12} + E_{13} + E_{14} + E_{15} + E_{16}. \quad (21)$$

All of the reconstruction methods give an estimate of the (x,y) coordinates of the centre of the electro-magnetic shower which occurs at a distance d from the front face of the TAPS block. d increases with photon energy according to [36]:

$$d = 2.05 \text{ cm} \left(\log \frac{E_\gamma}{12.7 \text{ MeV}} + 1.2 \right). \quad (22)$$

For photons which do not hit the surface of a TAPS block at normal incidence, a correction must be made to obtain the incidence position at the face of the block (x_{corr}, y_{corr}) from the reconstructed position (x_{rec}, y_{rec}). The corrected position coordinates can be obtained through:

$$x_{corr} = x_{rec} \left(1 - \frac{d}{\sqrt{l^2 + x_{rec}^2 + y_{rec}^2 + d}} \right) \quad (23)$$

where l is the distance from the target to the centre of the front face of the TAPS block and the expression for y_{corr} is similar.

The methods of position reconstruction were tested on simulated data, obtained using GEANT 3.21 [40]. In a series of simulations, mono-energetic photons of various discrete energies were incident on the surface of a TAPS element [38]. For the simulated data, the simulated and the reconstructed positions were compared for different methods.

The distribution of reconstructed positions for different methods for 100 MeV photons incident normally at the centre of element D54 is shown in fig. 22. The average reconstructed position for various entry points for simulated data is shown in fig. 23. The lin method and the log methods with small values of W tend to pull the reconstructed entry point of photons which entered the element away from the centre and the edge, towards the centre, while the photons which entered at the centre and at the edge had their positions reconstructed correctly on average. This is because the element with the greatest energy deposition gets a very large weight compared with the elements with less deposited energy. The power methods at high P give results similar to those from the linear method.

The fractional methods and the power methods at low P , averaged over many events, tend to reconstruct the true position on average, but with a large uncertainty. Photons entering close to, but not at, the centre get their reconstructed position pulled closer to the centre, whereas photons entering close to, but not at, the edge get their reconstructed positions pulled towards the edge. In the frac18 method, the reconstructed position is pulled further towards the edge of the elements, and the uncertainty is greater than the uncertainty in the frac6 method.

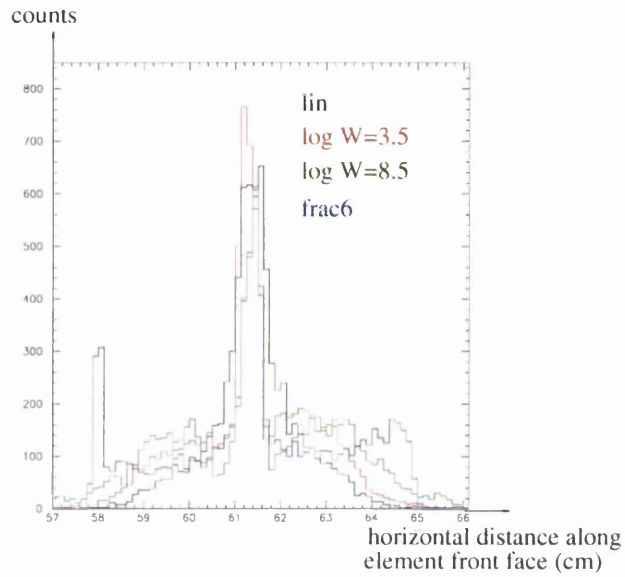


Figure 22: Distribution of reconstructed positions in element D54. The edges of the TAPS element are at 58 and 65 cm.

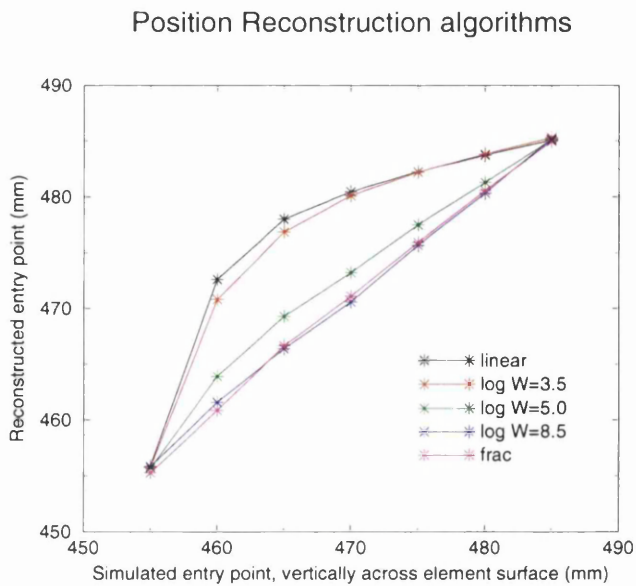


Figure 23: Average reconstructed position versus simulated entry position, using simulated data. The element centre is at 455 mm and the vertical edge at 485 mm.

The next investigations were done using real data, with the full range of incident photon energies (135-380 MeV), taken with a ^{12}C target. The reconstructed pion mass distributions were compared (see fig. 24) for the different position reconstruction methods.

The power, linear and frac18 methods produced a considerably worse pion reconstructed mass resolution than the log methods and so they were discarded. Of the remaining log methods, the log $W=3.5$ method provided a slightly better pion reconstructed mass resolution than the other log methods when using the methods of position reconstruction in the usual way.

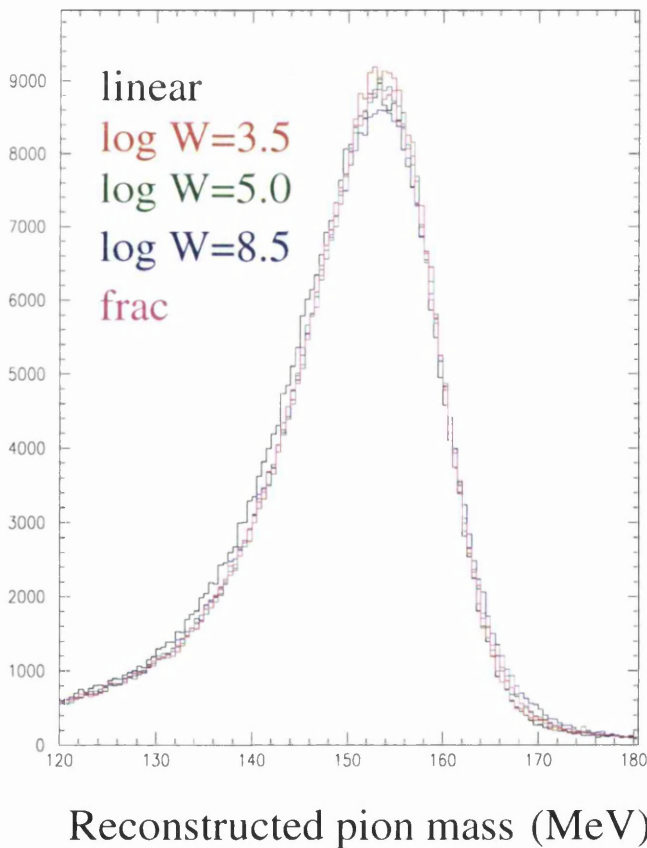


Figure 24: Reconstructed pion mass distribution for experimental data on ^{12}C . The frac method is frac6.

Two alternatives were tried for the log methods: firstly the position was reconstructed using only the central element and its 6 neighbours, secondly the reconstructed position was forced onto the edge of a circle centred at the centre of the central element and whose radius was the average element radius (see fig. 25). This was attempted because small energy depositions in elements not neighbouring the central element can be given relatively large weights using the log method, pulling the reconstructed position significantly away from the central element.

Shifting the position inside the central detector slightly worsens the reconstructed mass resolution, indicating that the electro-magnetic shower can be such that the element with the greatest energy deposition is not always the one whose surface was struck by the photon.. This probably mostly happens for photons incident at oblique angles to the element surface. Using only 7 elements instead of 19 improves the resolution, particularly when the position is shifted inside the central detector. Thus, elements not neighbouring the central one pull the reconstructed position too far from its real position, as small energy deposits are given relatively large weights with the log method.

Comparing the methods with these alternative ways of using them, the log ($W=5.0$) method, using only 7 elements and not shifting the reconstructed position inside the central detector, provided the best reconstructed mass resolution. This method was used in the analysis.

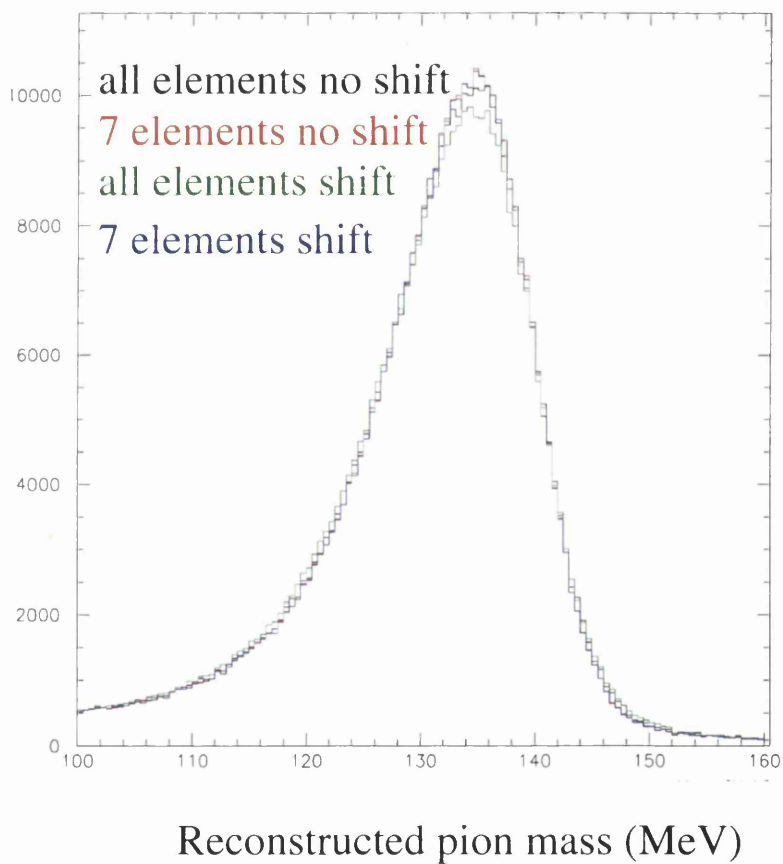


Figure 25: Reconstructed pion mass distribution for different ways of using the $\log W=3.5$ position reconstruction method

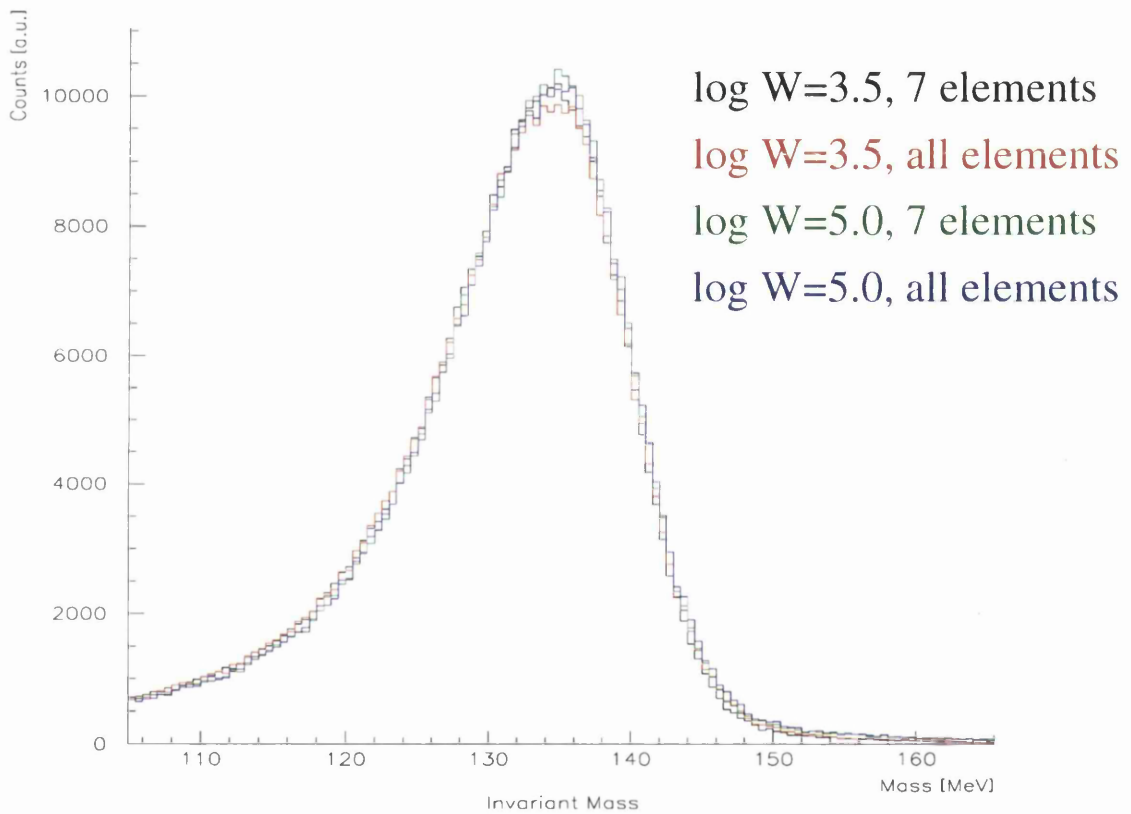


Figure 26: Reconstructed pion mass distributions using log methods with $W = 3.5$ and 5.0 , using 7 or all elements for the position reconstruction, not shifting the reconstructed position. Of all the methods investigated, the $\log W=5.0, 7$ elements method provided the best resolution.

4.4.2 Correction to the position reconstruction

The peak position in the distribution of reconstructed pion masses m_{π}^{rec} was found to vary systematically with the relative position of the cluster inside a TAPS block used to reconstruct it [38]. This indicates that reconstructed angles of the photons were increasingly in error as the photon was incident on elements closer to the edge of a TAPS block. This error is probably related to the non-normal incidence of the photons away from the centre of the TAPS block. In the absence of a detailed explanation of this effect, empirical corrections were applied to the reconstructed positions using equations 24 - 27:

$$x_{rec}^{corr,blocksA-F} = 0.9x_{rec}^{blocksA-F} \quad (24)$$

$$y_{rec}^{corr,blocksA-F} = 0.9y_{rec}^{blocksA-F} \quad (25)$$

$$x_{rec}^{corr,FW} = 0.95x_{rec}^{FW} \quad (26)$$

$$y_{rec}^{corr,FW} = 1.00y_{rec}^{FW} \quad (27)$$

where x_{rec} and y_{rec} are measured using the axes shown in fig. 27. The correction was different for TAPS blocks A-F and the FW due to their different geometries. No correction was found to be necessary for the y coordinate in the FW. This correction reduced the variation of m_{π}^{rec} for clusters in a block significantly (see ref. [38] for further details).

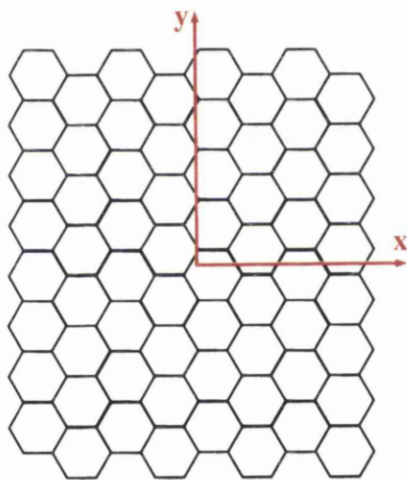


Figure 27: A TAPS block (schematic) with the coordinate system used to correct the reconstructed cluster position

4.5 Selection of pions

4.5.1 Pion kinematics and missing energy

The pion mass was reconstructed from eq. 49 (see appendix B1):

$$m_{\pi}^{rec} = \sqrt{2E_1E_2(1 - \cos\psi)} \quad (28)$$

where m_{π}^{rec} is in units of MeV, E_1 and E_2 are the measured energies of the pion decay photons and ψ their opening angle in the lab. The pion total energy E_{π} was calculated using the 'X'-formula (eq. 29) (see appendix B2):

$$E_{\pi}^2 = \frac{2m_{\pi}^2}{(1 - X^2)(1 - \cos\psi)} \quad (29)$$

where m_{π} is the well known mass of the pion and

$$X = \frac{E_1 - E_2}{E_1 + E_2} \quad (30)$$

This way of calculating E_{π} is only weakly dependent on X when the two photons have similar energies and X is small. This is beneficial as the photon energy resolution has traditionally been quite poor compared with the angular resolution in experimental data.

The missing energy for the coherent neutral pion production process is defined in eq. 31:

$$E_{miss} = E_{\pi} + E_{recoil} - E_{\gamma} \quad (31)$$

where E_{recoil} is the kinetic energy of the recoiling nucleus, obtained through energy and momentum conservation in the coherent reaction, and E_{γ} the energy of the incident photon.

A typical E_{miss} spectrum is shown in fig. 28. The peak at 0 MeV is due mainly to coherent events, the events in the tail mainly to non-coherent.

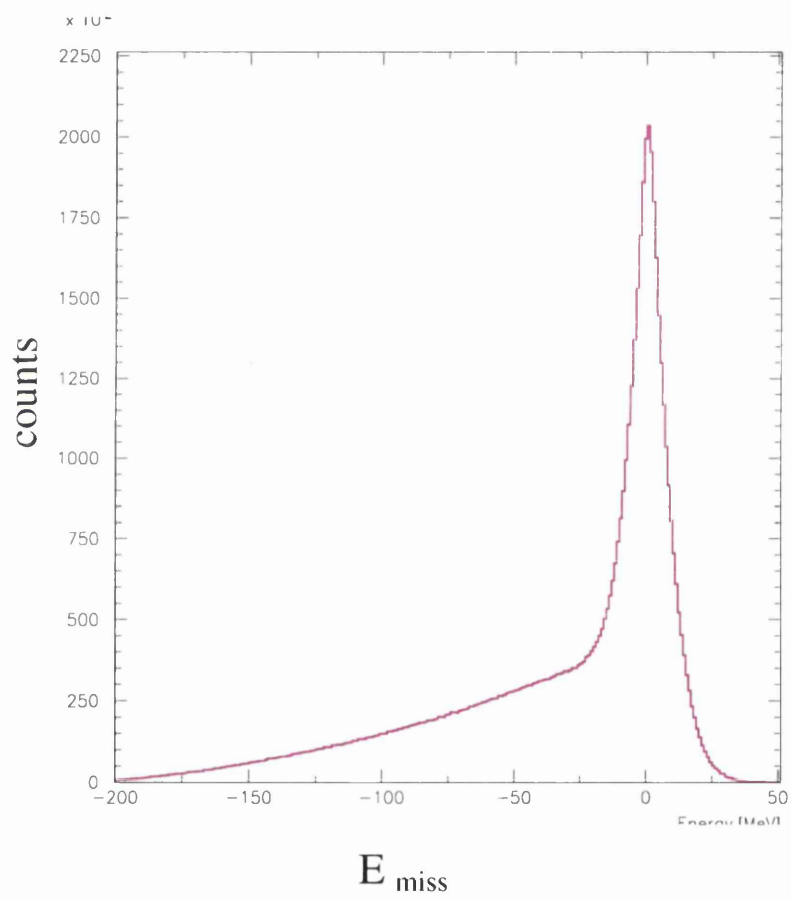


Figure 28: E_{miss} distribution for the ^{12}C data for all photon energies and all pion angles.

4.5.2 The CPV detectors II

Charged particles were produced in the experiment mostly by pair production by photons, both from pion decay and from the beam. The pair production could take place in the target, the beam pipe and in the TAPS elements, where one or more products of the pair production could be directed toward the front of the TAPS element while the main part of the shower propagated toward the back.

In events where the CPV detector firing was due to pair production in a TAPS element which is part of a pion decay photon cluster, it was not desirable to discard the event. Only events where the CPV on a TAPS element which was not part of a pion decay photon cluster fired should be discarded. At least two clusters had to be present to start the trigger (see section 3.6). Combining a cluster created by a charged particle propagating through the CPV detector with a cluster made by a pion decay photon, or two clusters from the electron-positron pair, would most probably reconstruct a pion mass very different from the tabulated value. A spectrum of the reconstructed mass excluding clusters when the CPV on a central detector fired clearly reduces the bump at about 25 MeV but does not greatly reduce the peak counts and such events would be removed by the pion mass selection (see section 4.5.3). Any benefit from excluding charged particle events would be greatest at backward pion angles where the ratio of coherent to non-coherent events is smaller.

The missing energy distribution for ^{40}Ca for $\theta_\pi > 40^\circ$ is shown in fig. 29. The data contributing to fig. 29 has had all the cuts used in the analysis except the CPV cut applied to it. There is a small reduction in the number of events when clusters are discarded if the CPV on their central detector fired, but the fractional reduction is very similar in and outside the peak region. The CPV cut is clearly not helpful in removing background. For ^{12}C , the reduction in the missing energy spectrum at backward angles when using the CPV information was similar.

Using the CPV detectors did, therefore, not improve the energy resolution. Also, when discarding clusters where the CPV detector on the central detector fired, the number of detected pions was slightly reduced. Furthermore, the efficiencies of the CPV detectors

were not well known and varied considerably. The CPV detectors were therefore not used in the analysis.

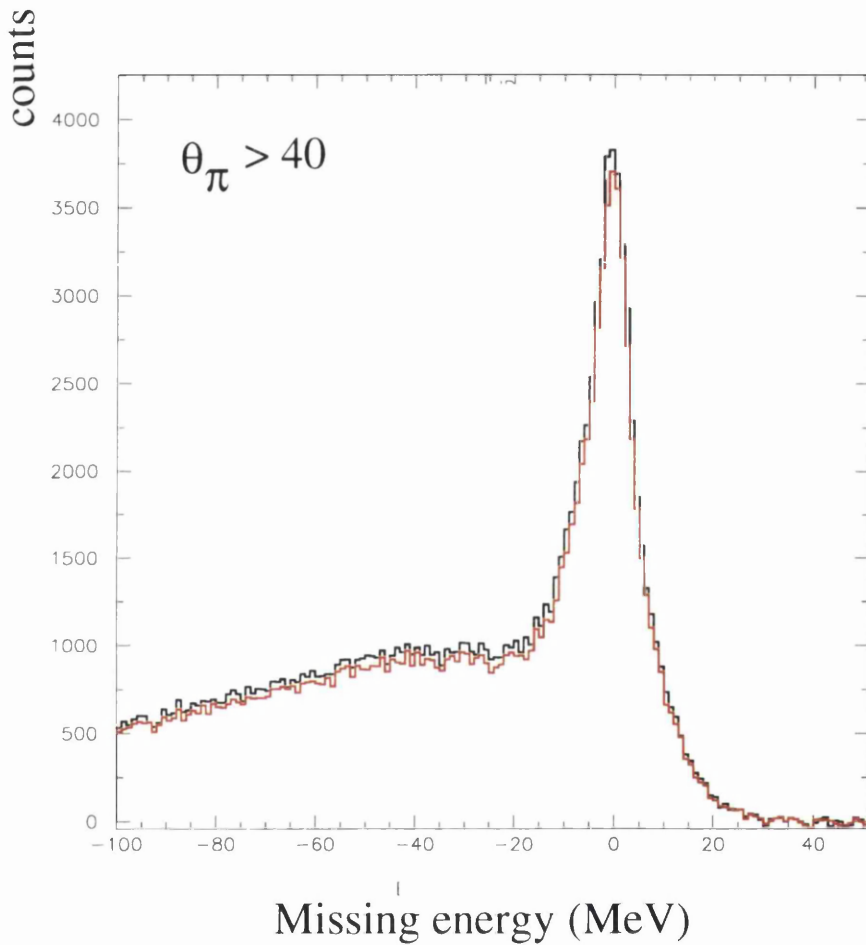


Figure 29: Pion missing energy distribution for ^{40}Ca , discarding a cluster if the central detector does not pass the PSA (black) and the PSA combined with CPV (red) criteria, respectively. The reduction in counts between the two spectra is similar in the peak of coherent events and the background of non-coherent events to the left hand side of the peak.

4.5.3 Selection of pions

The reconstructed pion mass obtained when using all pairs of photons whose clusters met the cluster conditions (see section 4.3.3), is shown in fig. 30 for ^{12}C and fig. 31 for ^{40}Ca . The events contributing to these spectra will be called the potential pions. The FWHM of the reconstructed mass spectrum is 14.2 MeV for ^{12}C and 13.9 MeV for ^{40}Ca .

To select pions from the potential pions, cuts were made on several quantities (see table 6): the reconstructed mass, m_{rec} , the time difference between the two photons detected in TAPS, $T_{\gamma\gamma}$, and the time difference between the tagging electron and the TAPS trigger, T_{TT} .

A significant number of potential pions had reconstructed masses quite far from the tabulated mass of the π^0 (134.98 MeV). There are several reasons for this. The finite resolution of TAPS smeared out the distribution of reconstructed masses, widening the peak at 135 MeV. A part of the electro-magnetic shower could escape TAPS, leading to a decrease in the detected energy and too small a reconstructed mass - this led to a slower fall-off on the low mass side of the peak. Finally, pair production in the target resulted in a photon cluster containing only a part of the photon's energy and gave rise to the bump at about 25 MeV [41]. This bump is more prominent in the ^{40}Ca data as the larger electric field in the atom gives rise to more pair production.

Table 6: Some of the cuts applied to select pions

Spectrum where cuts to select pions were applied	Selected region
Reconstructed mass	(120 : 150) MeV
Time between two pion decay photons	(-1.8 : 1.8) ns
Time between tagging electron and the TAPS trigger	(-2 : 3) ns

Potential pions whose mass was outside the region 120-150 MeV were discarded. As can be seen in figures 30 and 31, this cut discards a greater fraction of the events on the low

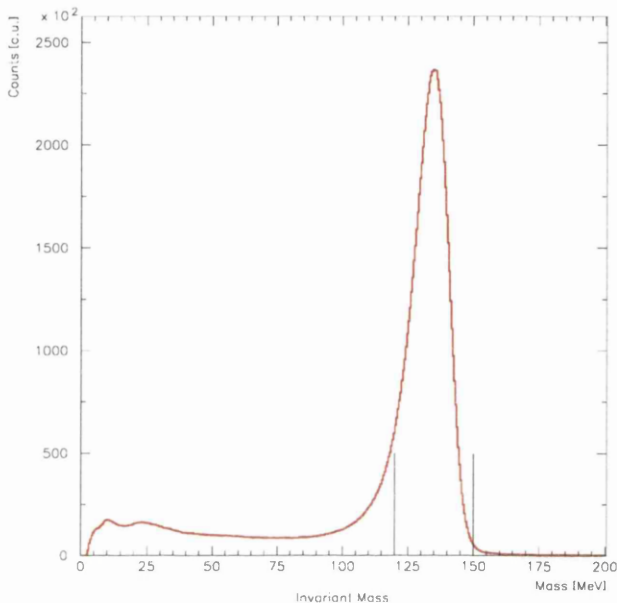


Figure 30: Reconstructed pion mass for ^{12}C . The vertical black lines show where the cut was made.

reconstructed mass side of the peak than on the high. The discarded events do, however, have significantly too low a reconstructed mass, due to leakage of the electro-magnetic shower out of TAPS, and discarding them improved the overall energy resolution of the remaining potential pions.

Potential pions where $T_{\gamma\gamma}$ was outside the interval $(-1.80, 1.80)$ ns were discarded (see fig. 32). Due to the good time resolution of TAPS after the pulse shape analysis (see section 4.3.1), this distribution was sharp and only about 0.1 % of the potential pions were discarded with this cut.

The spectrum of time difference between the tagger and the TAPS trigger, shown in fig. 33, has a coincidence peak near zero time on a flat background due to random coincidences. To select the prompt coincidences, potential pions where T_{TT} was outside the region $(-2.0, 3.0)$ ns were discarded (see fig. 33). The distribution of T_{TT} is slightly asymmetric, probably due to the time signals from TAPS and the tagger drifting during

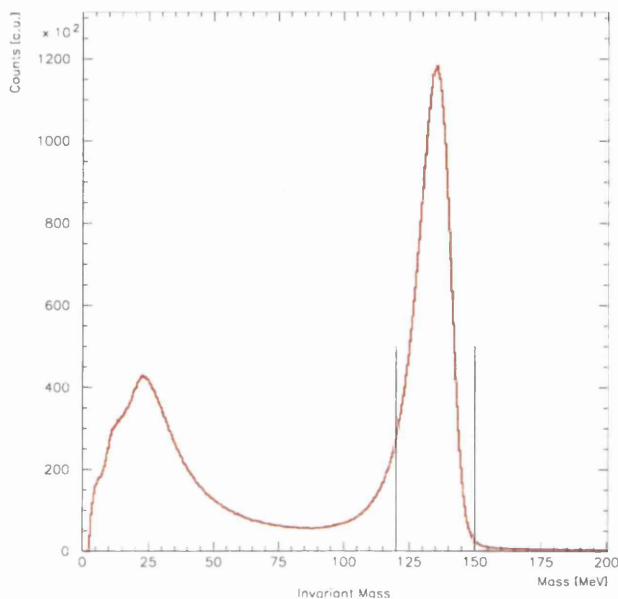


Figure 31: Reconstructed pion mass for ^{40}Ca . The vertical black lines show where the cut was made.

the data run, moving the T_{TT} spectrum away from zero. The region $(-2.0, 3.0)$ ns does, however, contain a significant background of events due to random coincidences between TAPS and the tagger. To subtract this background, regions were selected on both sides of the peak containing only random background events (see fig. 33). In the analysis used for the present experiment, these events contributed to the cross section with a weight of $-\frac{1}{6}$ as the width of the chosen background region was 6 times the width of the peak region.

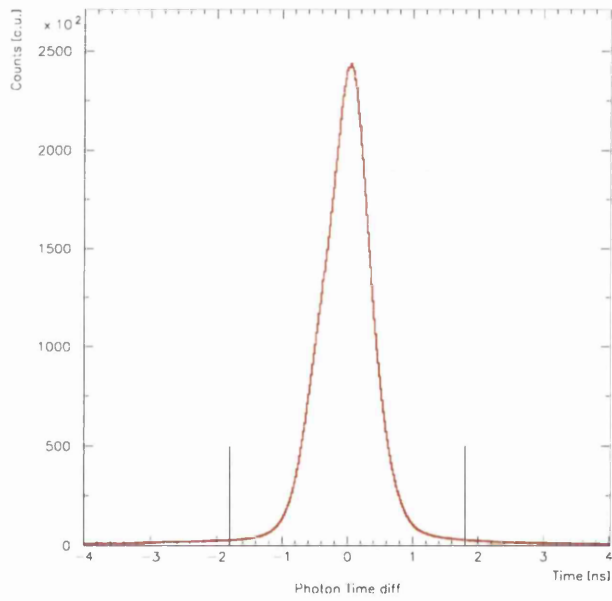


Figure 32: Time difference between the two pion decay photons for ^{12}C . The black lines show where the cut was made.

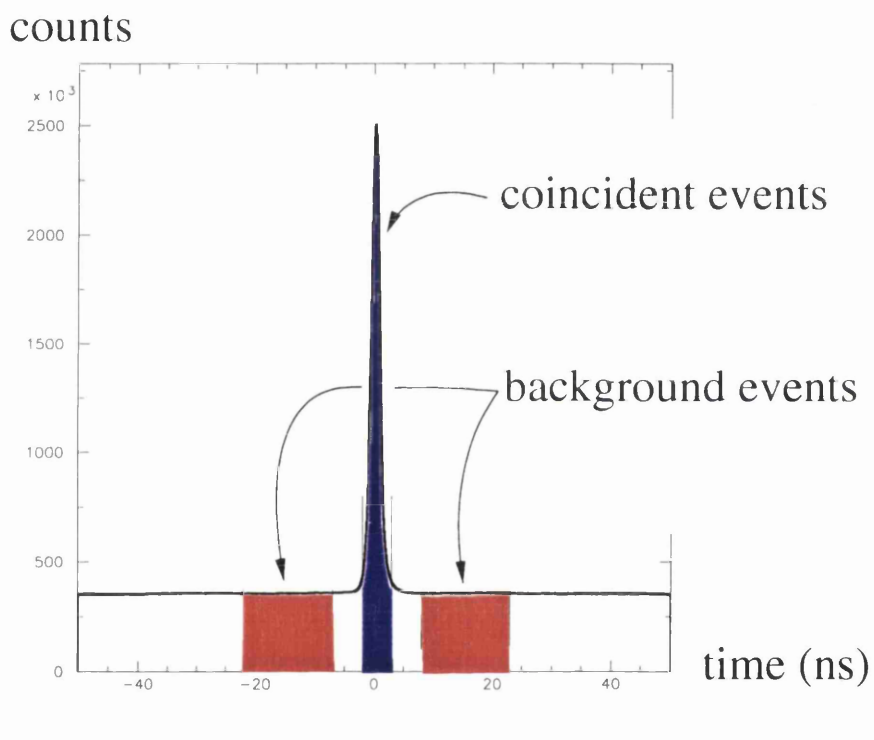


Figure 33: Time difference between the tagging electron and TAPS trigger. The blue area contains potential pions selected by the cut, the red area potential pions selected for random background subtraction.

4.5.4 Selection of coherent events

Several different processes contribute to neutral pion photo-production. Examples of these are: coherent processes, where the nucleus is left in its ground state; nuclear excited state processes, where the nucleus is left in an excited state after the pion production; quasi-free processes, where a proton or neutron is knocked out of the nucleus and a neutral pion is produced; and double pion production.

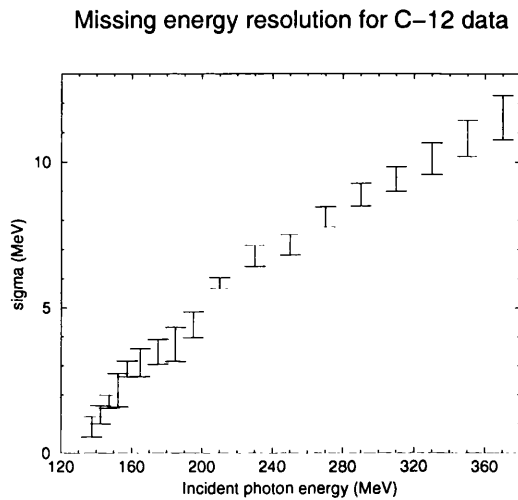


Figure 34: Missing energy resolution σ obtained using ^{12}C data and averaged over all pion angles. Statistical errors are shown.

To obtain the coherent yield, the non-coherent yield must be eliminated from the total. The extra energy required for the processes mentioned above compared with coherent production are shown in table 7. The elimination of some of the non-coherent processes could be carried out by selecting events whose missing energy was close to zero. This was only possible when the extra energy required for the process was significantly greater than the energy resolution of TAPS (see fig. 34).

For most incident photon energies, the energy resolution was not good enough to eliminate the nuclear excited state events with low nuclear excitation energies. Quasi-free events could be eliminated for low incident photon energies. Double pion production events could be eliminated at all incident photon energies.

Table 7: Some of the non-coherent processes contributing to π^0 -production. The extra energy required compared with the coherent reaction is shown. There are many more nuclear excitation states than those listed for both nuclei - only the lowest few are listed.

Process	Extra energy required (MeV)	
	^{12}C	^{40}Ca
Nuclear excitation	4.4, 15.0, ...	3.7, 4.5, ...
Proton knock-out	16.0	12.5
Neutron knock-out	18.7	9.9
2 π^0 production	134.98	134.98

The yield of the non-coherent processes varies slowly with θ_π [42] [43], whereas the coherent pion production yield is known (see section 2.3 - 2.5) to decrease with θ_π by a large factor. At large θ_π , the ratio of non-coherent to coherent events becomes large and the coherent peak becomes harder to distinguish.

Missing energy spectra for ^{12}C for various incident photon energies and pion lab angles are shown in figures 35 - 38.

At incident photon energies close to the pion production threshold, the energy resolution was very good (see fig. 35). Non-coherent processes did not contribute significantly: at threshold there is not enough energy for them to occur, and the yield of these processes increases slowly with increasing incident photon energy while the coherent yield initially increases more rapidly [43]. At incident photon energies around 200 MeV, non-coherent processes contribute significantly to the yield - there is a 'tail' on the left hand side of the coherent missing energy peak (see fig. 36). As the yield of the coherent process decreases with pion lab angle, the non-coherent processes constitute a greater fraction of the total yield. The apparent peak position has shifted from 2 MeV in fig. 36 to -8 MeV in fig. 38. The variation of apparent missing energy peak position as a function of pion lab angle is

shown in fig 39. For small pion lab angles, the apparent peak position is close to some value of missing energy, E^i . It starts to shift significantly away from E^i at a particular pion lab angle, θ^* , which generally decreases for increasing incident photon energies. Whereas the reconstructed pion decay photon energies and angles are known to contain systematic errors, these are not great enough to explain the variation in the apparent missing energy peak position.

The values of θ^* were found to coincide roughly with the theoretically predicted values of the angle where the magnitude of the coherent yield becomes significantly reduced compared with the maximum cross section values in the angular distribution. The variation in apparent peak position can be explained as a combination of a variation in the peak position of the coherent yield due to systematic errors in the reconstructed pion energy and angle, and a variation in the relative contributions from the different processes contributing to the missing energy distribution. When the yield from the coherent process decreases, the yield from the nuclear excited states and the quasi-free processes can become important in the total yield. The apparent position of the peak in the missing energy distribution then becomes the average peak position of the combination of distributions due to the different processes.

The shape of the coherent part of the missing energy distribution also varied significantly with the incident photon energy and the pion angle. At low E_γ 's, the shape was well fitted with a single Gaussian function (see fig. 35). At E_γ around 200 MeV, the shape of the missing energy distribution was not described well by a Gaussian function (see fig. 36). This is probably due to the apparent peak position of the missing energy distribution moving significantly over the energy range contributing to the data: the distribution in fig. 36 is probably the sum of many Gaussian distributions, each with a slightly different peak position. Distributions with this shape could be fitted with two Gaussian functions and a Fermi function used to represent the fall-off of the distribution from the quasi-free processes below its average threshold E_{av} .

The function used to fit the data was:

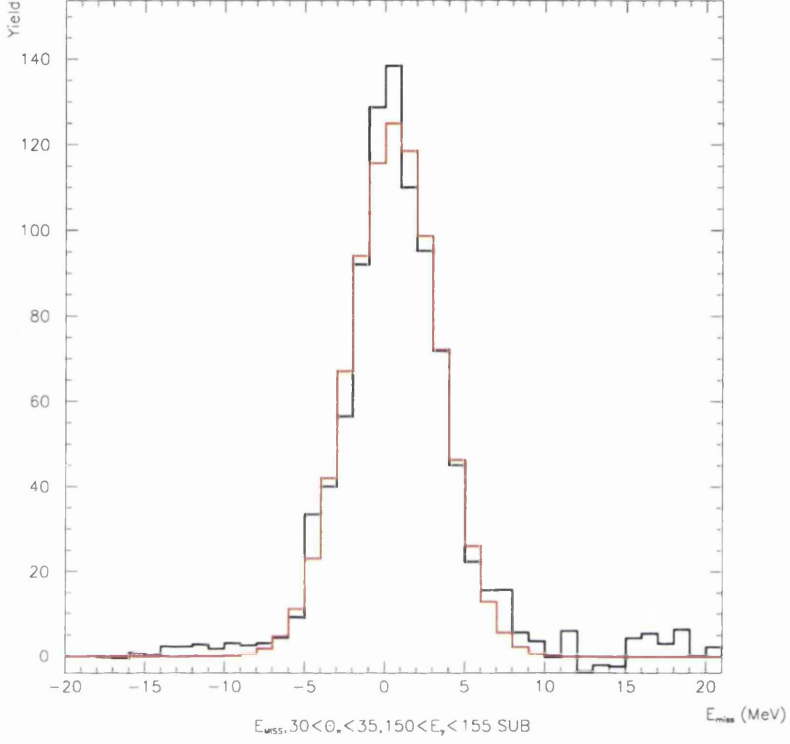


Figure 35: Missing energy spectrum for ^{12}C for $30 < \theta_\pi < 35^\circ$ and $150 < E_\gamma < 155$ MeV, fitted with method 1. The data is shown in black and the fitted single Gaussian function in red.

$$F = \frac{A_1}{\sqrt{2\pi} \sigma_1} \exp\left(-\frac{(x - x_c)^2}{2\sigma_1^2}\right) + \frac{A_2}{\sqrt{2\pi} \sigma_2} \exp\left(-\frac{(x - x_c)^2}{2\sigma_2^2}\right) + \frac{A_Q \sigma_F \sqrt{2\pi}}{1 + \exp\left(2.4 \frac{x - x_c + E_{av}}{\sigma_F \sqrt{2}}\right)} \quad (32)$$

where A_1 and A_2 are the areas, σ_1 and σ_2 the widths and x_c the common centre of the Gaussian functions, A_Q the height of the Fermi function, x the missing energy, E_{av} the average energy required for the quasi-free process and

$$\sigma_F = \sqrt{\frac{A_1 \sigma_1^2 + A_2 \sigma_2^2}{A_1 + A_2}}. \quad (33)$$

The width of the Fermi function is obtained from the Gaussian widths, weighted

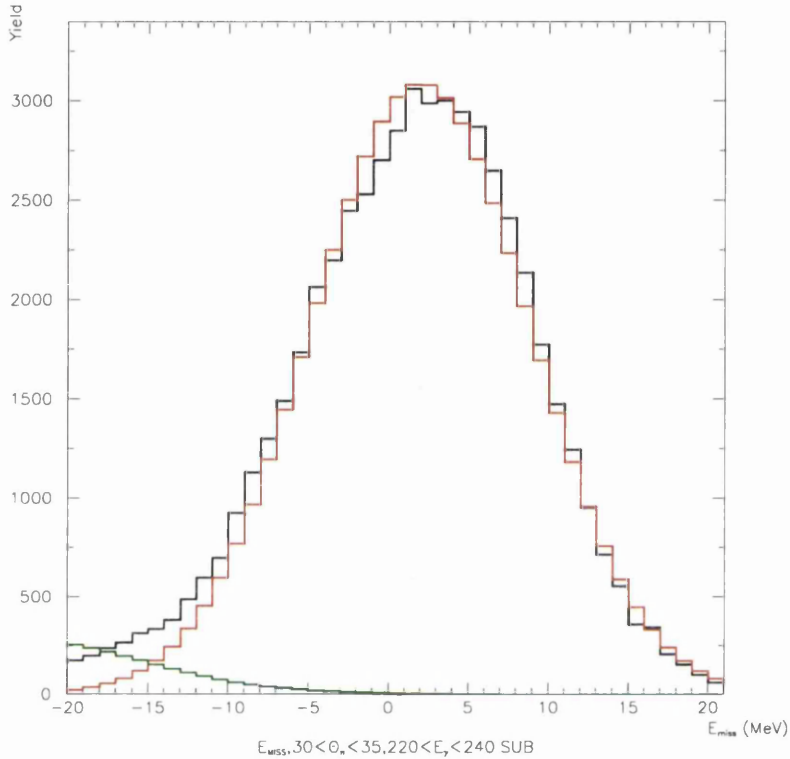


Figure 36: Missing energy spectrum for ^{12}C for $30 < \theta_\pi < 35^\circ$ and $220 < E_\gamma < 240$ MeV, fitted with method 2. The data is shown in black, the fitted double Gaussian function in red and the fitted Fermi function in green.

with the Gaussian areas such that the greatest Gaussian determined most of the width of the Fermi function to ensure that the resolutions of the distributions describing the coherent and quasi-free processes were consistent. The slight asymmetry of the measured missing energy spectrum in the peak region in fig. 35 suggests that the incoherent process is making a significant contribution. However, without any knowledge of which nuclear states are populated it was not possible to include the shape of the nuclear excitation pion production distribution in the fit. When this contribution became large, a different fitting procedure, method 3, was used.

Three fit methods were used to fit the missing energy distributions. All the fits were

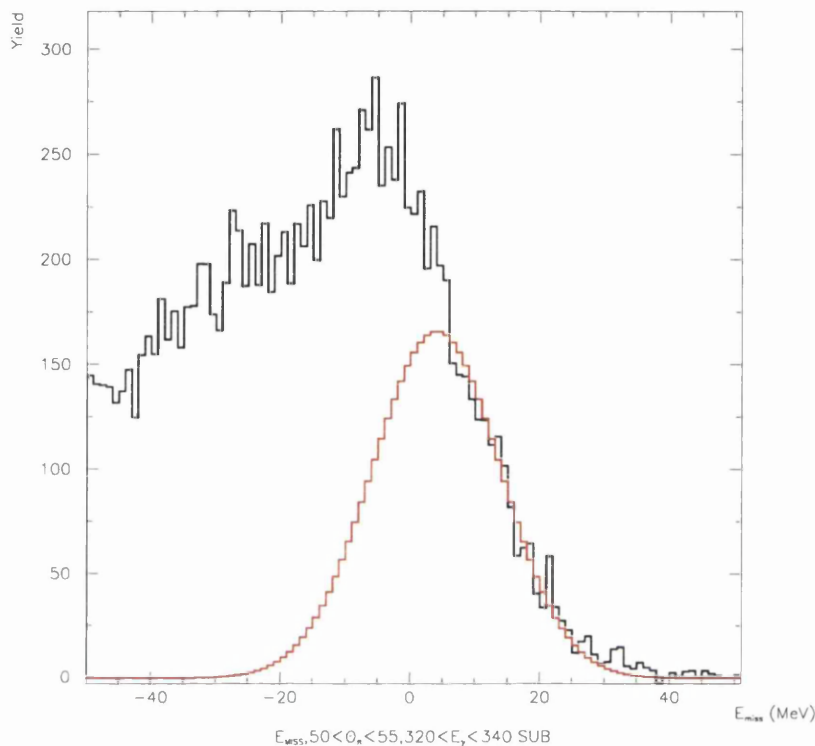


Figure 37: Missing energy spectrum for ^{12}C for $50 < \theta_\pi < 55^\circ$ and $190 < E_\gamma < 200$ MeV, fitted with method 3. The data is shown in black and the fitted single Gaussian function in red.

carried out using the graphics tool Minuit [44].

- Method 1: A Gaussian plus a Fermi function were fitted, allowing the fit to determine the height, width and position of the Gaussian function and the height of the Fermi function. This method was used where the shape of the peak was described well by a single Gaussian function and where the apparent peak position was close to E^i (see fig 35). The fit function used is described in eq. 32 with $A_2 = 0$.
- Method 2: Two Gaussian plus a Fermi function were fitted. The two Gaussian functions were centred in the same place. The fit determined the heights, widths and position of the Gaussian functions and the height of the Fermi function. This

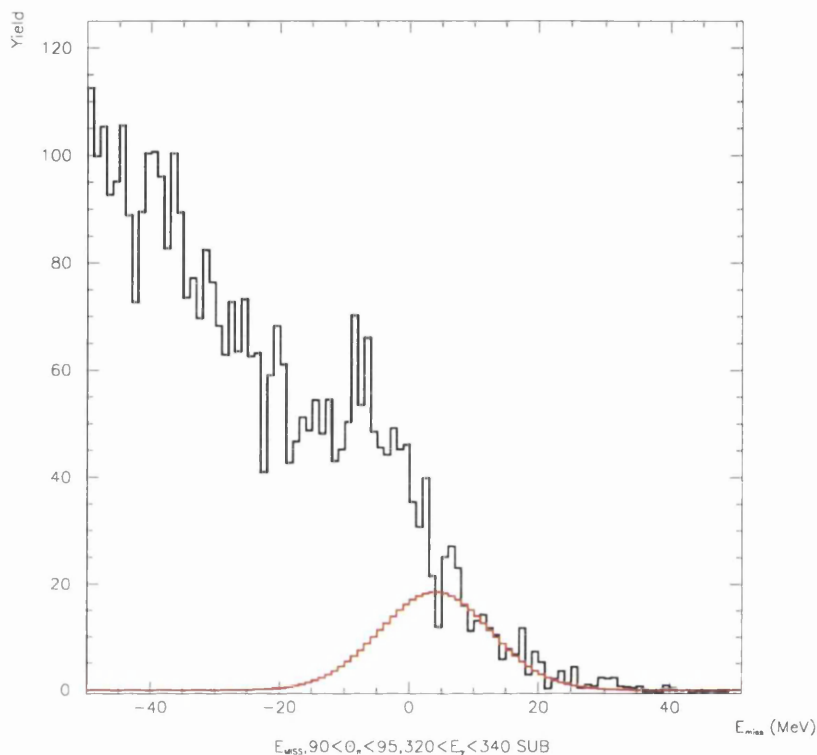


Figure 38: Missing energy spectrum for ^{12}C for $90 < \theta_\pi < 95^\circ$ and $320 < E_\gamma < 340$ MeV, using method 3. The data is shown in black and the fitted single Gaussian function in red.

method was used where the shape of the peak was described well by two Gaussian functions and where the apparent peak position had not shifted significantly away from E^i (see fig 36). The fit function used is described in eq. 32.

- Method 3: The upper half of a single Gaussian was fitted. The centre position of the Gaussian was fixed at E^i , the fit selected the height and width of the Gaussian. This method was used where the apparent peak position had shifted significantly away from E^i . (see fig 37 and fig 38). The fit function used is described in eq. 32 with $A_2 = 0$, $A_Q = 0$ and $x_c = E^i$.

In methods 1 and 2, the distance between the centre of the Gaussian function and the

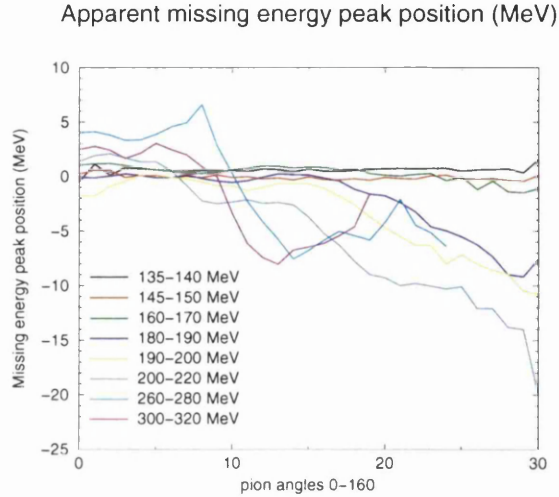


Figure 39: Apparent peak position of the missing energy distribution for ^{12}C

centre of the fall-off of the Fermi function was determined by the average extra energy required for the quasi-free process. This was done to make the fall-off of the Fermi function describe the fall-off of the quasi-free production distribution in the coherent peak region.

E^i varied with incident photon energy by up to 5 MeV. This is probably due to the systematic errors in the reconstructed energy and angle of the pion. The regions where the different fit methods were used are shown in table 8. The fit regions, and the regions where the different methods were used, are not identical for ^{12}C and ^{40}Ca . The coherent differential cross section decreases faster with pion lab angle for ^{40}Ca than for ^{12}C , hence the coherent yield could be determined at greater pion lab angles for ^{12}C than for ^{40}Ca . The first nuclear excited state occurs at a lower nuclear excitation energy in ^{40}Ca than in ^{12}C . Because the contributions from the nuclear excited states are closer to the coherent peak for ^{40}Ca , and because the coherent cross section decreases faster with pion angle for ^{40}Ca , the apparent peak position started to move away from θ^* at slightly lower incident photon energies for ^{40}Ca than ^{12}C , and thus method 3 was used at slightly lower incident photon energies for ^{40}Ca than for ^{12}C .

Table 8: Fit methods used to fit E_{miss} distributions

E_γ range (MeV)	^{12}C		^{40}Ca	
	θ_π range ($^\circ$)	fit method	θ_π range ($^\circ$)	fit method
135-140	5-155	1	0-140	1
140-145	0-165	1	0-160	1
145-150	0-170	1	0-155	1
150-155	0-175	1	0-120	1
155-160	0-165	1	0-115	1
160-170	0-165	1	0-15	1
			15-60	2
			60-85	1
			85-165	3
170-180	0-5	1	0-5	1
	5-70	2	5-25	2
	70-115	1	25-80	1
	115-160	3	80-160	3
180-190	0-5	1	0-5	1
	5-70	2	5-60	2
	70-95	1	60-165	3
	95-165	3		
190-200	0-10	1	0-10	1
	10-65	2	10-55	2
	65-85	1	55-125	3
	85-170	3		
200-220	0-40	1	0-20	1
	40-65	2	20-25	2
	65-160	3	25-135	3
220-240	5-50	1	0-10	1
	50-175	3	10-25	2
			25-150	3
240-260	5-20	1	0-15	1
	20-150	3	15-30	2
			30-130	3
260-280	5-20	1	0-5	3
	20-145	3	5-10	1
			10-15	2
			15-130	3
280-300	0-160	3	0-115	3
300-320	0-145	3	0-110	3
320-340	0-140	3	0-100	3
340-360	0-140	3	0-80	3
360-380	0-155	3	0-70	3

4.6 The maximum likelihood method

Data analysis often involves calculating unknown quantities and their associated uncertainties from several equations containing measured quantities with their associated uncertainties. If the number of equations determining the unknowns equals the number of unknowns, the equations can simply be solved to yield the unknowns. If the number of equations is greater than the number of unknowns, a fit minimising the uncertainty in the unknown quantities, a maximum likelihood method, can be used to determine the unknowns.

In π^0 -production, the two pion decay photons γ_1 and γ_2 are detected. The pion energy E_π and momentum \underline{P}_π are determined by the pion decay photon energies (E_1 and E_2) and momenta (\underline{p}_1 and \underline{p}_2) by conservation of energy and momentum:

$$E_\pi = E_1 + E_2 \quad (34)$$

$$\underline{P}_\pi = \underline{p}_1 + \underline{p}_2 \quad (35)$$

Traditionally, the pion energy has been determined using the 'X'-formula (see section 4.5.1). However, this does not make use of all the information available.

The pion momentum and energy are related by:

$$E_\pi^2 = m_\pi^2 + P_\pi^2 \quad (36)$$

where $c \equiv 1$ and m_π is the pion mass. The maximum likelihood method (MLM) [45] assumes that the momenta and polar angles associated with γ_1 and γ_2 ; $p_1, p_2, \theta_1, \theta_2, \phi_1$ and ϕ_2 , have Gaussian distributions about their true values, $\mathbf{P}_1, \mathbf{P}_2, \Theta_1, \Theta_2, \Phi_1$ and Φ_2 .

The probability Q of a set of residuals $\delta \underline{p}_i = (\delta p_i, \delta \theta_i, \delta \phi_i)$, where $\delta p_i = \mathbf{P}_i - p_i$, and $\delta \theta_i$ and $\delta \phi_i$ are defined similarly, is

$$-\ln Q \propto F = \sum_i \left\{ \frac{\delta p_i^2}{\sigma_{pi}^2} + \frac{\delta \theta_i^2}{\sigma_{\theta i}^2} + \frac{\sin^2 \theta_i \delta \phi_i^2}{\sigma_{\phi i}^2} \right\} \quad (37)$$

where σ_{p_i} and σ_{a_i} are the errors in the momentum and angle. Using equations 34 and 35, P_π and E_π are calculated. F is then minimised under the constraint obtained directly from eq. 36:

$$G_1 \equiv \frac{1}{2}(E_\pi^2 - P_\pi^2 - m_\pi^2) = p_1 p_2 (1 - \cos\psi) - \frac{1}{2}m_\pi^2 = 0 \quad (38)$$

To carry out the minimisation, the constraint is expressed in terms of the measured quantities by expanding eq. 38 and keeping only the first-order terms:

$$G_i(P_i, \Theta_i, \Phi_i) = G_i(p_i, \theta_i, \phi_i) + \sum_i \left\{ \frac{\delta G_i}{\delta p_i} \delta p_i + \frac{\delta G_i}{\delta \theta_i} \delta \theta_i + \frac{\delta G_i}{\delta \phi_i} \delta \phi_i \right\} \quad (39)$$

Using the Lagrange multiplier technique, eq. 39 can be solved subject to the constraint (eq. 38) to determine corrections (δp_i , $\delta \theta_i$ and $\delta \phi_i$) to the measured parameters. For details, see [45].

The MLM can be used iteratively; when the measured values (p_i , θ_i and ϕ_i) have been corrected once, they can be used as input into the MLM and more accurate values for the corrections can be obtained.

The MLM is illustrated in fig. 40.

The reconstructed pion mass distribution obtained using the X formula and the MLM are shown in fig. 41. The width of the distribution using the X formula simply expresses the errors in the measured photon energies and angles. The mass distribution obtained with the MLM is very narrow as the MLM works by forcing the reconstructed mass towards the pion mass.

Missing energy distributions obtained using both the X formula and the MLM are shown in fig. 42. The MLM obtains a slightly different peak channel from the X formula, but as the pion decay photon energies used to calculate E_{miss} have been shifted phenomenologically (see section 4.5.1) this does not recommend one method over the other. The energy resolution obtained using the two methods is similar for low incident photon energies: at incident photon energies above about 155 MeV the MLM produces a poorer resolution than the X formula, at energies above about 250 MeV, the resolution from the MLM is slightly better than that from the X formula.

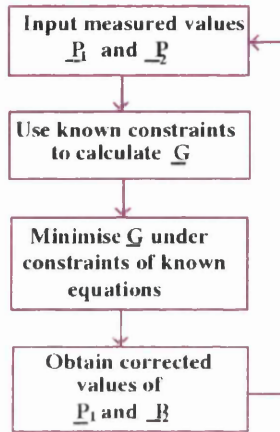


Figure 40: Flow diagram of the Maximum Likelihood Method

The MLM assumes that each of the measured variables (photon energy and angles and the incident photon energy) has a Gaussian distribution about its true value. As is indicated by the systematic changes in the peak position of the missing energy (see section 4.5.1), probably both the reconstructed photon energy and angles contain systematic errors. The MLM can therefore not be expected to work as intended. It was not used in the analysis.

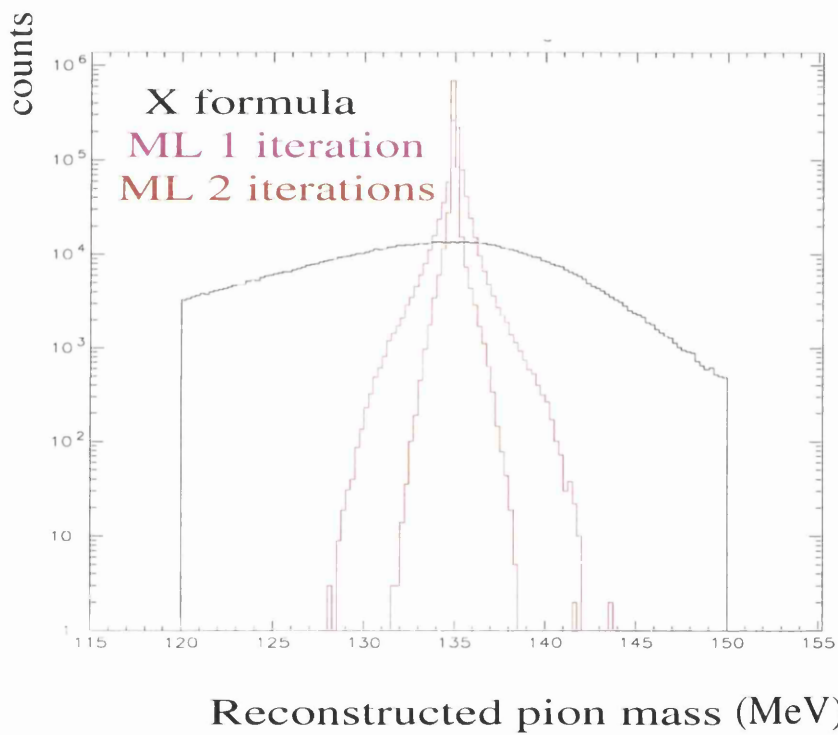
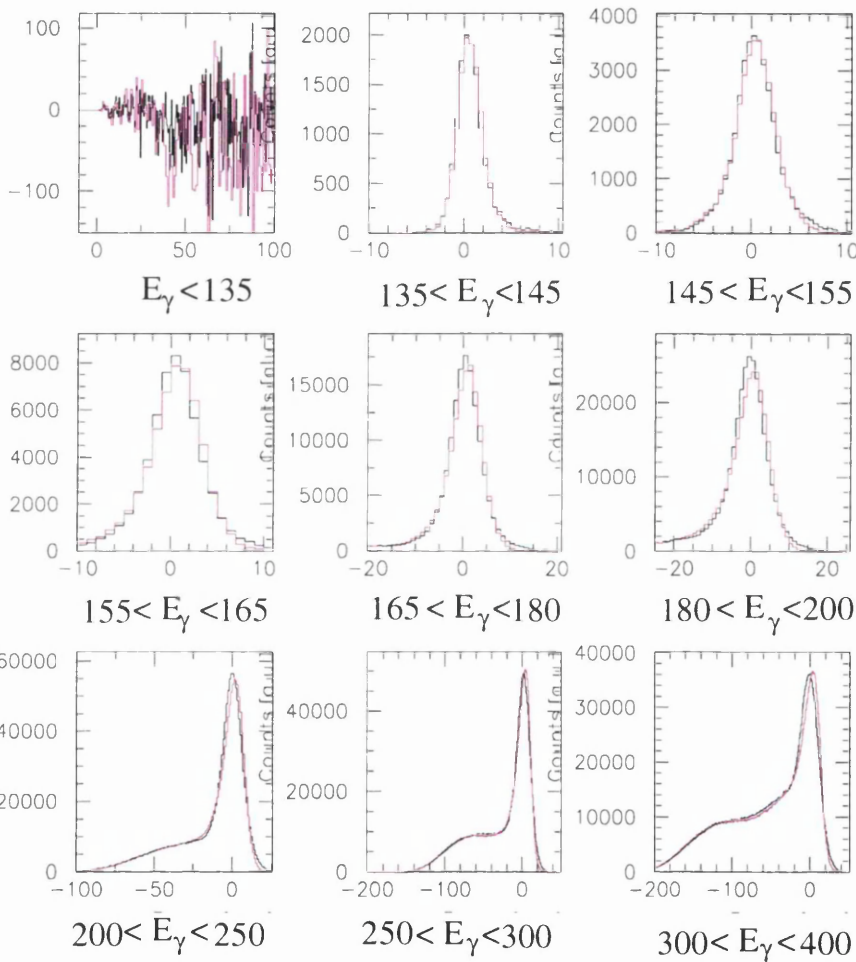


Figure 41: Reconstructed pion mass from the X formula and the MLM with 1 and 2 iterations shown on a logarithmic scale.



X method
MLM

Figure 42: Reconstructed pion missing energy using the X formula and the MLM for various incident photon energy bins. The horizontal axes of the spectra are in units of MeV, the vertical axes in units of counts. These spectra were produced using a subset of the ^{12}C data.

4.7 TAPS detection efficiency

Due to the geometry of TAPS (See fig. 13) the efficiency with which TAPS detected pions varied strongly with both pion energy and angle. As TAPS only covered a limited solid angle, a significant fraction of the pion decay photons were not incident on any part of TAPS. The opening angle distribution of the two pion decay photons is strongly correlated with the pion energy (see eq. 29). The pion decay photons were detected in separate TAPS blocks (see section 3.6); either neighbouring TAPS blocks, or blocks separated by one or two other blocks. Pions whose decay photons had an opening angle for which TAPS provided little solid angle, were unlikely to be detected. Pions whose decay photon opening angle matched the angle between TAPS blocks had a higher likelihood of being detected.

Simulations were carried out by Sanderson [38] using the software GEANT 3.21 [40], using a Monte Carlo random number generator to simulate pions of discrete energy and lab angle. The pions were generated inside the target. The photon interactions in the target, the beam pipe, the CPV detectors and the TAPS elements were simulated. Resultant particles were tracked until their energy was less than 1 MeV. The effect of light collection in the TAPS elements was included. The simulated data were analysed using the same analysis with the same cuts as were applied to the experimental data, and the detection efficiency was determined for the discrete values of pion energy and angle. The variation in detection efficiency with pion energy and angle for ^{12}C is shown in figures 44 and 45. 10^5 pions were simulated for each combination of pion energy and angle. The statistical error in the detection efficiency was about 3 %. Simulating a greater number of pions for each combination of pion energy and angle would have decreased this error. As the contribution to the error in the cross section due to the uncertainty in the detection efficiency was comparable to the contribution from the estimate of the number of coherent events, and as the simulations took a significant amount of time to generate, simulations of a greater number of pions were not carried out. Information about the timing of the TAPS signals was not provided by the GEANT simulation. The efficiency obtained therefore did not allow for the reduction produced by the cuts applied to the time spectra, and corrections

were made to the simulated detection efficiency to compensate for this (see section 4.8).

The shape of the distribution of reconstructed pion mass from the simulation and the data agreed well (see fig. 43) and the estimated difference in the reduction in the coherent peak when the cut on the reconstructed mass was applied was less than 1 % [46].

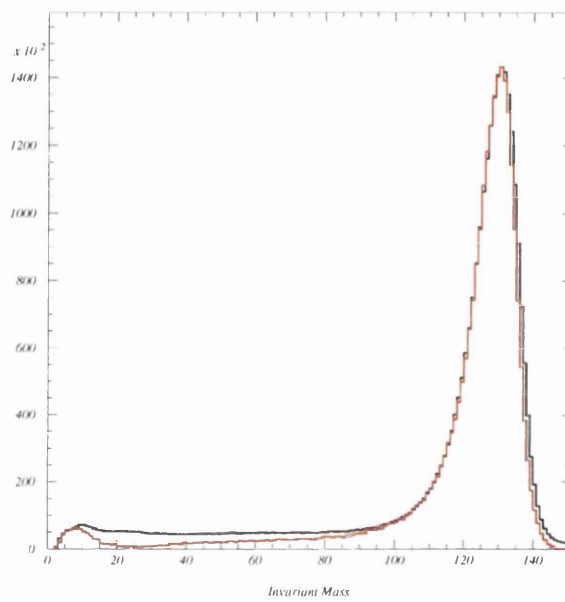


Figure 43: Reconstructed pion mass - simulation compared with data for ^{12}C . Black line - experimental data; red line - simulated data.

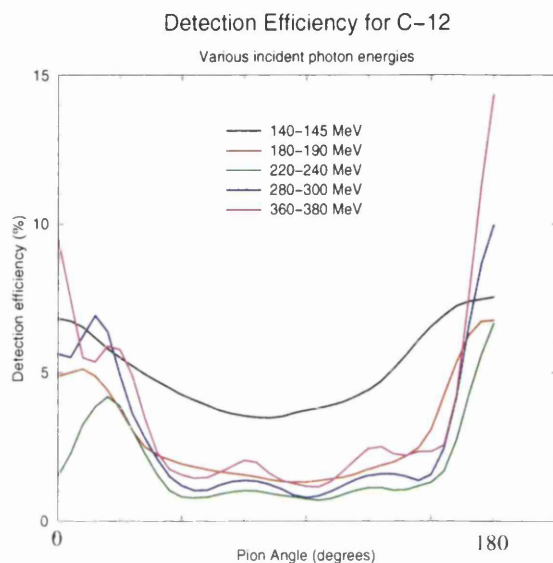


Figure 44: TAPS detection efficiency as a function of pion lab angle for various pion energies.

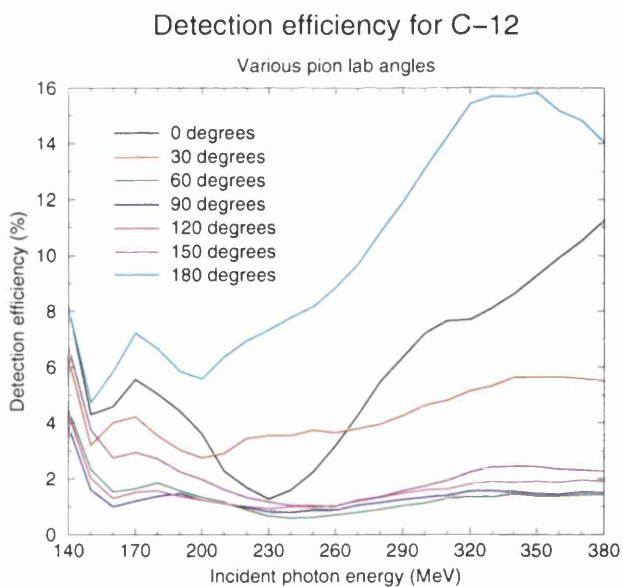


Figure 45: TAPS detection efficiency as a function of the incident photon energy for various pion angles.

4.8 Cross sections

The differential cross section for a particular range of photon energies and pion angles was initially calculated as shown in eq. 40:

$$\frac{d\sigma_u(E_\gamma, \theta_\pi)}{d\Omega} = \frac{N_\pi}{\epsilon_{tagg} \rho N_{TS} N_{TC} \Omega \Gamma_{\gamma\gamma}} \quad (40)$$

where

$\frac{d\sigma_u(E_\gamma, \theta_\pi)}{d\Omega}$ is the uncorrected cross section. The corrections are described below.

N_π is the number of neutral pions detected in TAPS (see section 4.5.3) in that E_γ, θ_π range

ϵ_{tagg} is the tagging efficiency (see section 3.7) for that E_γ .

ρ is the target density, measured in nuclei/cm².

N_{TS} is the number of tagger scaler counts, i.e. the number of tagging electrons from a particular tagger channel.

N_{TC} is the number of tagger channels corresponding to the incident photon energy region

Ω is the solid angle of the angular bin in steradians.

$\Gamma_{\gamma\gamma}$ is the branching ratio of the decay ($\pi^0 \rightarrow \gamma \gamma$) : 98.89%.

Several corrections were applied to each value of the cross section:

$$\frac{d\sigma(E_\gamma, \theta_\pi)}{d\Omega} = \frac{d\sigma_u(E_\gamma, \theta_\pi)}{d\Omega} \frac{1}{\epsilon_{TAPS}} F_{\gamma\gamma} F_{TT} F_{E_{miss}} \quad (41)$$

where

$\frac{d\sigma(E_\gamma, \theta_\pi)}{d\Omega}$ is the corrected cross section.

ϵ_{TAPS} is the TAPS detection efficiency (see section 3.7).

$F_{\gamma\gamma}$ is a factor correcting for events due to neutral pions having been removed with the cut on the time difference between the two pion decay photons. This was calculated by fitting a Gaussian function to the spectrum of the pion decay photon time difference and estimating the fraction lost in the cut.

F_{TT} is a factor correcting for events due to neutral pions having been removed with the cut on the time difference between the tagger signal and the TAPS trigger. This was estimated in a similar way to $F_{\gamma\gamma}$.

$F_{E_{miss}}$ is a factor correcting for events due to neutral pions having been cut away with the cut on the missing energy (see section 4.5.4).

The integrated cross section was obtained by integrating the differential cross section:

$$\sigma = \int \frac{d\sigma}{d\Omega}(E_\gamma, \theta_\pi) d\Omega \simeq 2\pi \sum_\theta \frac{d\sigma}{d\Omega}(E_\gamma, \theta_\pi) \sin\theta \quad (42)$$

4.9 Errors in the cross sections

The statistical error depends mostly on the number of counts in the coherent peak region, but there is also a contribution due to the non-coherent background. It is therefore large when the coherent cross section is small and the non-coherent contribution is relatively large - for large pion lab angles. The statistical error in the area of the coherent part of the missing energy distribution was obtained from the fitting routine. As the detection efficiency was determined by a Monte Carlo procedure (see section 4.7), it also contained a statistical error estimated to be 3 % for all combinations of pion energy and lab angle. The contributions to the error in the cross section from the fitting and the detection efficiency simulation were combined in quadrature to produce the statistical errors shown in the cross section plots and tables.

A systematic error also arose from the fitting of the missing energy distribution. An estimate of the fractional variation in the area of the fitted Gaussian functions for small variations in the fit parameters is shown in table 9. For distributions where the missing energy peak was well defined by a single Gaussian function and the background was small (see fig. 35), the systematic error was small.

For distributions where the peak was well defined but the background significant (see fig. 36), the systematic error was still quite small. The accuracy of the fit relies on the background being fitted well with the Fermi function - that is that the nuclear excited

states production process does not contribute significantly and that the Fermi function describes the fall-off of the quasi-free distribution well - and on knowing the peak position of the missing energy distribution for the coherent events. Where the apparent peak position of the missing energy distribution has not shifted significantly away from E^i , the nuclear excited states were not thought to contribute significantly. The distribution of the quasi-free processes was known to have its peak so far below the peak of the coherent distribution that only the fall-off needed to be fitted.

For the distributions where the apparent peak position has moved significantly away from E^i (see figures 37 and 38), the fit relied on the assumption made about the coherent peak position. Particularly for the distributions where the fitted coherent peak constitutes a small fraction of the total yield, the area of the fitted coherent peak is strongly dependent on the selected coherent peak position.

The estimated systematic error in the cross sections is 0.1 - 1.5 % in the pion angle and energy region where the first maximum occurs in the differential cross section, as the missing energy distributions are well described by Gaussian fits. In the region of the first minimum of the differential cross sections, and for pion angles greater than that where the first minimum occurs, the systematic error is considerably larger, typically 20-40 %, as the non-coherent events make a considerable contribution to the missing energy distribution and as the peak position of the coherent missing energy distribution is not well defined.

The error in the tagging efficiency was about 0.7%. The error in the target thickness was 0.02%. As the contribution from these errors to the error in the cross section was negligible compared with the contributions from the TAPS detection efficiency and the missing energy fits, they were not included in the calculation of the error in the cross section.

Table 9: Estimate of the systematical error in the fit to the missing energy distribution for selected incident photon energies and angles. The numbering of the fit methods is as explained in section 4.5.4

E_γ (MeV)	θ_π ($^\circ$)	Method used for fit	Estimated systematic error (%)
145-150	10-15	1	2.6
	45-50	1	0.5
	90-95	1	1.2
	135-140	1	1.2
200-220	10-15	1	0.05
	45-50	2	0.1
	90-95	3	38.0
	135-140	3	23.9
340-360	10-15	3	6.4
	45-50	3	9.3
	90-95	3	29.9

4.10 Data from the NaI detectors

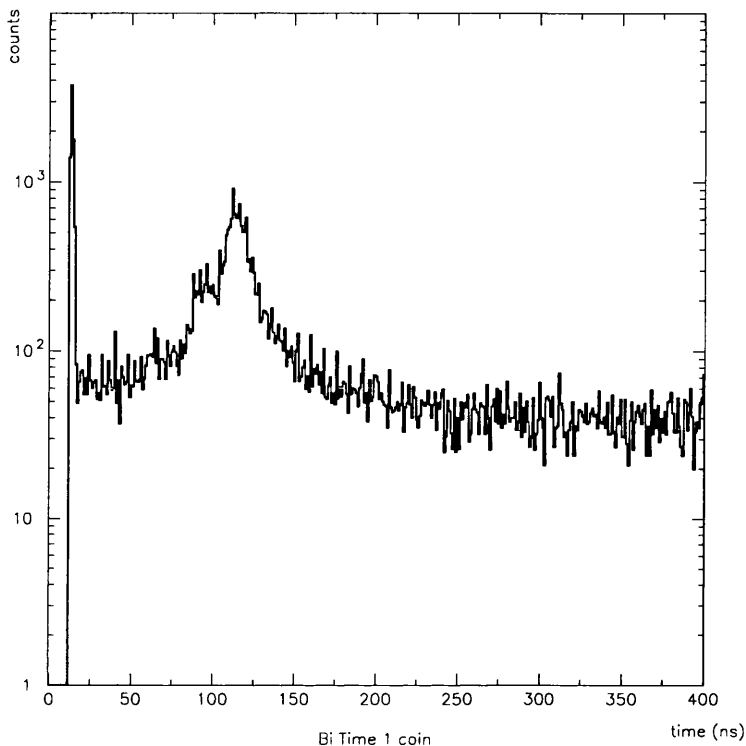


Figure 46: Bicorn NaI time spectrum for ^{12}C for a subset of the data

The time spectrum from the Bicorn NaI from the ^{12}C data is shown in fig. 46. A peak containing events coincident with the TAPS trigger is clearly visible.

The energy spectrum from the Bicorn NaI from the ^{12}C data is shown in fig. 47. The pedestal is not shown. This spectrum contains events which had a coincident time signal in the TDC belonging to the Bicorn NaI, which had an associated missing pion energy in the region $(-40,20)$ MeV and which were coincident with the tagger time signal.

The spectrum contains considerable background, but a peak, due to the nuclear excited state at 4.4 MeV, is visible. Nuclear decay photons from the nuclear excited state at 15.0 MeV were not seen in the NaI detectors. The energy spectrum from the Harshaw NaI was similar.

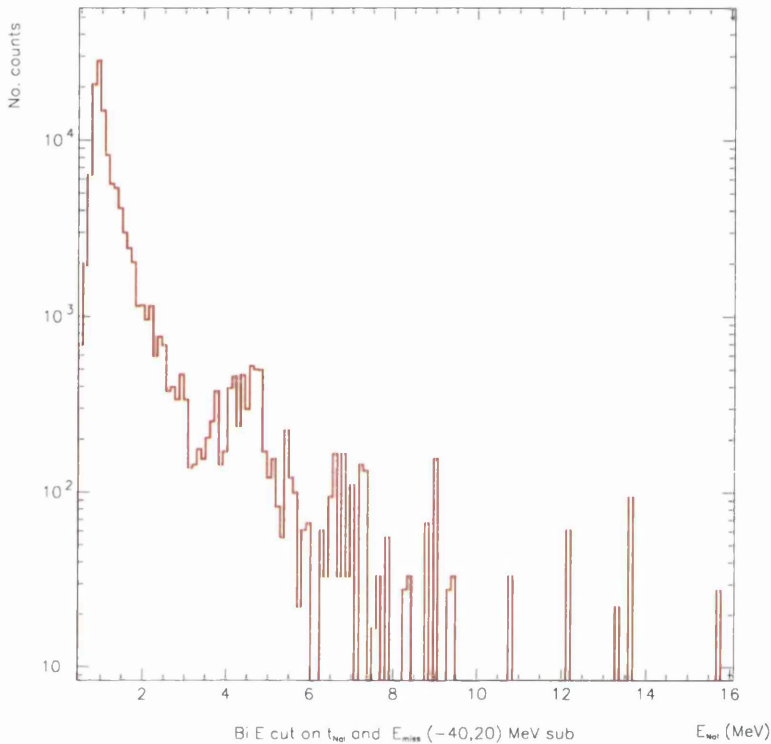


Figure 47: Bicon NaI energy spectrum for ^{12}C . The events selected have a prompt time signal in the NaI TDC, an associated pion missing energy in the region $(-40,20)$ MeV and are in prompt coincidence with the tagger time signal.

The detection efficiency of the NaI detectors for 4.5 MeV photons emitted isotropically from the target was estimated from GEANT simulations carried out by Sanderson [40] [46] to be 3 %.

The angular distribution of the 4.4 MeV nuclear decay photon produced via neutral pion production from ^{12}C has been calculated by [42]. According to this calculation, the distribution has a minimum at $\theta_\gamma = 90^\circ$, where θ_γ is the lab angle between the pion and the nuclear decay photon - the differential cross section at $\theta_\gamma = 90^\circ$ is approximately a factor of 2 less than at $\theta_\gamma = 30^\circ$. As TAPS was positioned in the horizontal plane, it detected mostly neutral pions emitted in the horizontal plane. Hence, the distribution of

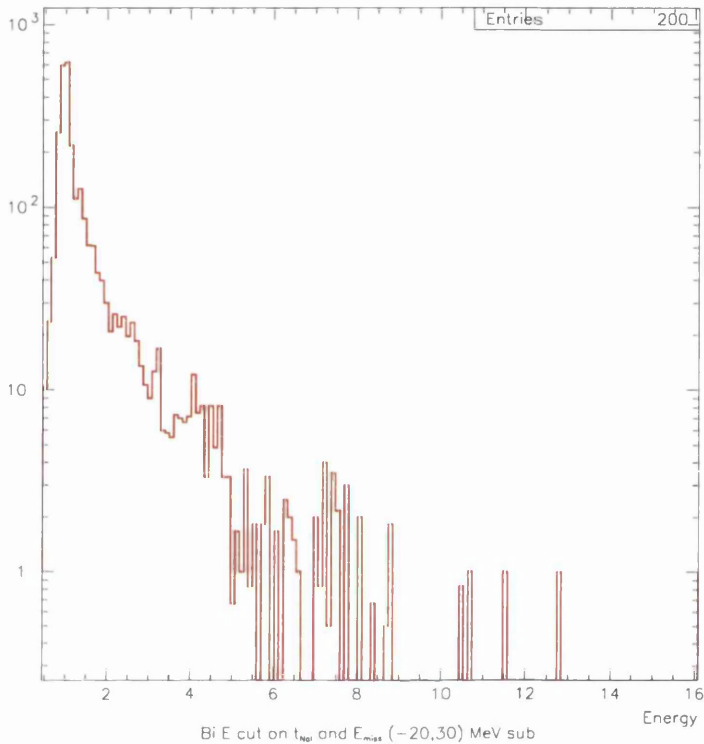


Figure 48: Bicon NaI energy spectrum for ^{40}Ca selecting events which had a coincident time signal in the TDC belonging to that NaI, which had an associated missing pion energy in the region $(-40,20)$ MeV and which were coincident with the tagger time signal.

the nuclear decay photons which could be detected in coincidence with the pions detected in TAPS had a minimum in the direction perpendicular to horizontal, i.e. where the NaI detectors were positioned. An upper limit on the neutral pion production cross section due to the 4.4 MeV nuclear excited state can be obtained by multiplying the cross section obtained by selecting the 4.4 MeV nuclear decay photons detected in the NaI detectors by a factor of 2.

The Bicon spectrum for ^{40}Ca is shown in fig 48. There are no convincing peaks at 3.7 and 4.5 MeV which might indicate populations of the low lying states in ^{40}Ca . At higher energies, there are several states which would not be resolved in the NaI, but the

lack of strength in fig. 48 suggests a very small population of the excited states of higher energy.

5 Results and discussion

Figures 49 - 70 show the measured cross sections for coherent π^0 production from ^{12}C and ^{40}Ca . The error bars shown are statistical. The data are compared with results from Koch et al. [17] [18] and Schmitz [19], with preliminary results from Krusche [20] and with theoretical model predictions using the PWIA, DWIA and DREN (see sections 2.3-2.5).

The theoretical model predictions were made for single values of incident photon energy E_γ , with E_γ in 10 MeV steps between the values of 140 and 380 MeV. These predictions were averaged to correspond to the E_γ bins used in the data, for all E_γ bins except $E_\gamma = 135\text{-}140$ MeV. No theoretical calculations were available in the region $135 < E_\gamma < 140$ MeV so the data from this E_γ bin are compared with the theoretical predictions for 140 MeV.

5.1 ^{40}Ca

The differential and integrated cross sections for ^{40}Ca show the expected characteristics. The integrated cross section increases with E_γ from zero at the neutral pion production threshold to a maximum value at about $E_\gamma = 225$ MeV, somewhat below the Δ resonance, and then decreases with increasing E_γ .

The differential cross sections have a diffraction-like shape with one or several maxima separated by minima. The magnitudes of the maxima decrease with increasing pion lab angle. The pion lab angles at which the maxima and minima occur decrease with increasing incident photon energy. A first minimum and second maximum appears for $E_\gamma > 160$ MeV. An indication of a second minimum and a third maximum appears for $E_\gamma > 280$ MeV.

The ^{40}Ca data are compared with experimental data from [18], preliminary experimental data from [20] and with theoretical model predictions from [23].

5.1.1 Comparison with other experimental data

Figures 54 - 56 show the differential cross sections from preliminary data from [20] compared with the present result for $E_\gamma = 200$ MeV (a weighted average of the results for $190 < E_\gamma < 200$ and $200 < E_\gamma < 220$ MeV was used to obtain this distribution), $280 < E_\gamma < 300$ MeV and $340 < E_\gamma < 360$ MeV and with theoretical predictions from [23].

The peak positions in the two data sets agree reasonably well, but the magnitude of the present peak cross section is greater than that from [20] at $E_\gamma = 200$ MeV, similar at $E_\gamma = 290$ MeV and smaller at $E_\gamma = 350$ MeV.

This discrepancy could be partly due to systematic variations in the separation between coherent and non-coherent events (see section 4.5.4), particularly at larger pion angles, but in the present data these errors are too small to completely explain the difference between the two data sets. The discrepancy could also be partly due to errors in the TAPS detection efficiency. The detection efficiency was obtained from simulations using discrete values of pion energy and angle (see section 4.7). For the higher pion energies, the non-uniform distribution of the detectors with pion lab angle results in a predicted detection efficiency which varies between 2 and 10 % as a function of pion lab angle (see fig. 44). These variations are probably larger for the set-up in [20] as only 5 TAPS blocks were available to cover the whole angular range, whereas 6 blocks and the FW (equivalent to 8 TAPS blocks in total) were used in the present experiment. The discrepancy between the two data sets in the region of the first maximum would imply errors of 20-30 % in the simulated detection efficiency, but although the present simulation has been investigated in some detail [38], no such systematic errors have been found and the discrepancy is not understood.

At backward pion lab angles beyond the first minimum, there are also significant discrepancies between the two sets of experimental results. The statistical accuracy and the pion energy resolution is slightly better in the present work, and whereas differential cross sections were obtained down to about $10 \mu\text{b}$ in the results from [20], the present work obtained values down to about $1 \mu\text{b}$. The differential cross sections from the present result are generally smaller than those from [20] at backward pion lab angles. The over-

all shape of the differential cross sections from the present work also agrees better than those from [20] with the theoretical predictions. These remarks suggest that significant non-coherent yield is included in the results from [20].

In fig. 57, the differential cross section is shown for the present results for $160 < E_\gamma < 170$ MeV and from [18] for $E_\gamma = 164$ MeV. The two cross sections are in reasonable agreement. At low values of θ_π , the data from [18] disagrees with the present result. The differential cross section from [18] does not vanish as θ_π approaches 0° , where the $\sin(\theta_\pi)$ dependence (see eq. 6) should force the value of the cross section to zero. The errors are greater in the results from [18] than in the present result. This is probably because the data was obtained using a Pb-glass detector which had quite poor energy resolution compared with BaF₂, making it more difficult to select coherent events. This selection could only be done by making a cut on the opening angle between the pion decay photons and this resulted in a low detection efficiency for the pions.

The two experimental data sets agree quite well in the region of the first maximum and first minimum. Both experimental data sets show a second maximum but it is better defined in the present result.

Fig. 59 shows the integrated cross section in the E_γ region 135-170 MeV from the present data compared with results on the coherent and the total (nuclear excited nuclear state plus coherent production) cross section [18] for 158-168 MeV. The present results reasonably well with the coherent cross sections, suggesting that the separation between coherent and non-coherent events in the present data was reasonably successful.

5.1.2 Comparison with theoretical models

Figures 49 - 53 and 58 show the differential and integrated cross sections for ^{40}Ca compared with the three theoretical models.

The PWIA clearly does not provide a good description of the results. The integrated cross section from the PWIA differs from the experimental data by about 25% close to the pion production threshold, and the difference increases in the Δ region around 300 MeV. The positions of the minima in the differential cross section (see tables 10-12) appear at

systematically lower angles in the PWIA than in the experimental data.

The importance of including the final state interactions (FSI) in the description of the pion production process is obvious as the DWIA gives a much better description of the experimental data than the PWIA. As well as increasing the predicted cross section in the threshold region, the DWIA treatment introduces a strong imaginary potential in the Δ region which describes absorption of the pion in the nucleus and brings the predicted cross section closer to the experimental results. It also shifts the angles where the minima occur in the differential cross sections closer to those in the experimental data. Although the agreement with the experimental results is improved in the DWIA model, there are still discrepancies between the DWIA predictions and the experimental data and these may indicate that the strength of the FSI in the model is incorrect for some incident photon energies.

The position of the first maximum (see table 10) is significantly lower than that predicted by the DWIA close to the π^0 -production threshold, but this discrepancy decreases with E_γ . For $160 < E_\gamma < 170$ MeV, the lowest incident photon energies where the first minimum appears in the data, the minimum position in the data and the DWIA agree quite well. For $180 < E_\gamma < 190$ MeV, there is a discrepancy in the minimum positions from the present data and the DWIA of about 15° . This discrepancy then decreases with increasing E_γ and for $320 < E_\gamma < 340$ MeV, the position of the first minimum from the present result and from the DWIA agree quite well. If these discrepancies are a direct indication that the distortion used in the distorted wave impulse approximation is incorrect, it would perhaps be expected that the discrepancies would be greatest where the difference between the plane and distorted wave models is greatest. However, this may not be the case as the pion-nucleus interaction has real and imaginary parts whose effects on some features of the angular distribution can cancel and as the parameter describing the distortion may not be greatest where the effect of the interactions is largest.

The same applies to the discrepancy in the position of the second maximum (see table 11) between the present data and the DWIA which follows the same trend. It is negligible for the lowest values of E_γ where the second maximum appears ($160 < E_\gamma < 170$ MeV) ,

then increases with E_γ , is greatest for $180 < E_\gamma < 190$ MeV and then decreases with E_γ . It is negligible for $E_\gamma > 320$. The position of the third maximum is harder to identify accurately, but the data suggest (see tables 12 -14) that discrepancies between the present data and the DWIA exist.

The largest of the discrepancies occur in the magnitudes of the second and third maxima between the present results and the DWIA and the DREN and these do occur in the region where the predictions are very sensitive to the distortion.

In the lowest E_γ region where a second maximum appears in the present data ($160 < E_\gamma < 170$ MeV) (see tables 10-12), the magnitude of the second maximum in the DWIA is a factor of 5 lower than the present data. This discrepancy decreases with increasing E_γ , and at the highest values of E_γ available in the data ($360 < E_\gamma < 380$ MeV), the data and the models agree quite well. The discrepancy in the magnitude of the third maximum between the present result and the DWIA shows the same trend: it is greatest where the third maximum first appears in the data ($240 < E_\gamma < 260$ MeV) and then decreases with increasing E_γ . The discrepancies do suggest that the strength of the final state interaction used in the DWIA needs some modification at some energies. A systematic investigation of the sensitivity of the theoretical predictions to the strength of the final state interaction would be informative.

The minima in the differential cross section in the data are not as deep as those predicted by the models. This could be due to yield from non-coherent processes ‘filling in’ the minima - the separation between coherent and non-coherent processes was difficult (see section 4.5.4) and the selection of the coherent cross section contained systematic errors, which could have included non-coherent yield in the estimate of the coherent cross section. However, it is not likely that this can explain the shape of the angular distributions in the region of the first maximum since it was possible to extract the coherent cross sections which were an order of magnitude smaller at more backward angles and calculations of the incoherent process suggest that it has a relatively smooth angular distribution. Also, the sharpness of the minima from the theoretical calculations varies with photon energy and pion angle.

Although no nuclear de-excitation photons could be identified in the NaI energy spectra, this does not imply that the nuclear excitation pion production process was negligible (see section 5.1.3). It is not possible to determine reliably whether it is nuclear excitation yield or an effect of the final state interactions which causes the minima in the present data to be less deep than predicted by the DWIA and the DREN.

Although some adjustment of the pion-nucleus interaction would improve the agreement between the DWIA predictions and the experimental result, more major modifications are needed in the Δ resonance region, where the cross section from the DWIA model significantly exceeds that from the present data.

As discussed in section 2.6, modifications of the Δ properties inside the nucleus and multiple interactions inside the nucleus should be taken into account to give a good description of the pion production process. This is done in the DREN, where the maximum of the integrated cross section is shifted from 300 MeV in the DWIA model to 225 MeV, in agreement with the present measurements, indicating that the Δ mass used in the DREN is a good description of the modified Δ mass. The cross section is reduced in the DREN treatment compared with the DWIA. For $E_\gamma < 280$ MeV, the data agrees better with the DWIA, for $E_\gamma > 280$ MeV, with the DREN. Increasing the strength of the FSI would further reduce the cross section in both the DWIA and DREN, improving the agreement between the present result and the DWIA but worsening the agreement with the DREN for $E_\gamma < 340$ MeV. This suggests that the parameterisation of the medium modifications and the multiple interactions used in the DREN also require modifications. This is not surprising since the parameterisation used in the DREN is based on data on neutral pion production on the ${}^4\text{He}$ nucleus, whose density distribution is very different from that in heavier nuclei. The present data will allow this parameterisation to be improved.

5.1.3 The nuclear excitation process

The nuclear excited state pion photo-production process is expected to contribute to the total pion photo-production yield. However, as fig. 48 shows, no nuclear decay photons from any particular nuclear excited state could be identified in the NaI spectra.

No theoretical prediction of the nuclear excitation pion photo-production cross section for ^{40}Ca has been found in the literature.

It is possible that the nuclear excitation π^0 -production process makes a small contribution to the total π^0 production process for ^{40}Ca . It is also possible that this contribution is non-negligible, but that the angular correlation of the nuclear decay photons with the pions detected in TAPS with the present set-up is such that few nuclear decay photons were emitted in the direction of the NaI detectors so that their signals could not be separated from the background in the NaI energy deposition spectra. The detection of nuclear decay photons is discussed further in section 5.2.3.

Table 10: Positions of the first maximum and first minimum in the differential cross section for ^{40}Ca

E_γ (MeV)	1^{st} max				1^{st} min			
	($^\circ$) experiment	($^\circ$) PWIA	($^\circ$) DWIA	($^\circ$) DREN	($^\circ$) experiment	($^\circ$) PWIA	($^\circ$) DWIA	($^\circ$) DREN
135-140	59 ± 2	64	65	66	-	-	-	-
140-145	47 ± 2	55	54	55	-	-	-	-
145-150	46 ± 2	52	51	52	-	-	-	-
150-155	43 ± 2	48	48	48	-	-	-	-
155-160	42 ± 2	46	45	45	-	-	-	-
160-170	35 ± 2	42	41	42	-	-	111	111
170-180	34 ± 2	39	38	38	97 ± 2	110	99	99
180-190	32 ± 2	36	35	35	82 ± 2	97	90	90
190-200	30 ± 2	33	32	33	77 ± 2	88	82	82
200-220	27 ± 2	30	29	29	65 ± 2	78	73	73
220-240	22 ± 2	27	26	26	60 ± 2	68	63	63
240-260	20 ± 2	25	23	23	54 ± 2	61	55	55
260-280	19 ± 2	22	21	21	49 ± 2	56	49	50
280-300	17 ± 2	20	19	19	42 ± 2	51	45	46
300-320	15 ± 2	19	17	18	41 ± 2	47	41	42
320-340	15 ± 2	18	16	17	38 ± 2	44	38	39
340-360	15 ± 2	16	15	16	35 ± 2	41	36	37
360-380	15 ± 2	16	15	15	32 ± 2	40	35	35

Table 11: Positions of second maximum and minimum in the differential cross section for ^{40}Ca

E_γ (MeV)	2^{nd} max				2^{nd} min			
	($^\circ$) experiment	($^\circ$) PWIA	($^\circ$) DWIA	($^\circ$) DREN	($^\circ$) experiment	($^\circ$) PWIA	($^\circ$) DWIA	($^\circ$) DREN
135-140	-	-	-	-	-	-	-	-
140-145	-	-	-	-	-	-	-	-
145-150	-	-	-	-	-	-	-	-
150-155	-	-	-	-	-	-	-	-
155-160	-	-	-	-	-	-	-	-
160-170	137 ± 2	-	137	137	-	-	-	-
170-180	122 ± 2	133	128	129	-	-	-	-
180-190	111 ± 2	123	117	118	-	-	-	-
190-200	93 ± 2	114	106	106	-	-	-	-
200-220	84 ± 2	101	93	94	-	-	141	143
220-240	76 ± 2	89	81	81	-	-	121	122
240-260	65 ± 2	79	71	72	-	133	103	104
260-280	60 ± 2	72	64	65	-	112	90	91
280-300	51 ± 2	65	58	59	83 ± 2	99	81	83
300-320	49 ± 2	60	52	54	77 ± 2	90	73	75
320-340	47 ± 2	56	48	50	-	82	69	70
340-360	45 ± 2	52	45	47	-	76	-	66
360-380	42 ± 2	50	44	45	-	73	-	63

Table 12: Positions of the third maximum and minimum in the differential cross section for ^{40}Ca

E_γ (MeV)	3^{rd} max				3^{rd} min			
	($^\circ$) experiment	($^\circ$) PWIA	($^\circ$) DWIA	($^\circ$) DREN	($^\circ$) experiment	($^\circ$) PWIA	($^\circ$) DWIA	($^\circ$) DREN
135-140	-	-	-	-	-	-	-	-
140-145	-	-	-	-	-	-	-	-
145-150	-	-	-	-	-	-	-	-
150-155	-	-	-	-	-	-	-	-
155-160	-	-	-	-	-	-	-	-
160-170	-	-	-	-	-	-	-	-
170-180	-	-	-	-	-	-	-	-
180-190	-	-	-	-	-	-	-	-
190-200	-	-	-	-	-	-	-	-
200-220	-	-	154	153	-	-	-	-
220-240	-	-	142	142	-	-	-	-
240-260	-	-	119	120	-	-	-	-
260-280	-	128	105	106	-	-	139	140
280-300	-	115	93	95	-	-	121	123
300-320	-	104	81	84	-	-	108	109
320-340	-	95	74	77	-	-	102	102
340-360	-	88	-	72	-	-	-	96
360-380	-	85	-	70	-	-	-	90

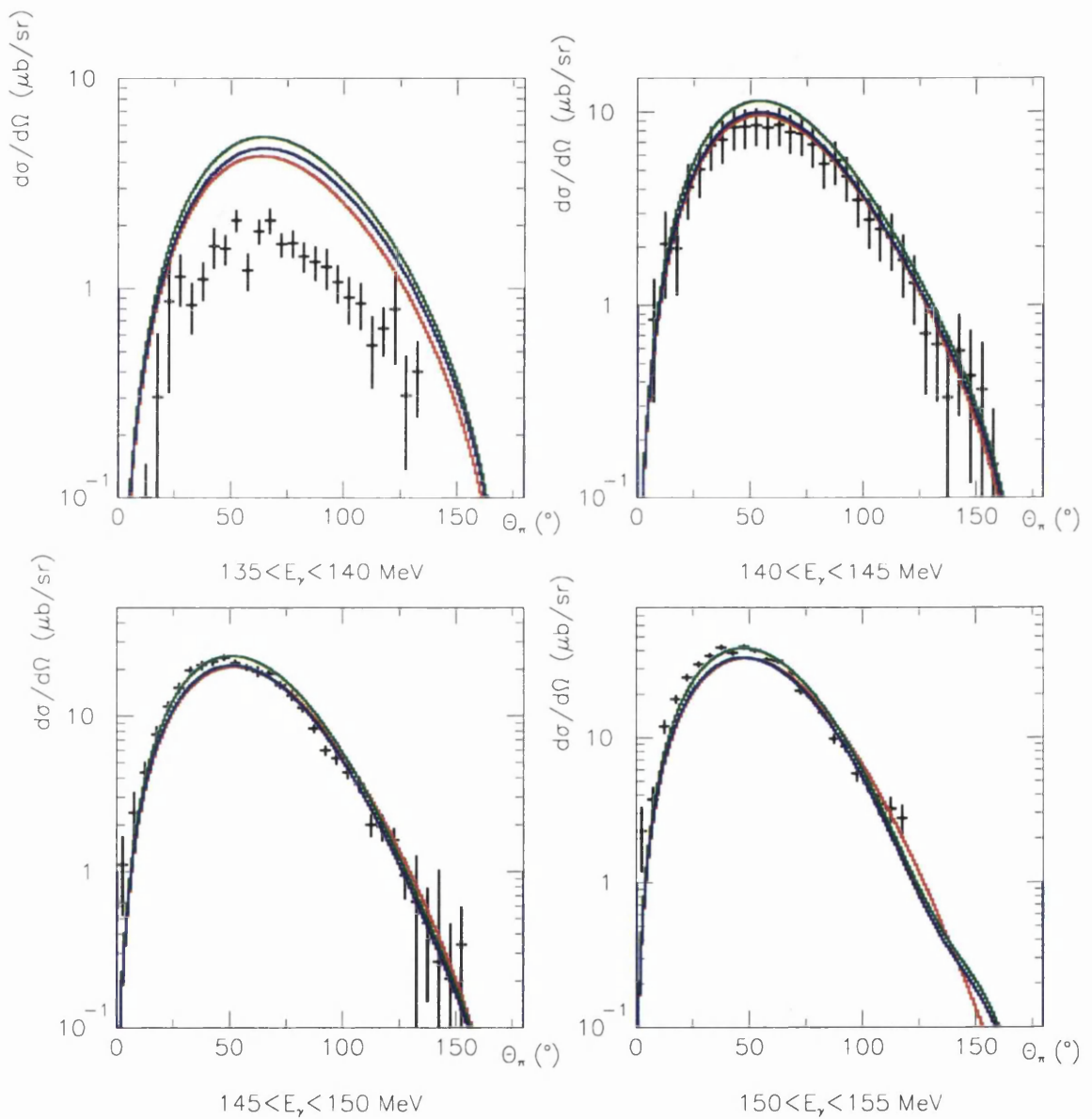


Figure 49: Differential cross sections for ^{40}Ca . Black-present experiment; red-PWIA; green-DWIA; blue-DREN. The theoretical predictions shown with the data where $E_\gamma < 140$ MeV is for $E_\gamma = 140$ MeV. All theoretical results from [23].

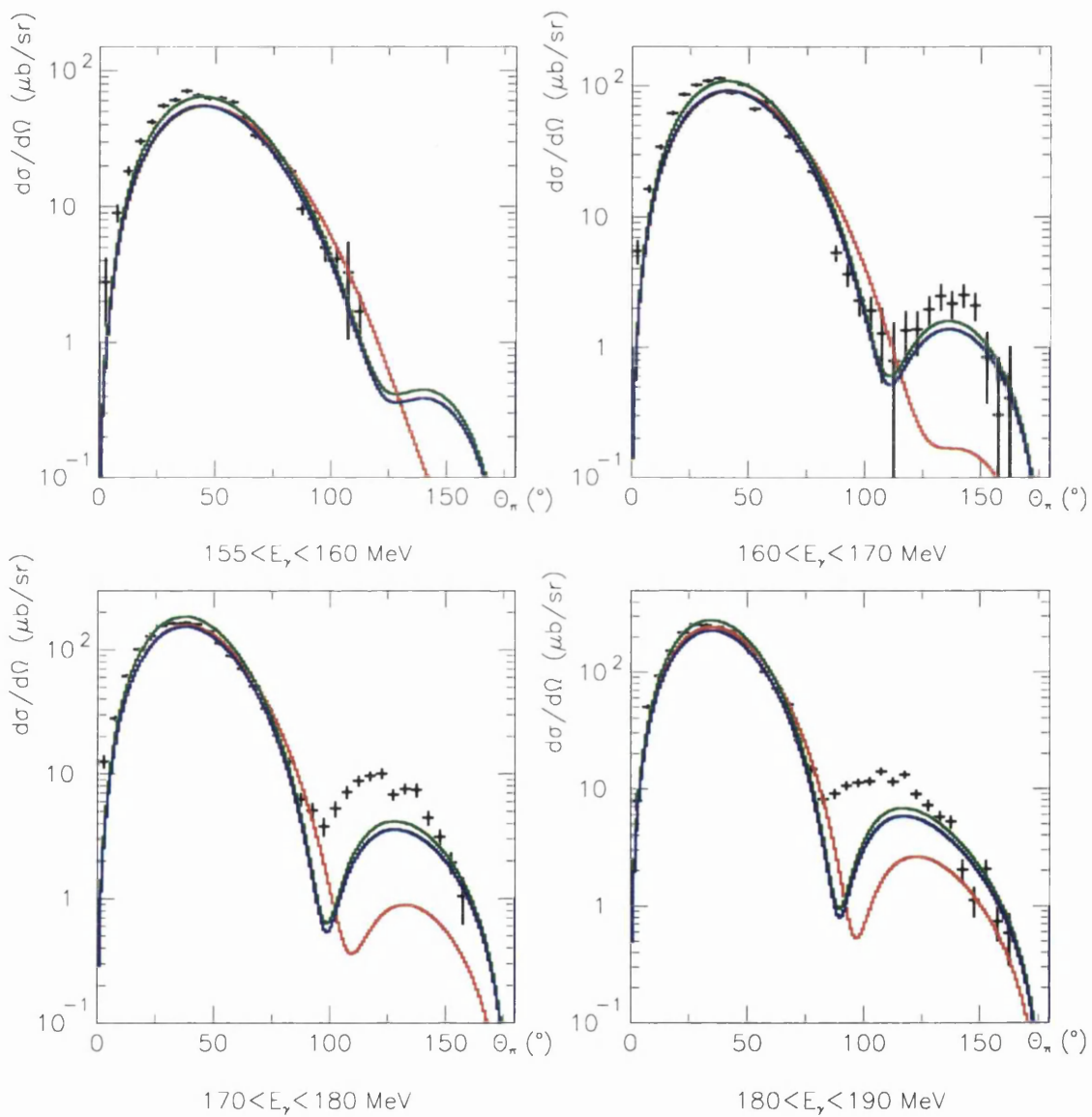


Figure 50: Differential cross sections for ^{40}Ca . Black-present experiment; red-PWIA; green-DWIA; blue-DREN. All theoretical results from [23].

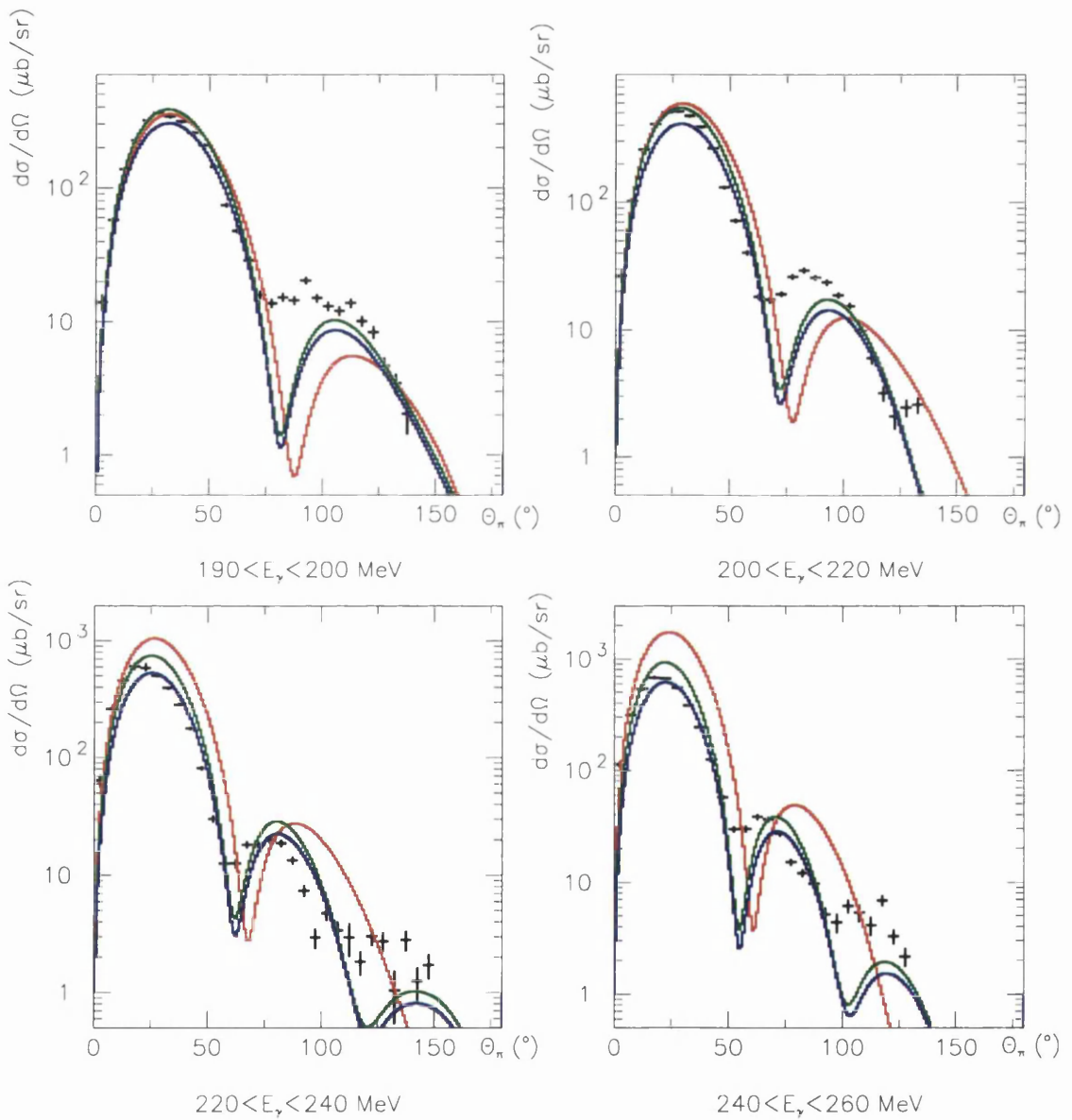


Figure 51: Differential cross sections for ^{40}Ca . Black-present experiment; red-PWIA; green-DWIA; blue-DREN. All theoretical results from [23].

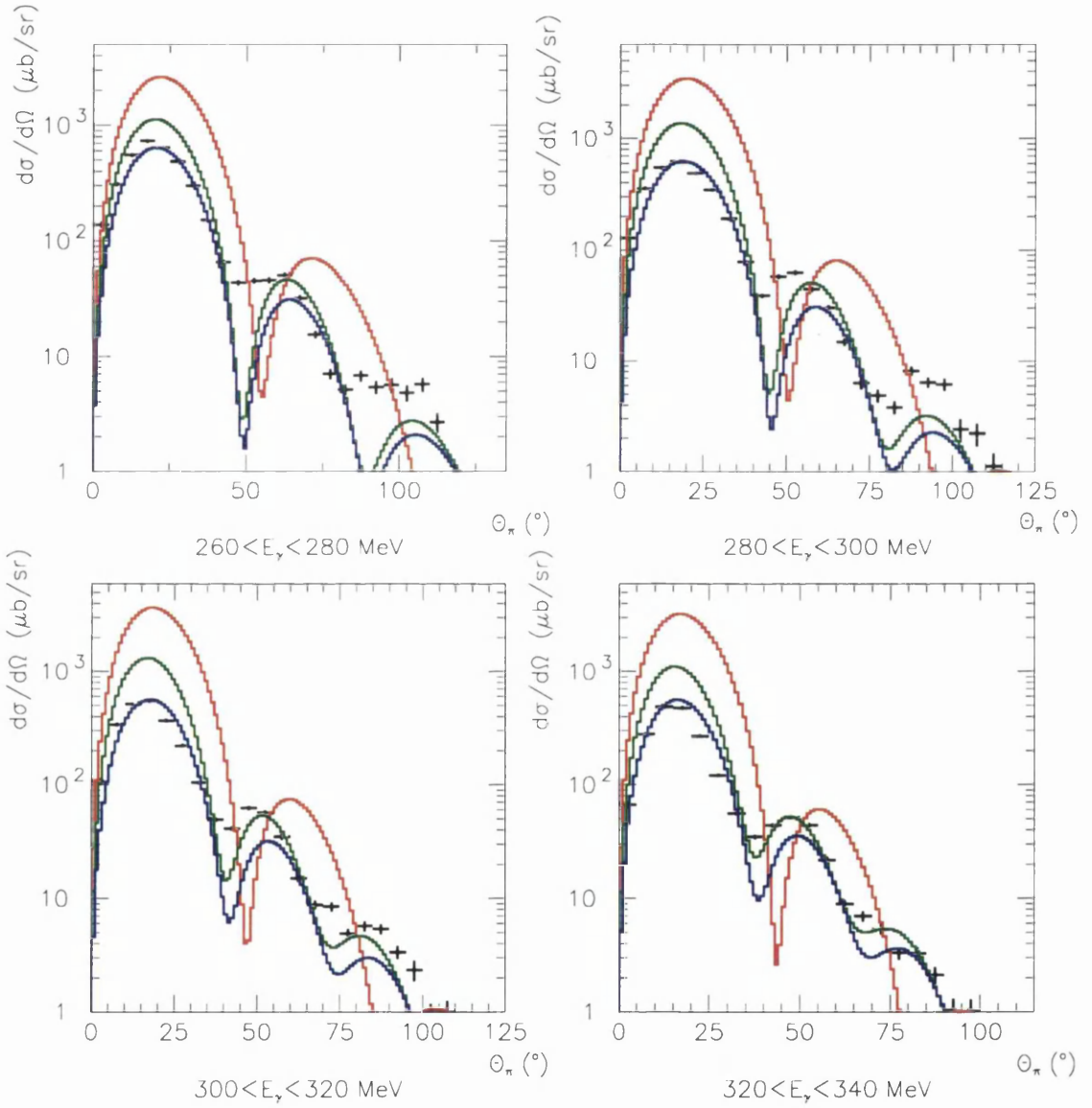


Figure 52: Differential cross sections for ^{40}Ca . Black-present experiment; red-PWIA; green-DWIA; blue-DREN. All theoretical results from [23].

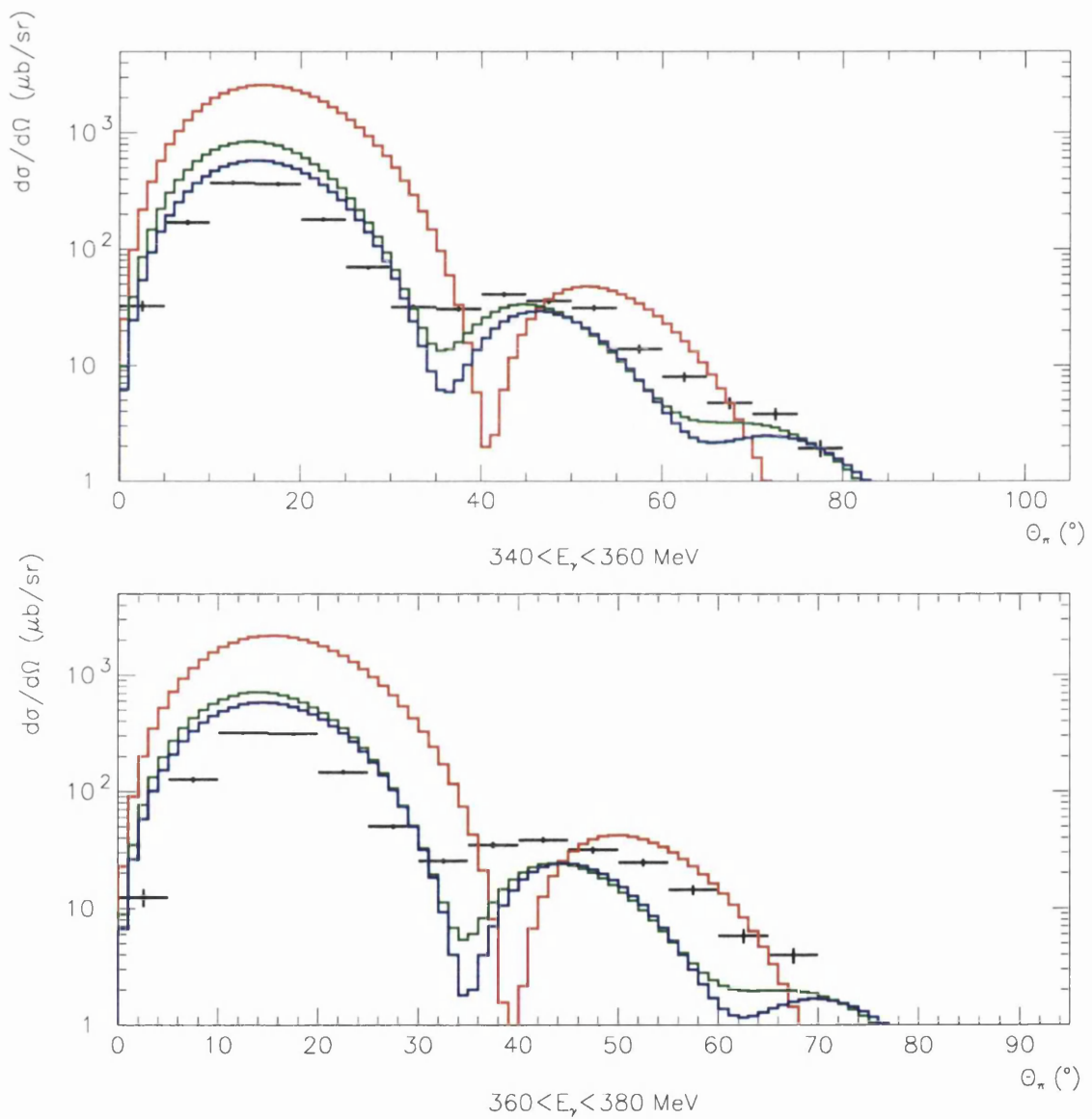


Figure 53: Differential cross sections for ^{40}Ca . Black-present experiment; red-PWIA; green-DWIA; blue-DREN. All theoretical results from [23].

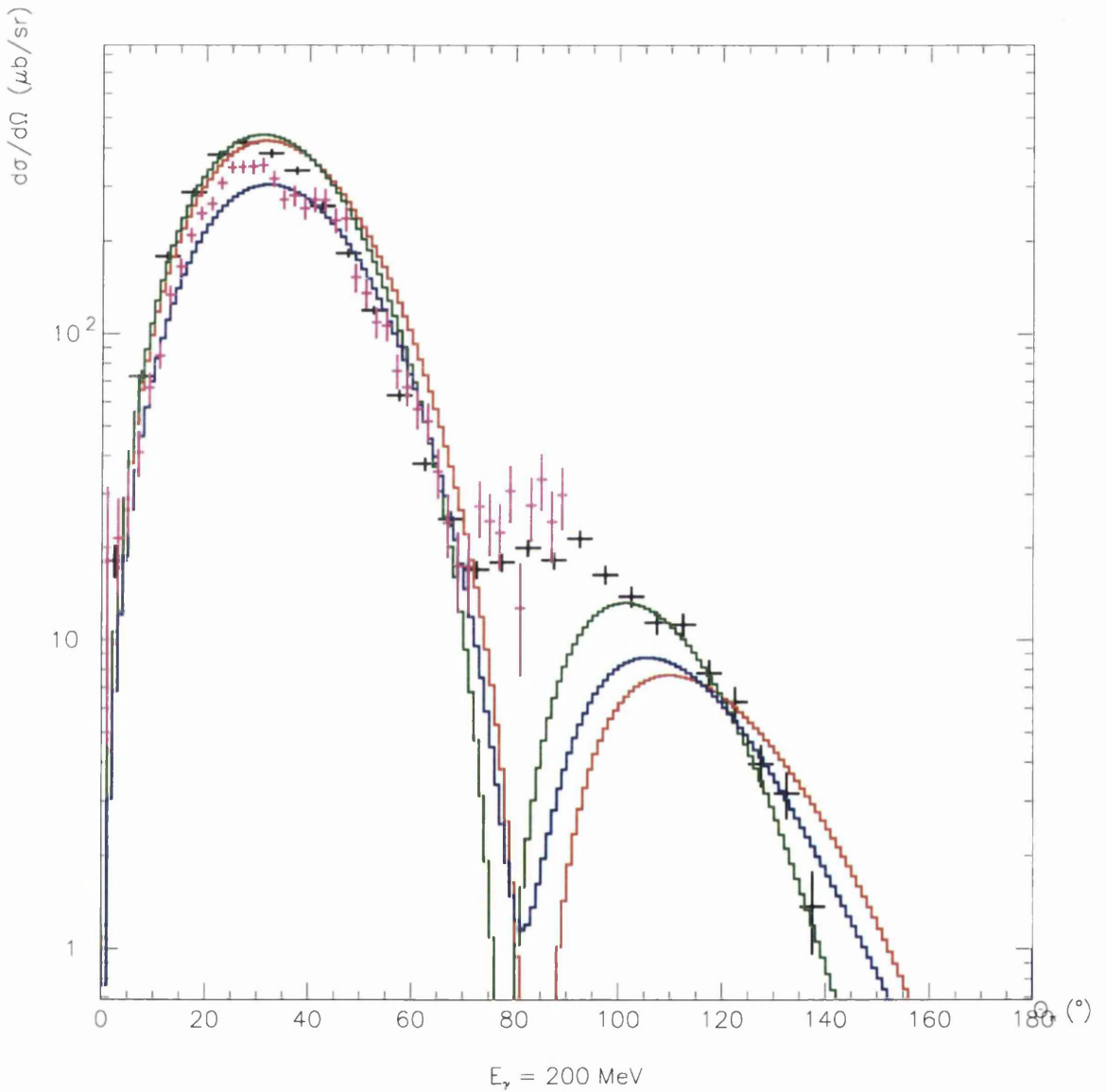


Figure 54: Differential cross section for ^{40}Ca at $E_\gamma = 200 \text{ MeV}$. Black-present experiment; purple-data from [20]; red-PWIA; green-DWIA; blue-DREN. All theoretical results from [23].

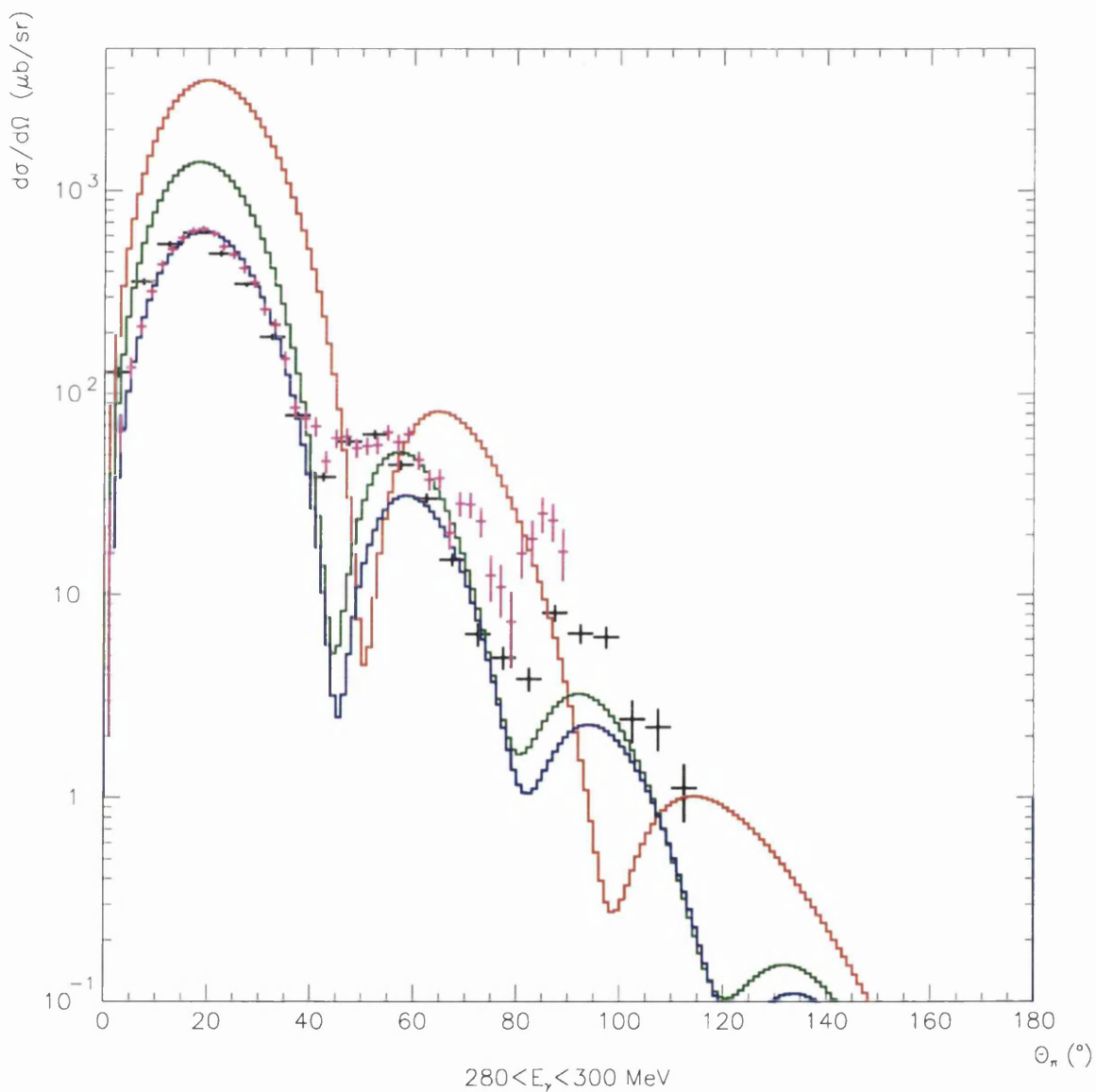


Figure 55: Differential cross section for ^{40}Ca at $E_\gamma = 290 \text{ MeV}$. Black-present experiment; purple-data from [20]; red-PWIA; green-DWIA; blue-DREN. All theoretical results from [23].

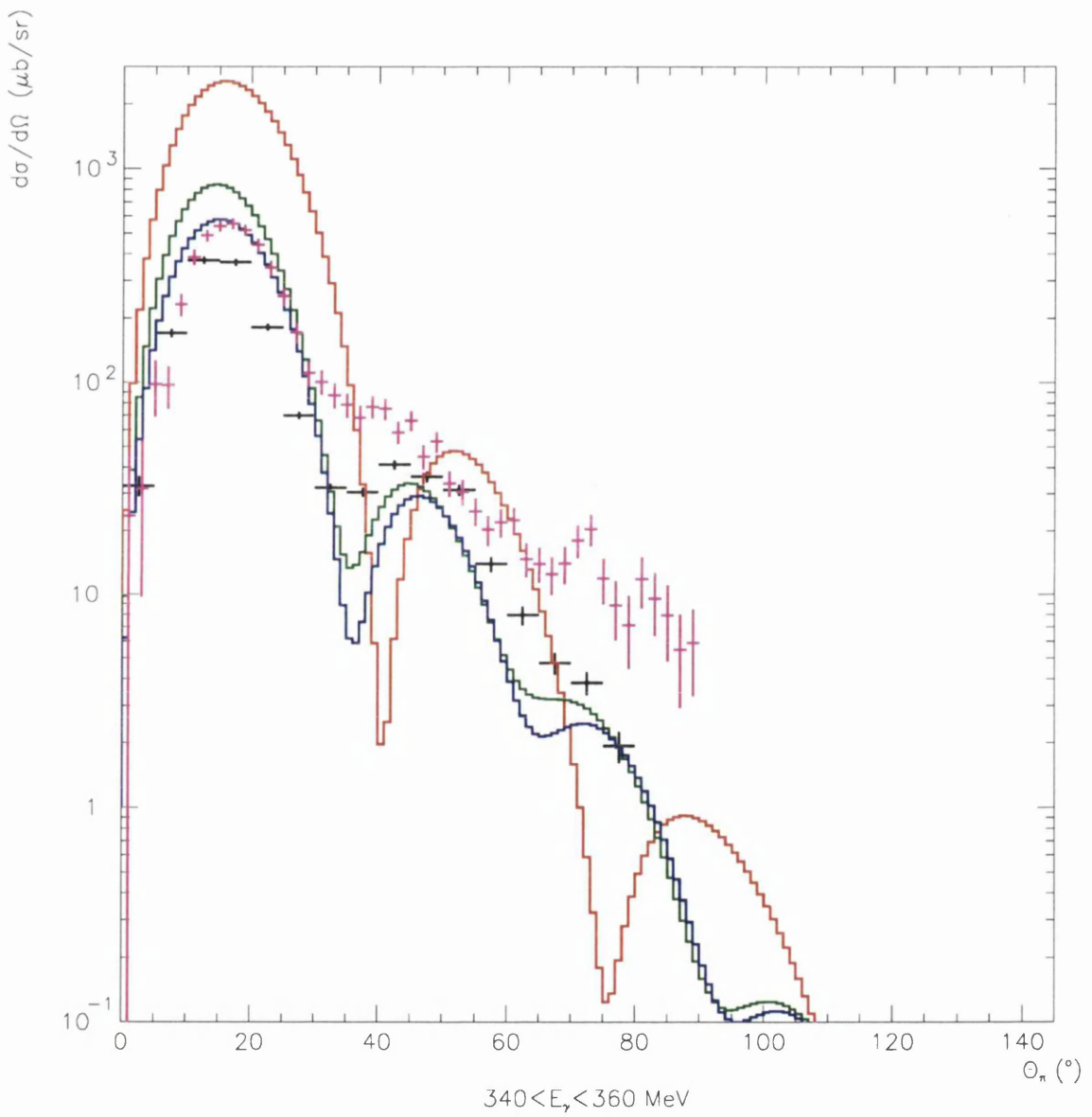


Figure 56: Differential cross section for ^{40}Ca at $E_\gamma = 350 \text{ MeV}$. Black-present experiment; purple-data from [20]; red-PWIA; green-DWIA; blue-DREN. All theoretical results from [23].

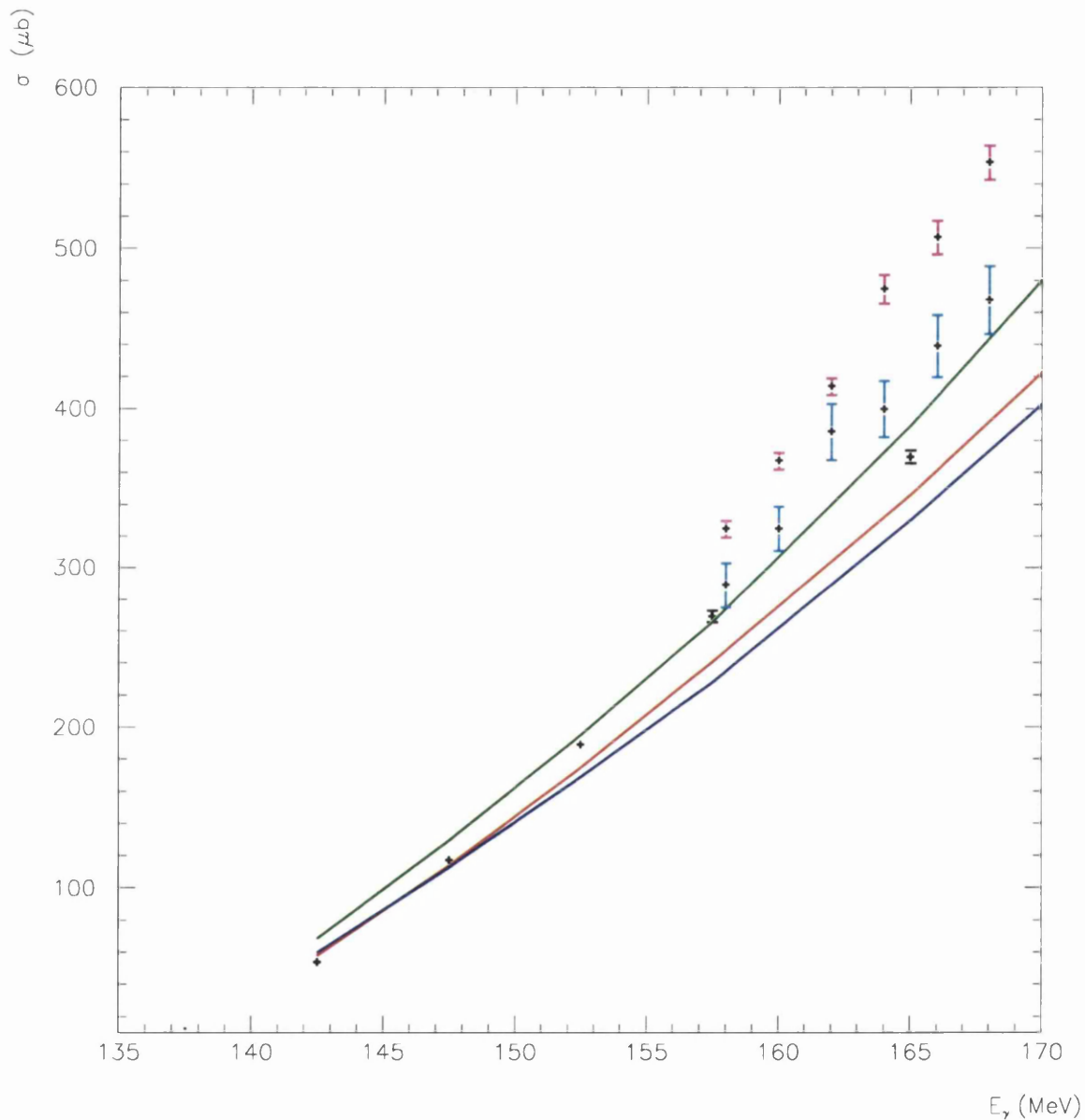


Figure 57: Differential cross section for ^{40}Ca at $160 < E_\gamma < 170$ MeV Black-present experiment; purple-data at $E_\gamma = 164$ MeV from [18]; red-PWIA; green-DWIA; blue-DREN. All theoretical results from [23].

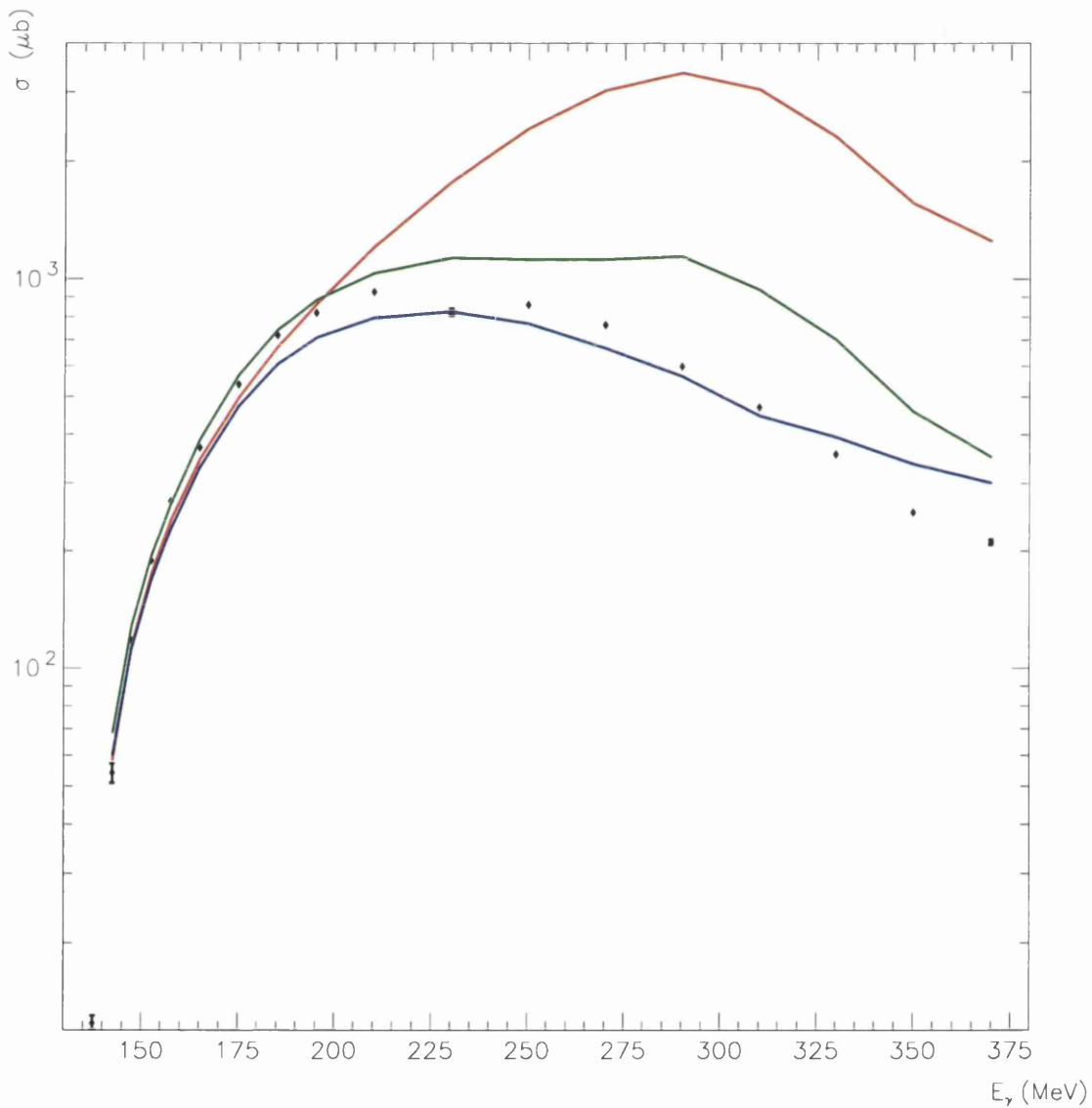


Figure 58: Integrated cross section for ^{40}Ca . Black-present experiment; red-PWIA; green-DWIA; blue-DREN. All theoretical results from [23].

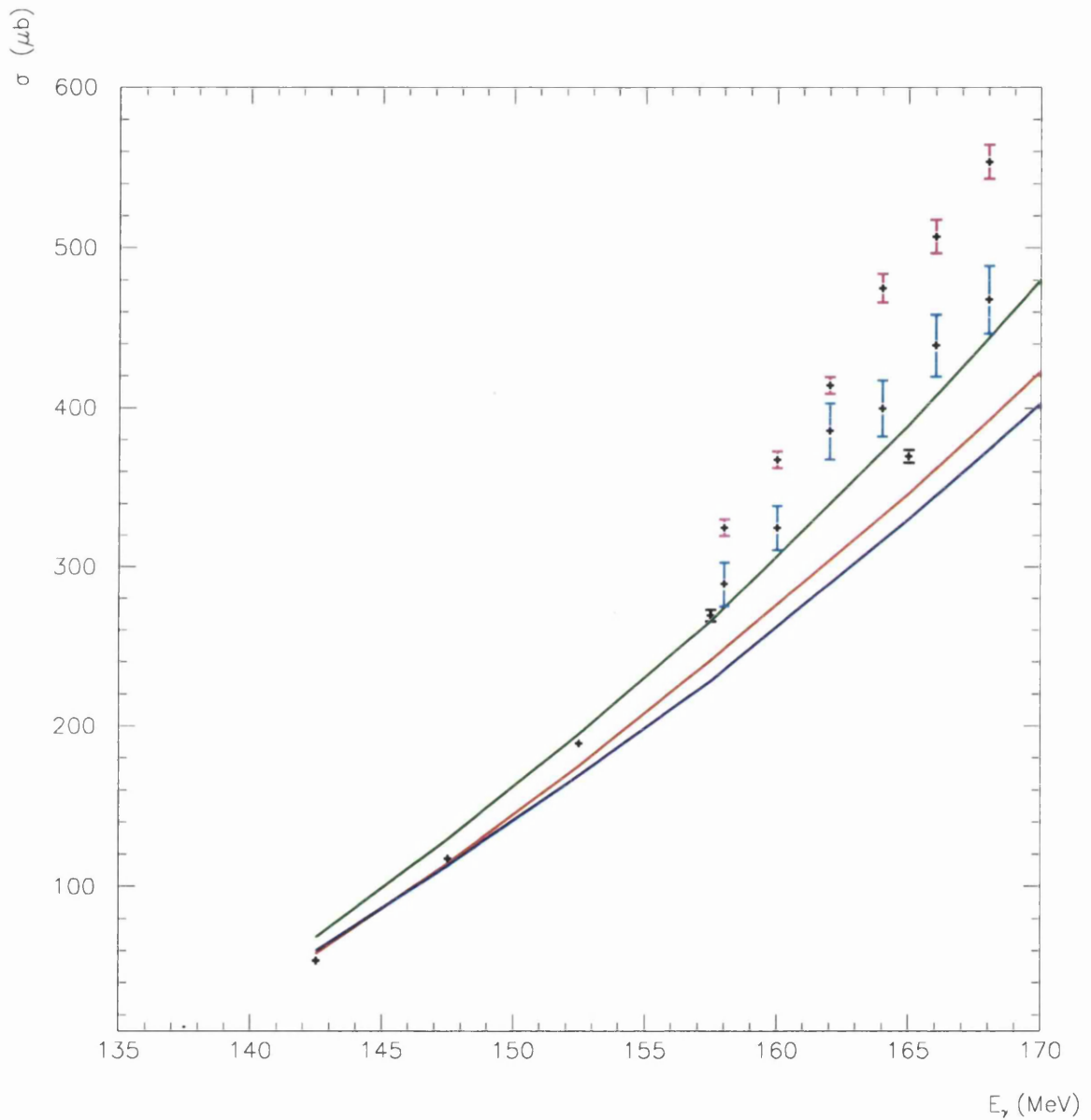


Figure 59: Integrated cross section for ^{40}Ca . Black-present experiment; light blue-coherent cross section data from [18]; purple: coherent plus non-coherent data from [18]; red-PWIA; green-DWIA; blue-DREN. All theoretical results from [23].

5.2 ^{12}C

The cross sections for ^{12}C show the same general characteristics as for ^{40}Ca . As the ^{12}C nucleus is smaller, the maxima and minima in the differential cross section occur at larger pion lab angles than for ^{40}Ca . The minima also appear less pronounced for ^{12}C .

5.2.1 Comparison with other experimental data

Figures 65 - 67 show the differential cross sections for $E_\gamma = 200, 290$ and 350 MeV from preliminary results from [20] compared with results from the present work for $E_\gamma = 200$ (obtained as described in section 5.1.1), $280 < E_\gamma < 300$ and $340 < E_\gamma < 360$ MeV. The comments made in section 5.1.1 on the comparison between the present results for ^{40}Ca and the preliminary data from [20] are also relevant for the ^{12}C data.

In the region of the first maximum, the differential cross section from the present result is greater than that from [20] for $E_\gamma = 200$ and 290 MeV and smaller for $E_\gamma = 350$ MeV. This could be partly due to the systematic variations from the separation of the coherent and non-coherent events, and partly due to the TAPS detection efficiency simulation (see section 5.1.1). At backward angles, the differential cross section from [20] is greater by a factor of up to 5. The positions of the minima agree well. As for ^{40}Ca , the full discrepancy between the data sets is too large to be explained by the systematic errors from the selection of the coherent events and statistical variations in the detection efficiency alone. Large systematic errors in the detection efficiency simulation could have caused the discrepancy, but though considerable work was done investigating the simulations [38] such errors were not found and the discrepancy remains not understood.

For ^{12}C , a second comparison with other data can be made in the Δ resonance region using the results from [19]. In that experiment, the integrated cross section was obtained for $\theta_\pi = (60 \pm 10)^\circ$ as a function of incident photon energy using a detector based on a large NaI crystal and a small array of BaF_2 crystals. Fig. 68 shows the differential cross section from the present result compared with data from [19]. The two sets of experimental data agree quite well. [19] obtained data for greater values of E_γ than was possible in the present result. There is a significant difference between the energy dependence of the

cross sections from the two measurements and the maximum of the cross section appears to be at a higher value of E_γ for the data from [19] than for the present result. Again, this may indicate systematic errors in the detection efficiency simulations which were needed for the analysis of the experiment.

Fig. 70 shows the integrated cross section for $135 < E_\gamma < 170$ MeV from the present data, compared with data from Koch et al. [17]. The data from [17] were available only for that energy range, but for more discrete values of E_γ than the present data in that energy range. The present measurement agrees quite well with the result from [17] very close to threshold but is lower at higher incident photon energies. This discrepancy is greater than the statistical errors and could be due to more non-coherent events being included in the result from [17]. As the energy resolution obtained in this result was rather poor, non-coherent events were discarded by a cut on the pion decay photon opening angle. This method reduces the coherent cross section by a factor of about 10 but is not very accurate at discarding all non-coherent events.

The ^{12}C results were used to investigate the reliability of the random background subtraction in the tagger. To do this, the differential cross section for π^0 production for the $130 < E_\gamma < 135$ MeV region, just below the π^0 production threshold, was evaluated (see fig. 72). On average, this cross section should be zero, as the incident photon energy is below the π^0 production threshold, and the average differential cross section in this region is very small; about $0.01 \mu\text{b}$. This yield is probably due to insufficient subtraction of background events in the distribution of time difference between the TAPS and the tagger (see fig. 33). The cross section below threshold is, however, negligible compared with other errors in the present result (less than $\frac{1}{10}$ of the yield in the threshold region, and only about $\frac{1}{1000}$ of the yield in the highest energy region). The cross sections for $135 < E_\gamma < 380$ MeV have not been corrected for this.

5.2.2 Comparison with theoretical models

Figures 60 - 64 and 69 show the differential and integrated cross sections for ^{12}C compared with the three theoretical models.

The comments made for the ^{40}Ca results generally apply to ^{12}C as well. Although the effect of introducing the pion-nucleus interaction into the theoretical models is somewhat smaller for ^{12}C than for ^{40}Ca , as the ^{12}C nucleus is smaller, the comparison with data clearly shows the importance of including a description of the final state interaction. The importance of including the Δ -nucleus interaction in the theoretical description is also clear as the DREN model gives a considerably better account of the ^{12}C data than the DWIA model. The maximum in the integrated cross section appears at approximately 250 MeV for ^{12}C , compared with at 225 MeV for ^{40}Ca , suggesting that the modification of the Δ mass inside the ^{12}C nucleus is about 25 MeV less than that needed to describe a Δ inside a ^{40}Ca nucleus, probably due to the smaller number of nucleons in the ^{12}C nucleus. The main discrepancies between the ^{12}C results and the theoretical models are similar to those seen for the ^{40}Ca results, i.e. the discrepancies in the positions of the minima and maxima of the differential cross sections and the energy dependence of the integrated cross section. These differences again suggest that further modification of the pion-nucleus interaction and of the Δ properties will be valuable in producing an improved description of the data for ^{12}C and ^{40}Ca obtained here and in the previous ^4He results.

5.2.3 The nuclear excitation process

Fig. 71 shows an estimate of the nuclear excitation (4.4 MeV) pion production cross section, obtained by selecting events where a 4 - 5 MeV energy deposition was detected in one of the NaI detectors. The cross section is very small: even at small pion lab angles, where it is greatest, it is only approximately $\frac{1}{10}$ of the coherent cross section at threshold and it is similar in magnitude to the sub-threshold cross section (see section 5.2.1) with so few counts that the information from the NaI detectors gives little more than an upper limit on the cross section to the 4.4 MeV excited state.

The differential cross section to an excited state is not expected to be as sharply peaked in pion lab angle as the coherent cross section. The angular distribution seen in fig. 71 for $E_\gamma < 200$ MeV contains so few data points that the structure can not be determined reliably. The distribution for $E_\gamma > 200$ MeV has structure, but it has a

maximum at about $\theta_\pi = 20^\circ$. This structure resembles the general shape of the coherent cross sections for $200 < E_\gamma < 380$ MeV. This is not understood.

In the cross section estimates in fig. 71 it was assumed that the nuclear decay photons were distributed isotropically. A calculation by Tryasuchev [43] suggests that the angular distribution of the 4.4 MeV nuclear decay photons has a minimum close to $\theta_\gamma = 90^\circ$, where θ_γ is the lab angle between the directions of the pion and the nuclear decay photon. The central angle of the NaI detectors is therefore at a minimum in the cross section, and a correction for this effect would increase the measured cross section. However, because the angular ranges covered by TAPS and the NaI are large this correction is not expected to be large.

It is possible that with further analysis of the present data, nuclear decay photons could be detected in TAPS and a better estimate of the nuclear excited state process at 4.4 MeV could be obtained. This would, however, require a significant improvement in the energy calibration of TAPS and involve a substantial amount of further work.

The differential cross section due to the nuclear excitation process is not expected to be as sharply peaked as the coherent cross section. The resemblance of the spectrum in fig. 71 to the coherent cross section strongly suggests that the events included in fig. 71 were part of the coherent yield.

This is not understood, and the results can be at best be used to indicate an upper limit on the non-coherent (4.4 MeV) process.

Table 13: Positions of the first maximum and minimum in the differential cross section for ^{12}C

E_γ (MeV)	1 st max				1 st min			
	($^\circ$) experiment	($^\circ$) PWIA	($^\circ$) DWIA	($^\circ$) DREN	($^\circ$) experiment	($^\circ$) PWIA	($^\circ$) DWIA	($^\circ$) DREN
135-140	71 ± 2	79	80	80	-	-	-	-
140-145	71 ± 2	72	73	73	-	-	-	-
145-150	65 ± 2	70	70	71	-	-	-	-
150-155	60 ± 2	66	67	67	-	-	-	-
155-160	58 ± 2	63	64	65	-	-	-	-
160-170	57 ± 2	59	59	60	-	-	-	-
170-180	53 ± 2	55	55	55	-	-	-	-
180-190	49 ± 2	52	51	51	-	-	-	-
190-200	47 ± 2	48	47	48	-	-	-	-
200-220	39 ± 2	44	43	44	122 ± 2	-	129	129
220-240	37 ± 2	40	38	39	117 ± 2	129	109	109
240-260	33 ± 2	36	34	35	92 ± 2	109	94	95
260-280	34 ± 2	33	31	32	82 ± 2	97	83	84
280-300	32 ± 2	30	28	30	77 ± 2	87	76	77
300-320	29 ± 2	28	26	28		80	71	71
320-340	24 ± 2	26	24	26	-	74	-	67
340-360	19 ± 2	24	22	24	-	68	-	61
360-380	19 ± 2	23	22	23	-	66	-	58

Table 14: Positions of the second maximum and minimum in the differential cross section for ^{12}C

E_γ (MeV)	2^{nd} max				2^{nd} min			
	($^\circ$) experiment	($^\circ$) PWIA	($^\circ$) DWIA	($^\circ$) DREN	($^\circ$) experiment	($^\circ$) PWIA	($^\circ$) DWIA	($^\circ$) DREN
135-140	-	-	-	-	-	-	-	-
140-145	-	-	-	-	-	-	-	-
145-150	-	-	-	-	-	-	-	-
150-155	-	-	-	-	-	-	-	-
155-160	-	-	-	-	-	-	-	-
160-170	-	-	-	-	-	-	-	-
170-180	-	-	-	-	-	-	-	-
180-190	-	-	-	-	-	-	-	-
190-200	-	-	-	-	-	-	-	-
200-220	128 ± 2		146	146	-	-	-	-
220-240	138 ± 2	144	135	135	-	-	-	-
240-260	104 ± 2	131	117	118	-	-	-	-
260-280	92 ± 2	119	102	104	-	-	-	-
280-300	89 ± 2	107	91	94	-	-	132	135
300-320	-	98	79	83	-	-	111	116
320-340	-	91	-	76	-	-	101	105
340-360	-	85	-	72	-	-	-	102
360-380	-	82	-	70	-	-	-	-

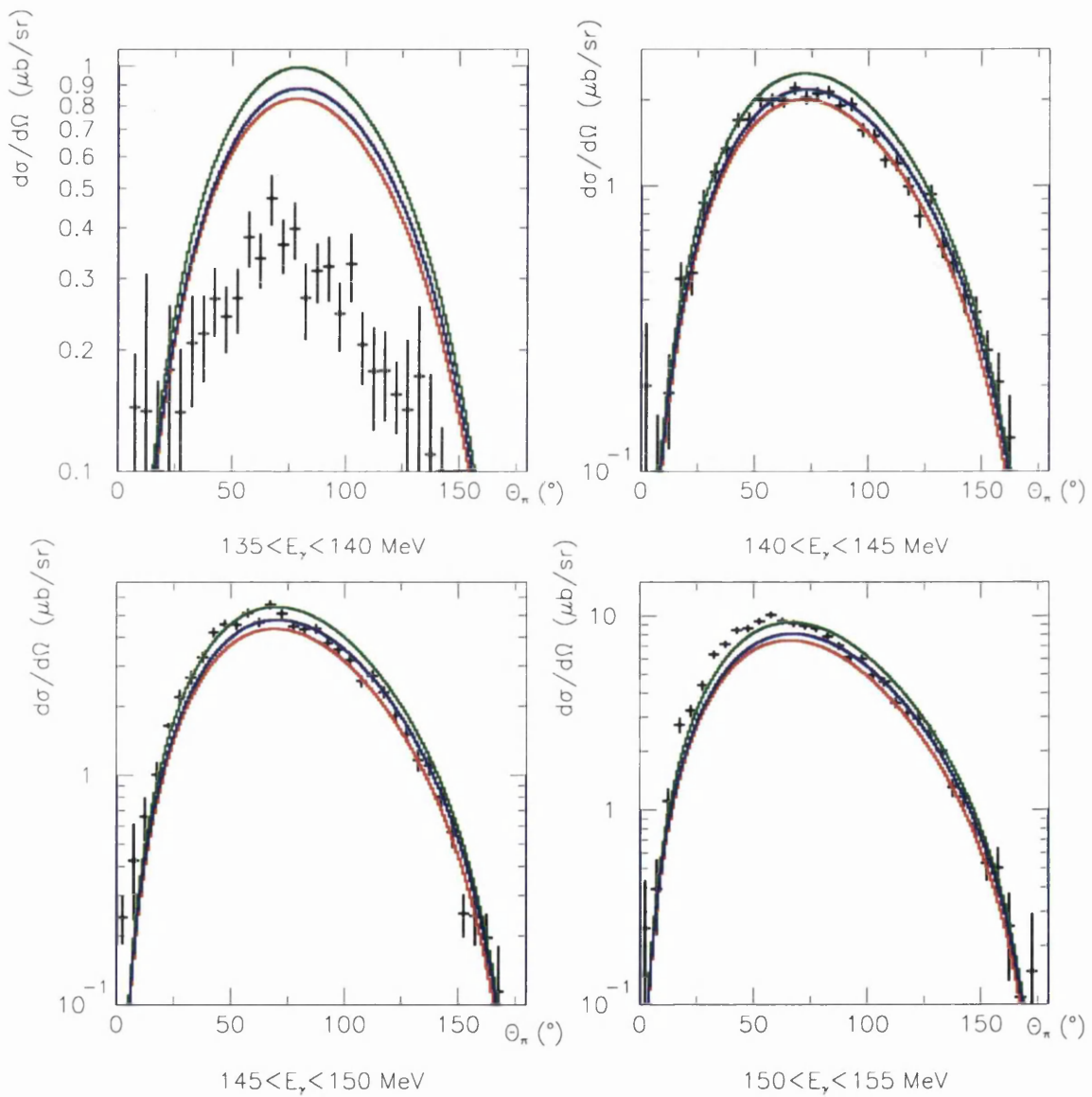


Figure 60: Differential cross sections for ^{12}C . Black-present experiment; red-PWIA; green-DWIA; blue-DREN. The theoretical predictions shown with the data where $E_\gamma < 140$ MeV is for $E_\gamma = 140$ MeV. All theoretical results from [23].

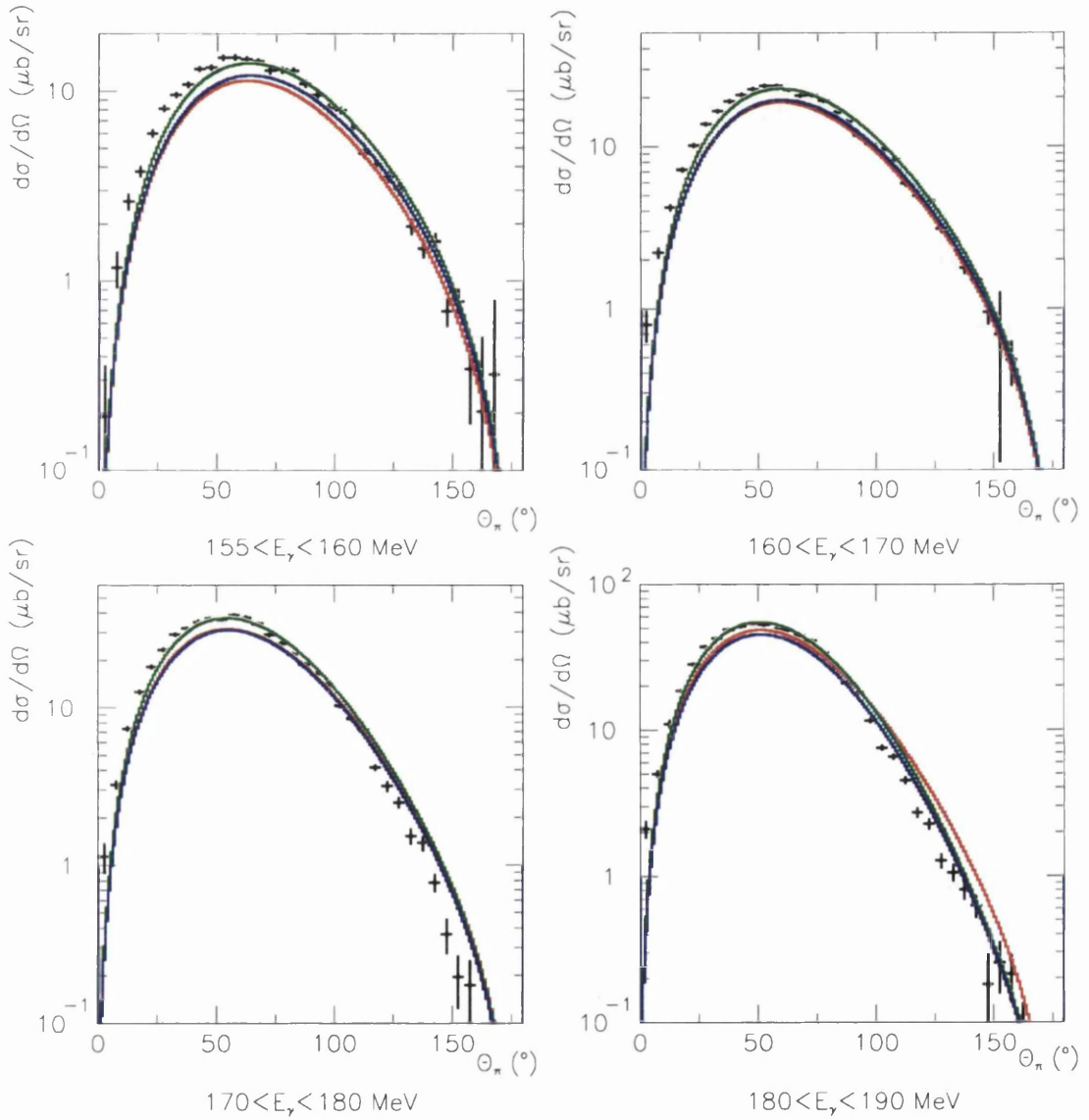


Figure 61: Differential cross sections for ^{12}C . Black-present experiment; red-PWIA; green-DWIA; blue-DREN. All theoretical results from [23].

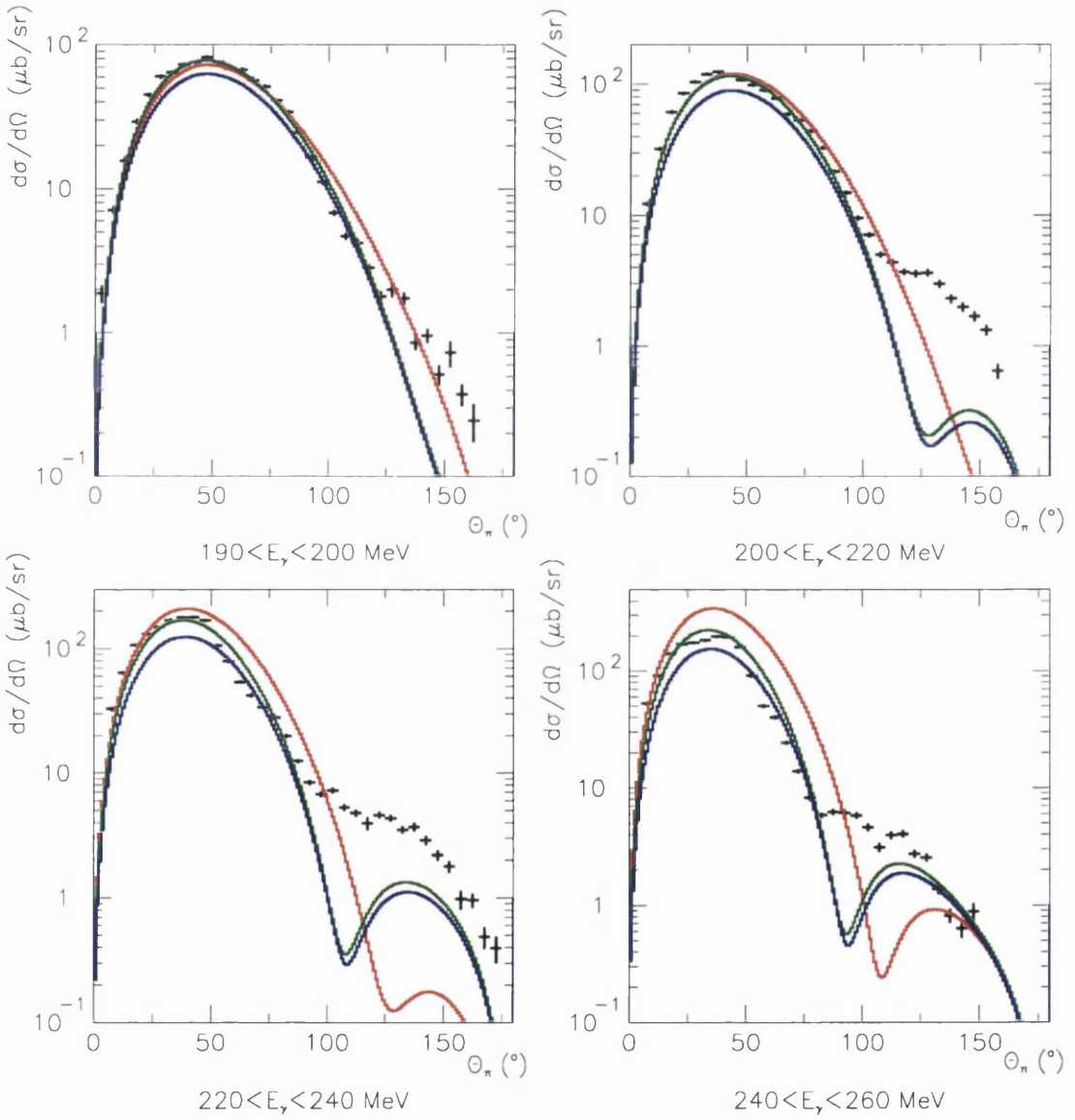


Figure 62: Differential cross sections for ^{12}C . Black-present experiment; red-PWIA, green-DWIA; blue-DREN. All theoretical results from [23].

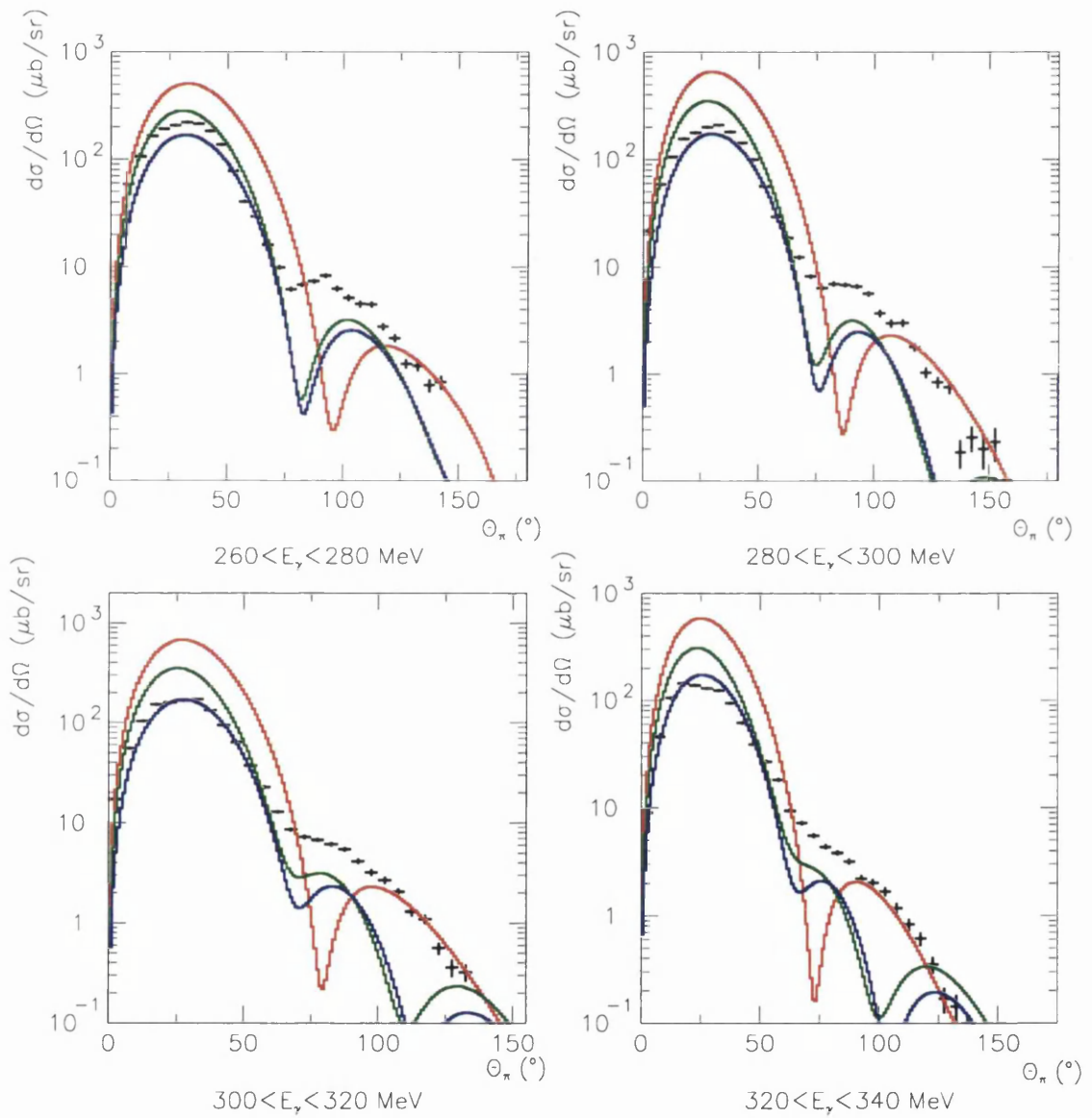


Figure 63: Differential cross sections for ^{12}C . Black-present experiment; red-PWIA; green-DWIA; blue-DREN. All theoretical results from [23].

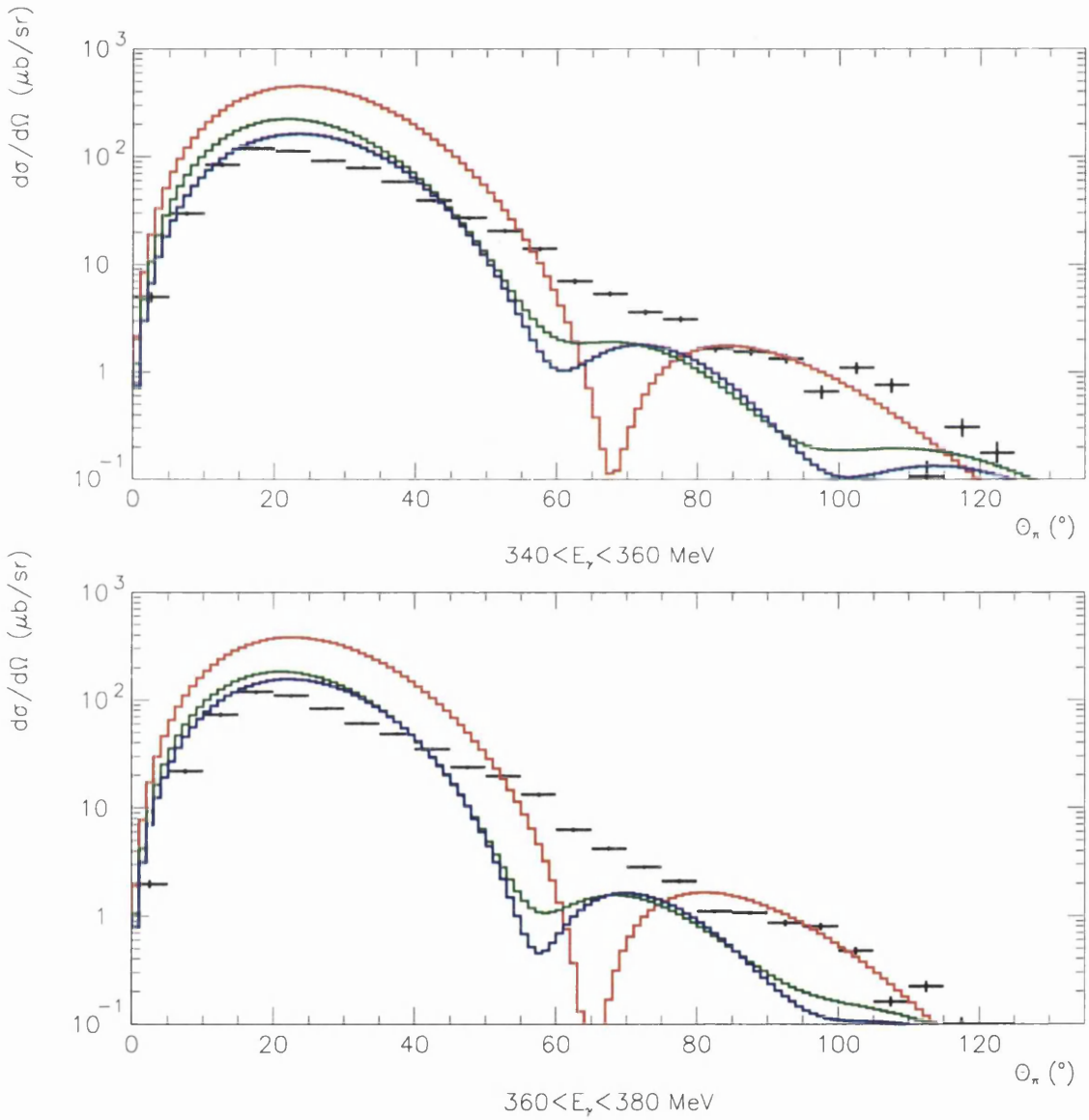


Figure 64: Differential cross sections for ^{12}C . Black-present experiment; red-PWIA; green-DWIA; blue-DREN. All theoretical results from [23].

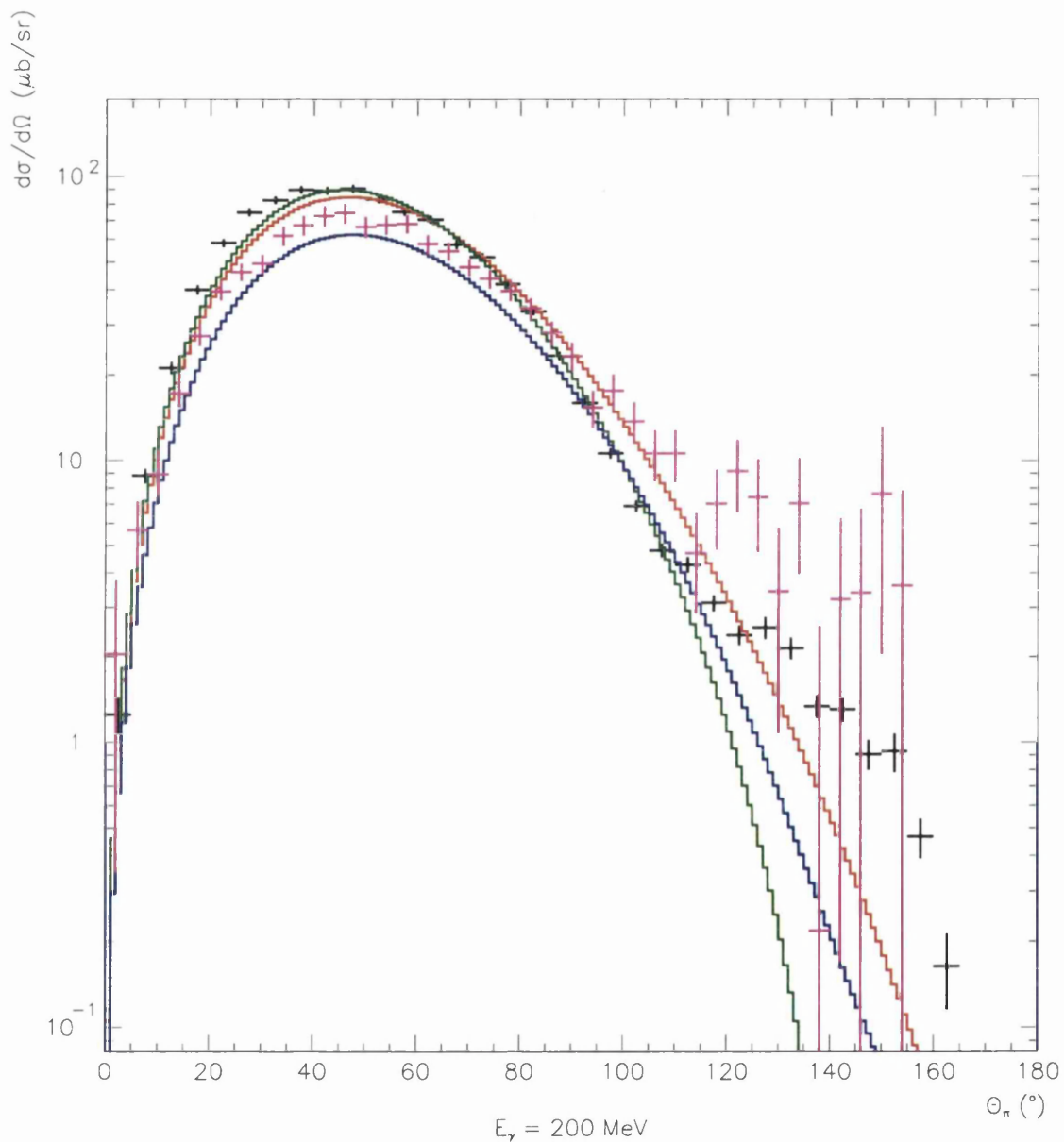


Figure 65: Differential cross section for ^{12}C at $E_\gamma = 200$ MeV. Black-present experiment; purple-data from [20]; red-PWIA; green-DWIA; blue-DREN. All theoretical results from [23].

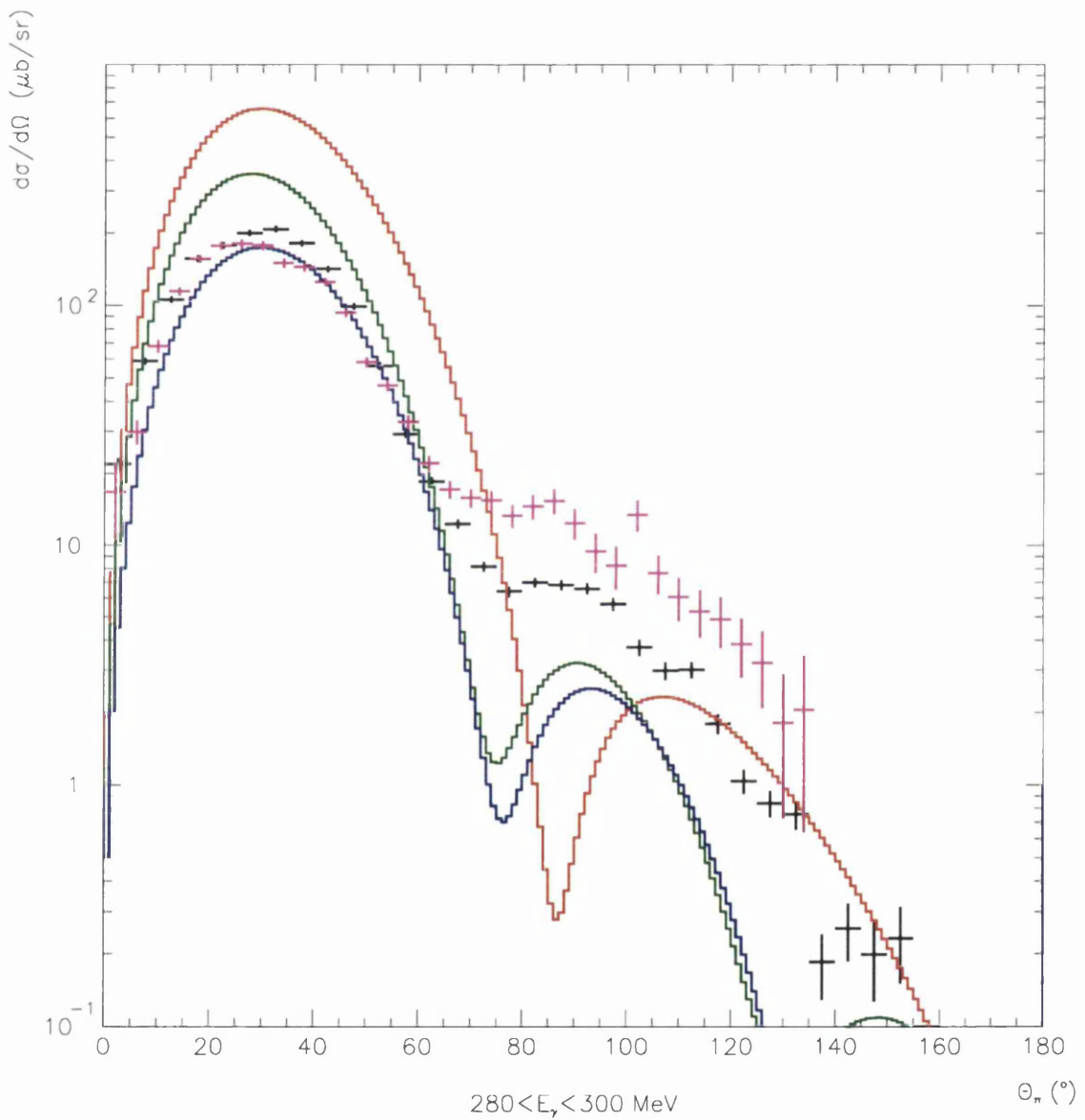


Figure 66: Differential cross section for ^{12}C at $E_\gamma = 290$ MeV. Black-present experiment; purple-data from [20]; red-PWIA; green-DWIA; blue-DREN. All theoretical results from [23].

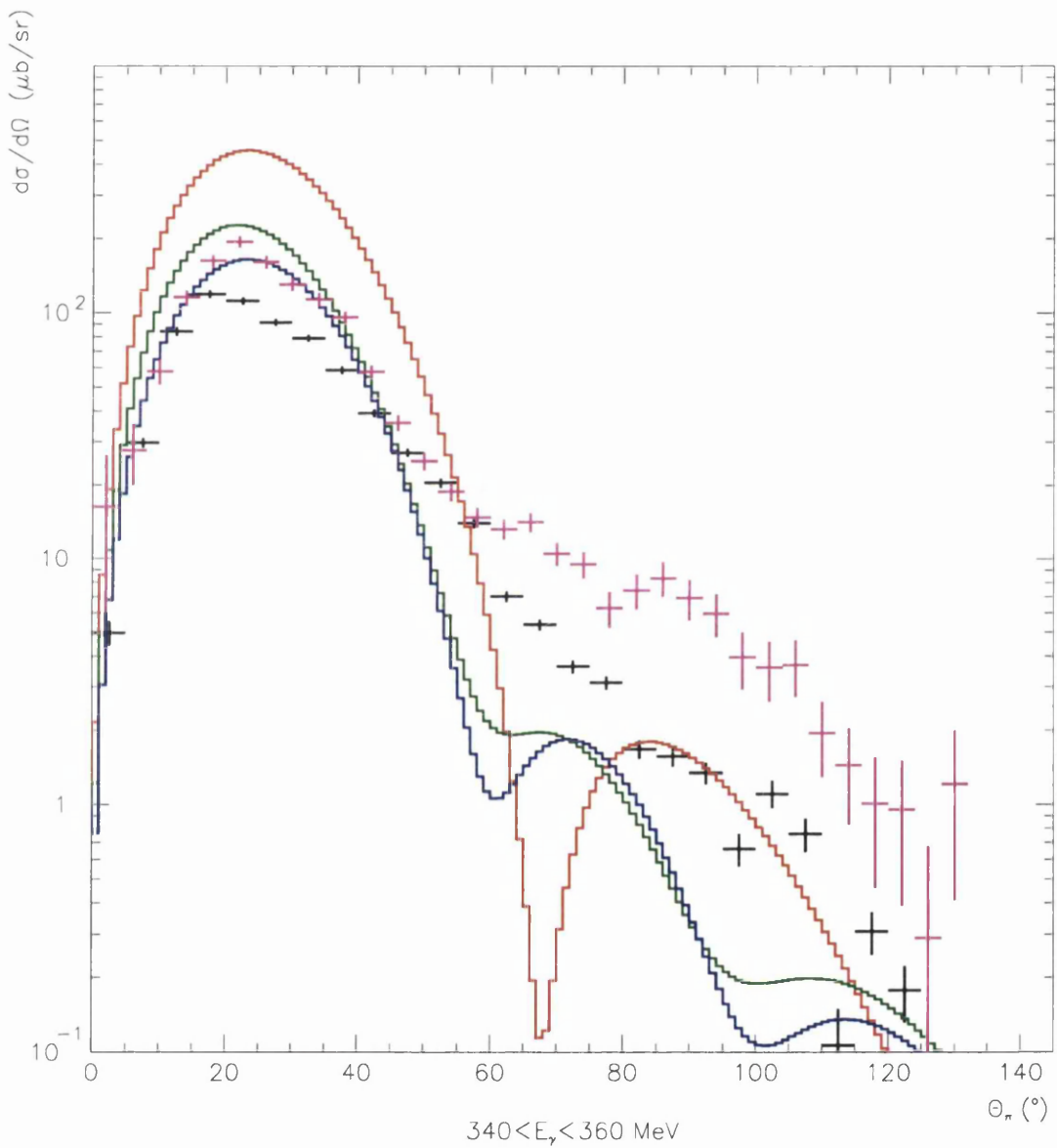


Figure 67: Differential cross section for ^{12}C at $E_\gamma = 350 \text{ MeV}$ Black-present experiment; purple-data from [20]; red-PWIA; green-DWIA; blue-DREN. All theoretical results from [23].

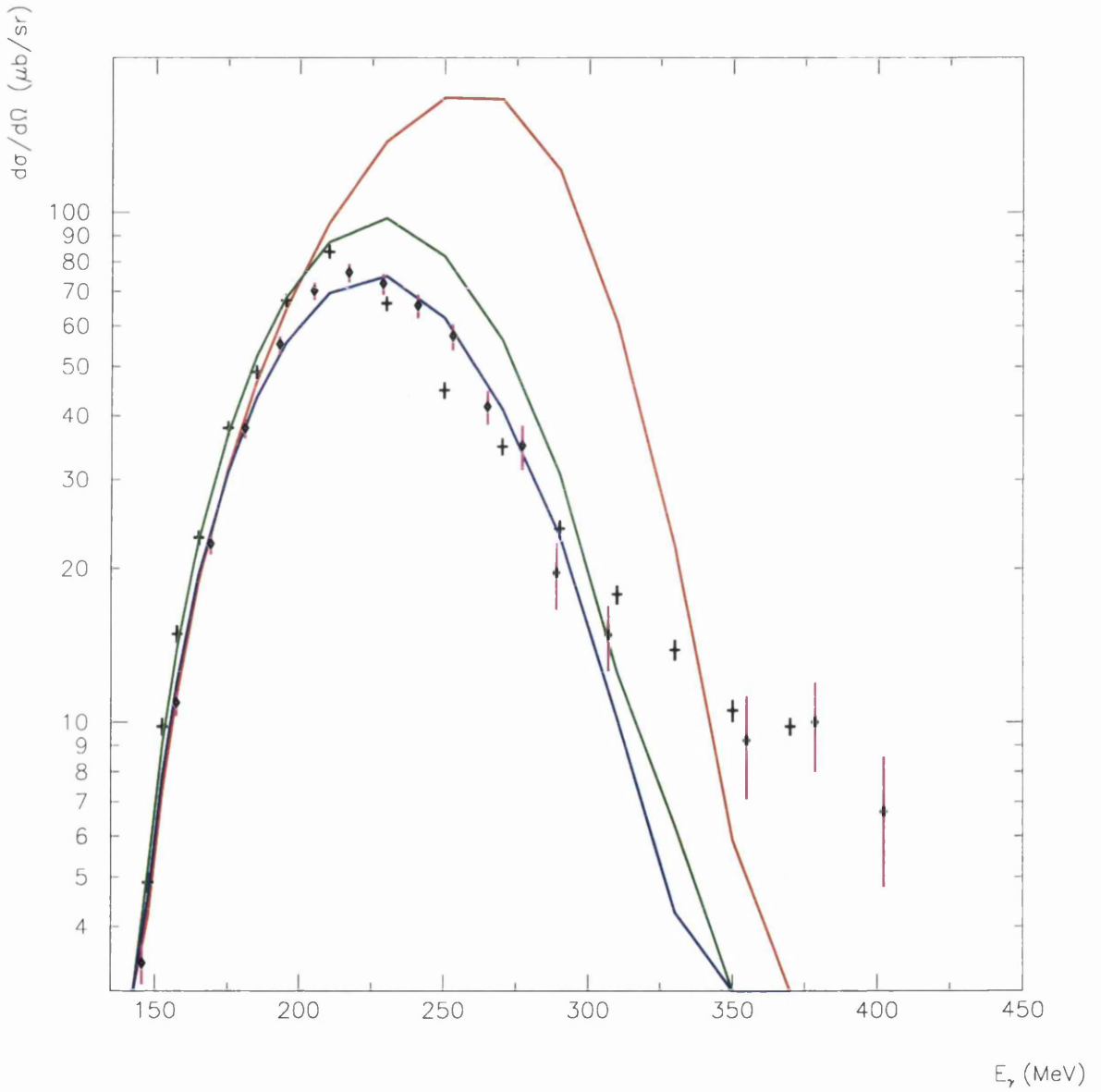


Figure 68: Differential cross section for ^{12}C at $\theta_\pi = 60^\circ$. Black crosses-present experiment; purple with black dots-data from [19] at $\theta_\pi = 60^\circ$; red-PWIA; green-DWIA;blue-DREN. All theoretical results from [23].

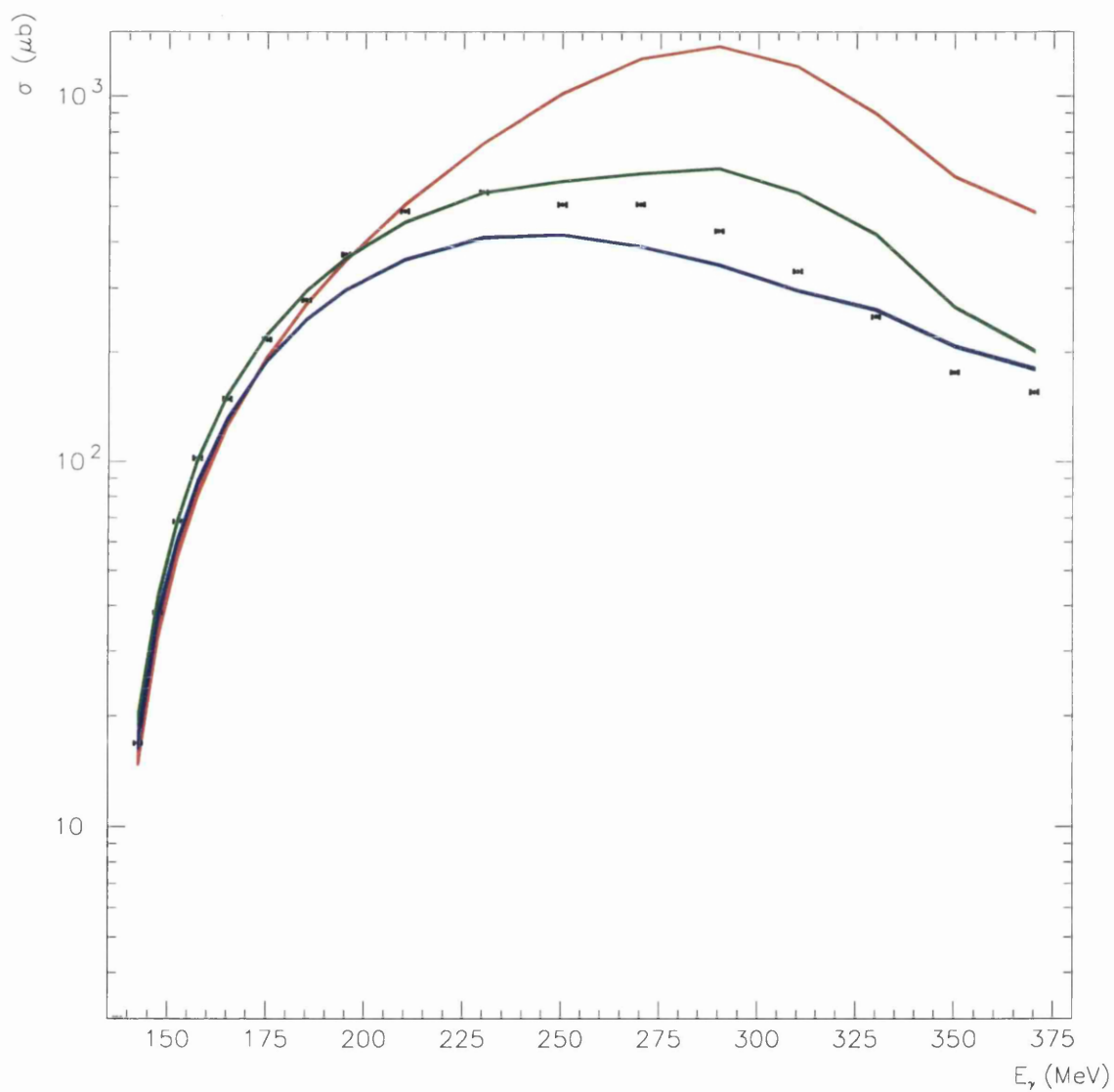


Figure 69: Integrated cross section for ^{12}C . Black-present experiment; red-PWIA; green-DWIA; blue-DREN. All theoretical results from [23].

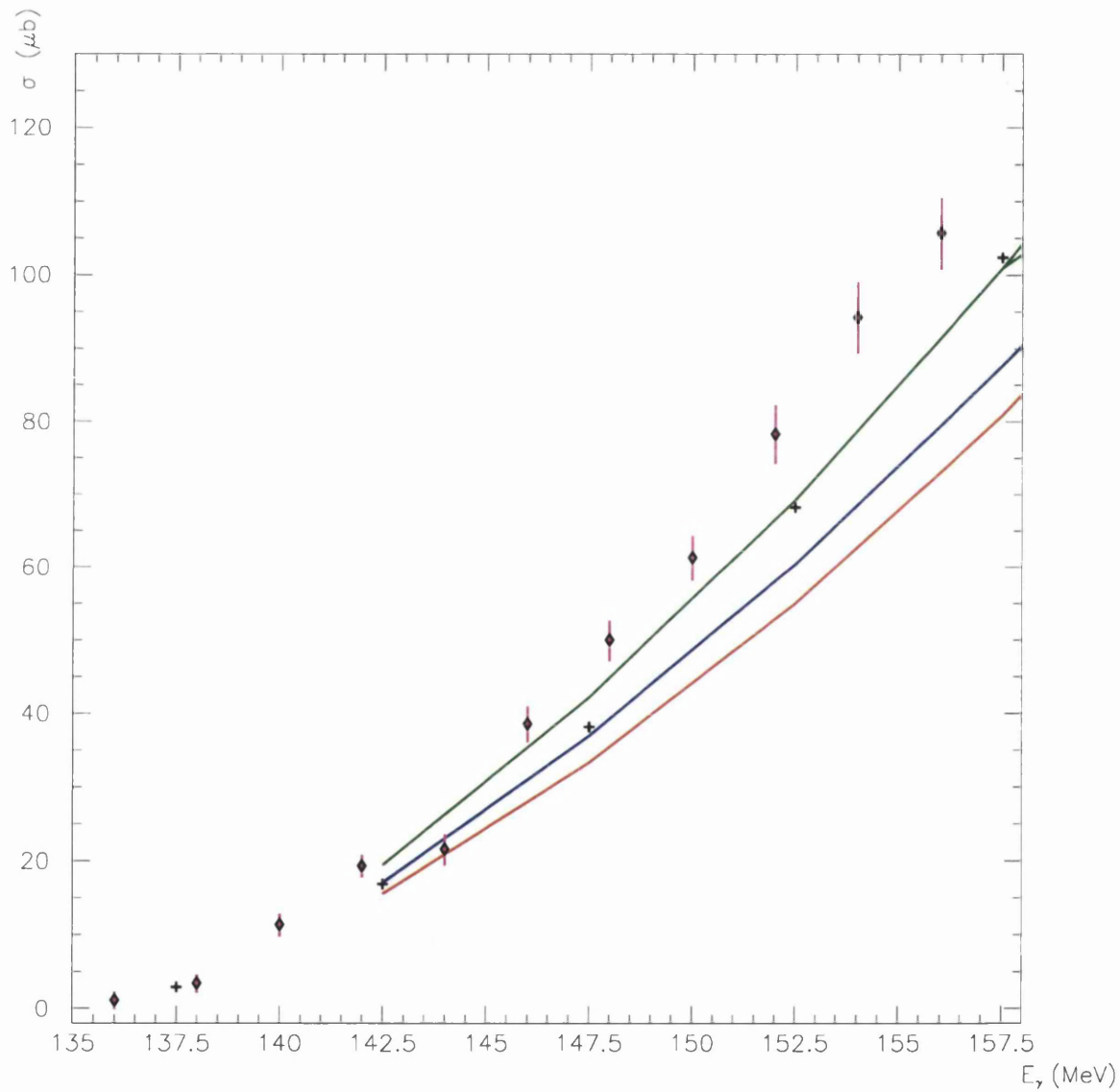


Figure 70: Integrated cross section for ^{12}C . Black-present experiment; purple-data from [17]; red-PWIA; green-DWIA; blue-DWIA with delta self energy corrections. All theoretical results from [23].

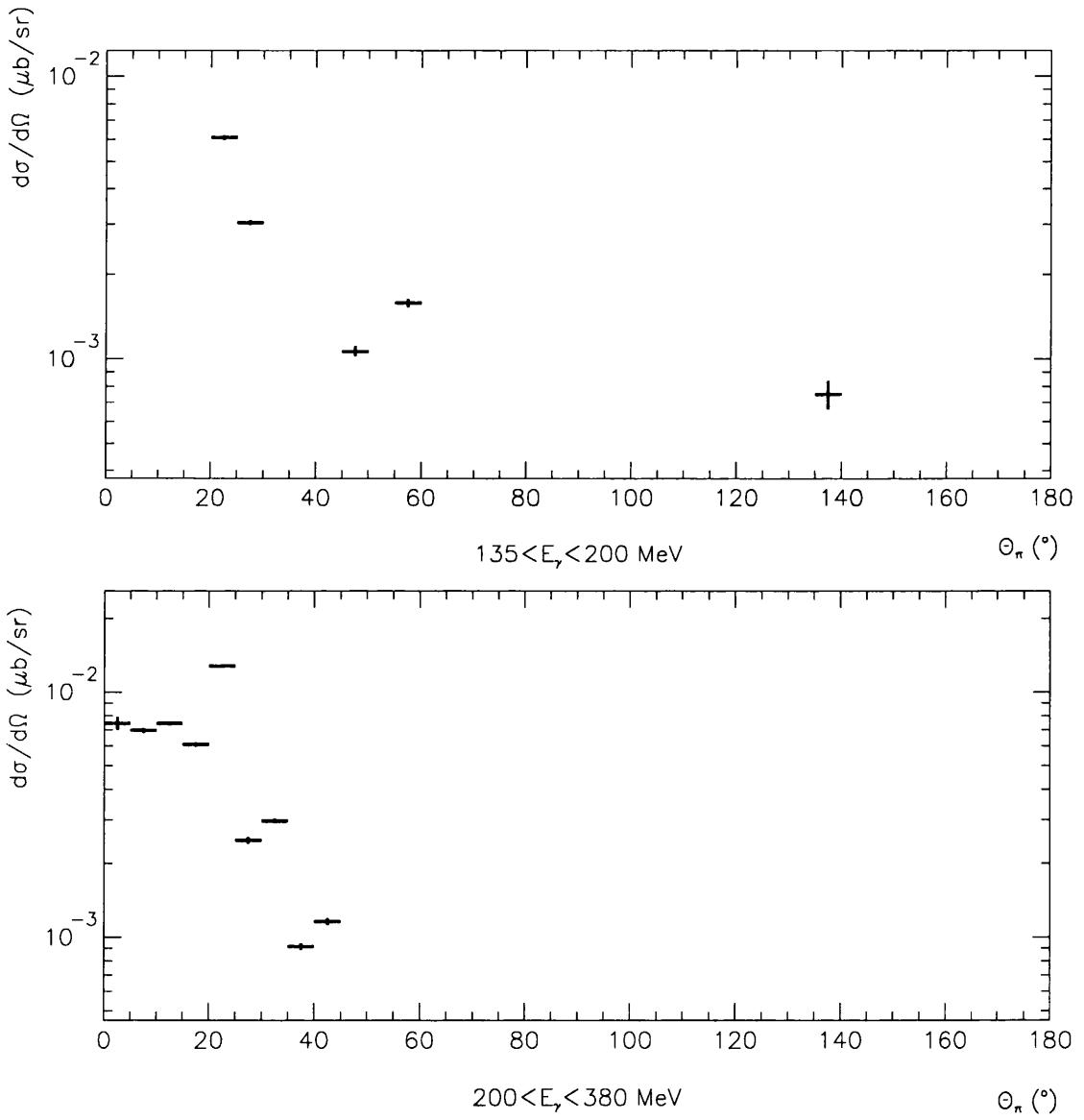


Figure 71: An estimate of the upper limit to the differential cross section for non-coherent nuclear excitation 4.4 MeV events for ^{12}C .

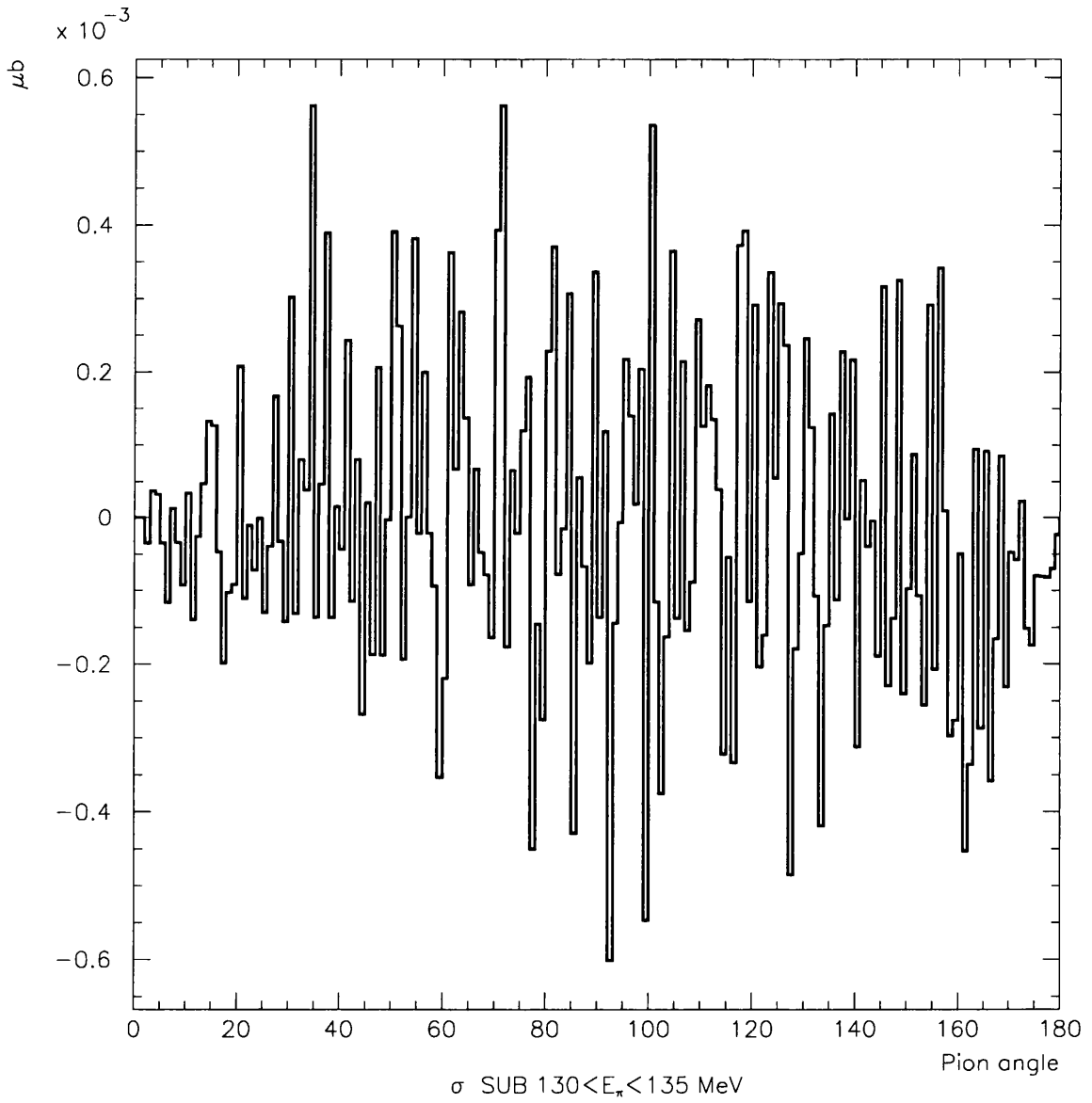


Figure 72: The differential π^0 production cross section for $130 < E_\gamma < 135$ MeV for ^{12}C .

5.3 Conclusion

Differential and integrated cross sections for coherent photo-production of neutral pions have been obtained for ^{12}C and ^{40}Ca in the incident photon energy range $135 < E_\gamma < 380$ MeV using the detector array TAPS. The present measurements cover a wider angular range and have smaller statistical errors than previous measurements. The present results are in reasonable over-all agreement with previous measurements, but there are discrepancies which exceed the statistical and the known systematic errors. These discrepancies suggest that the systematic errors in the cross sections are not properly understood.

Comparisons with the DWIA and DREN models show the importance of including a description of the final state interaction and the medium modifications in the theoretical descriptions. Comparisons with the DWIA suggest that modifications are needed in the model to describe the final state interactions accurately. The present results indicate that the properties of a free Δ particle do not provide a good description of the Δ inside a nucleus. Comparisons with the recent DREN model indicate that the parameterisation of the Δ properties and the description of multiple interactions, obtained from results on π^0 production on He, require some modification.

Results on heavier targets would provide a stronger check on both the final state interactions and on the Δ medium modifications in larger nuclei. Recent TAPS data on ^{16}O and ^{208}Pb is currently being analysed [38] and will provide more information. The results on ^{208}Pb will be particularly interesting as the ^{208}Pb nucleus contains an extra shell of neutrons compared with protons and the distributions of protons and neutrons can be compared.

Difficulties encountered in separating the coherent and non-coherent cross sections at some pion energies and angles suggest that it would be desirable to carry out further calibrations of TAPS to understand properly the cluster energy and position reconstruction. If the systematic errors in the energy and position reconstruction could be eliminated, the separation of coherent and non-coherent events in neutral pion production could be carried out with a smaller error. Furthermore, the maximum likelihood method could then be used to improve both the pion energy and position resolution.

The set-up of TAPS used in the present experiment resulted in large angular variations in pion detection efficiency. Small discrepancies between the present result and previous experimental results could be due to systematic errors in the detection efficiency simulations. A set-up with smaller angular variation in detection efficiency would provide more reliable results. The crystal ball, an array of NaI elements assembled to provide almost complete angular coverage around the target, will be assembled in Mainz in the next 12 months. This detector assembly would be well suited for pion production experiments as the angular variation of the detection efficiency would be considerably smaller than that of TAPS in the present set-up, and as the energy resolution of NaI is significantly better than that of BaF₂, making the separation between coherent and non-coherent events easier to achieve. The much improved angular coverage compared with TAPS in the present set-up would also allow for detection of nuclear decay photons over a greater angular range than was available in the present experiment.

A Tables of cross sections

Table 15: ^{12}C $\frac{d\sigma}{d\Omega}$

E_γ (MeV)	135-140	140-145	145-150	150-155	155-160	160-170
θ_π						
($^\circ$)	(μb)	(μb)	(μb)	(μb)	(μb)	(μb)
0 - 5		0.20 ± 0.13	0.24 ± 0.06	0.25 ± 0.19	0.19 ± 0.17	0.80 ± 0.18
5 - 10	0.14 ± 0.05	0.09 ± 0.07	0.42 ± 0.19	0.39 ± 0.17	1.18 ± 0.26	2.21 ± 0.18
10 - 15	0.14 ± 0.17	0.19 ± 0.07	0.66 ± 0.14	1.11 ± 0.18	2.63 ± 0.28	4.21 ± 0.22
15 - 20	0.10 ± 0.07	0.47 ± 0.07	1.00 ± 0.14	2.73 ± 0.26	3.78 ± 0.28	7.18 ± 0.30
20 - 25	0.18 ± 0.08	0.50 ± 0.08	1.64 ± 0.05	3.24 ± 0.24	6.00 ± 0.34	10.16 ± 0.39
25 - 30	0.14 ± 0.06	0.87 ± 0.10	2.20 ± 0.18	4.38 ± 0.27	8.10 ± 0.37	13.75 ± 0.48
30 - 35	0.21 ± 0.06	1.12 ± 0.09	2.67 ± 0.19	6.31 ± 0.32	9.54 ± 0.40	16.51 ± 0.56
35 - 40	0.22 ± 0.05	1.35 ± 0.09	3.28 ± 0.18	7.14 ± 0.33	10.82 ± 0.45	19.01 ± 0.65
40 - 45	0.27 ± 0.05	1.70 ± 0.10	4.20 ± 0.22	8.43 ± 0.36	13.08 ± 0.52	20.76 ± 0.71
45 - 50	0.24 ± 0.05	1.71 ± 0.10	4.57 ± 0.22	8.62 ± 0.37	13.28 ± 0.53	22.56 ± 0.77
50 - 55	0.27 ± 0.05	2.00 ± 0.11	4.54 ± 0.22	9.39 ± 0.39	14.98 ± 0.60	23.65 ± 0.80
55 - 60	0.38 ± 0.06	2.00 ± 0.11	5.11 ± 0.24	10.14 ± 0.42	15.03 ± 0.59	23.60 ± 0.80
60 - 65	0.34 ± 0.05	1.98 ± 0.11	4.66 ± 0.22	9.46 ± 0.40	14.71 ± 0.60	22.46 ± 0.76
65 - 70	0.47 ± 0.07	2.20 ± 0.12	5.57 ± 0.25	9.15 ± 0.39	14.33 ± 0.60	20.55 ± 0.72
70 - 75	0.36 ± 0.06	2.03 ± 0.11	5.09 ± 0.24	8.89 ± 0.39	12.80 ± 0.58	20.76 ± 0.73
75 - 80	0.40 ± 0.06	2.10 ± 0.11	4.47 ± 0.23	8.62 ± 0.39	12.94 ± 0.57	19.13 ± 0.67
80 - 85	0.27 ± 0.06	2.13 ± 0.11	4.34 ± 0.22	7.82 ± 0.37	12.72 ± 0.59	16.10 ± 0.60
85 - 90	0.31 ± 0.05	1.91 ± 0.11	4.36 ± 0.21	7.01 ± 0.34	10.92 ± 0.54	14.22 ± 0.54
90 - 95	0.32 ± 0.06	1.93 ± 0.10	3.77 ± 0.20	6.13 ± 0.31	9.49 ± 0.50	11.66 ± 0.48
95 -100	0.25 ± 0.05	1.57 ± 0.09	3.53 ± 0.18	5.98 ± 0.30	8.15 ± 0.46	10.38 ± 0.44
100 -105	0.33 ± 0.06	1.50 ± 0.09	3.18 ± 0.16	4.96 ± 0.26	7.93 ± 0.40	9.49 ± 0.40
105 -110	0.21 ± 0.04	1.23 ± 0.08	2.58 ± 0.16	4.57 ± 0.26	6.41 ± 0.38	8.30 ± 0.37
110 -115	0.18 ± 0.05	1.20 ± 0.08	2.71 ± 0.17	3.55 ± 0.23	4.71 ± 0.29	5.89 ± 0.29
115 -120	0.18 ± 0.04	1.00 ± 0.07	2.30 ± 0.14	3.16 ± 0.21	4.12 ± 0.30	4.97 ± 0.27
120 -125	0.16 ± 0.03	0.79 ± 0.07	1.82 ± 0.13	2.94 ± 0.22	3.53 ± 0.25	4.63 ± 0.25
125 -130	0.14 ± 0.07	0.94 ± 0.07	1.50 ± 0.12	2.53 ± 0.20	3.06 ± 0.27	3.10 ± 0.19
130 -135	0.17 ± 0.08	0.62 ± 0.06	1.16 ± 0.13	2.01 ± 0.17	1.93 ± 0.19	2.66 ± 0.20
135 -140	0.11 ± 0.06	0.54 ± 0.06	1.10 ± 0.10	1.30 ± 0.14	1.48 ± 0.16	1.78 ± 0.16
140 -145	0.08 ± 0.05	0.41 ± 0.06	0.81 ± 0.08	1.16 ± 0.14	1.62 ± 0.18	1.49 ± 0.14
145 -150	0.05 ± 0.02	0.36 ± 0.05	0.56 ± 0.08	0.85 ± 0.11	0.69 ± 0.12	0.95 ± 0.15
150 -155	0.01 ± 0.01	0.27 ± 0.04	0.25 ± 0.05	0.53 ± 0.10	0.78 ± 0.13	0.69 ± 0.58
155 -160		0.21 ± 0.05	0.24 ± 0.06	0.50 ± 0.14	0.34 ± 0.17	0.48 ± 0.15
160 -165		0.13 ± 0.05	0.20 ± 0.05	0.25 ± 0.12	0.20 ± 0.31	
165 -170			0.11 ± 0.07	0.11 ± 0.01	0.32 ± 0.48	
170 -175				0.15 ± 0.15	-0.01 ± -0.02	
175 -180						

Table 16: ^{12}C $\frac{d\sigma}{d\Omega}$

E_γ (MeV)	170-180	180-190	190-200	200-220	220-240	240-260
θ_π						
($^\circ$)	(μb)	(μb)	(μb)	(μb)	(μb)	(μb)
0 - 5	1.14 ± 0.25	2.11 ± 0.30	1.88 ± 0.28			
5 - 10	3.25 ± 0.21	5.01 ± 0.32	7.14 ± 0.49	12.23 ± 0.62	32.80 ± 1.34	52.41 ± 1.89
10 - 15	7.38 ± 0.32	11.01 ± 0.83	15.68 ± 1.08	32.28 ± 1.13	64.19 ± 2.12	91.04 ± 2.91
15 - 20	12.58 ± 0.47	18.54 ± 0.69	29.31 ± 1.49	61.24 ± 1.96	106.94 ± 3.32	139.85 ± 4.34
20 - 25	18.20 ± 0.66	28.26 ± 0.96	44.87 ± 1.62	85.27 ± 2.64	131.59 ± 4.08	170.12 ± 5.27
25 - 30	23.38 ± 0.77	37.31 ± 1.23	60.06 ± 2.16	104.06 ± 3.23	150.03 ± 4.50	175.95 ± 5.45
30 - 35	29.11 ± 0.96	42.71 ± 1.41	64.14 ± 2.12	119.20 ± 3.70	170.18 ± 5.11	183.42 ± 5.69
35 - 40	31.96 ± 1.05	49.04 ± 1.57	72.55 ± 2.39	124.00 ± 3.84	178.84 ± 5.37	198.30 ± 6.15
40 - 45	35.10 ± 1.16	51.45 ± 1.65	75.68 ± 2.42	116.16 ± 3.60	179.41 ± 5.56	195.95 ± 6.07
45 - 50	36.86 ± 1.22	54.71 ± 1.75	81.63 ± 2.61	108.00 ± 3.35	169.06 ± 5.24	160.51 ± 5.14
50 - 55	36.63 ± 1.17	52.57 ± 1.68	75.47 ± 2.41	98.70 ± 3.06	106.28 ± 3.51	91.24 ± 3.28
55 - 60	38.53 ± 1.27	48.99 ± 1.57	67.46 ± 2.09	89.79 ± 2.87	78.98 ± 2.69	49.96 ± 1.90
60 - 65	37.29 ± 1.23	48.63 ± 1.56	67.16 ± 2.15	77.83 ± 2.41	53.89 ± 1.89	40.07 ± 1.52
65 - 70	34.25 ± 1.13	44.73 ± 1.43	56.60 ± 3.11	59.14 ± 1.89	42.13 ± 1.47	24.36 ± 0.97
70 - 75	28.93 ± 0.95	41.02 ± 1.31	51.42 ± 1.65	53.30 ± 1.76	33.95 ± 1.22	13.86 ± 0.61
75 - 80	25.60 ± 0.87	33.97 ± 1.12	40.96 ± 1.31	43.95 ± 1.45	27.94 ± 1.03	8.21 ± 0.42
80 - 85	21.82 ± 0.74	26.83 ± 0.91	34.17 ± 1.13	32.60 ± 1.11	19.80 ± 0.79	5.86 ± 0.32
85 - 90	18.78 ± 0.68	20.96 ± 0.73	24.41 ± 0.83	21.51 ± 0.77	12.42 ± 0.56	6.21 ± 0.38
90 - 95	16.32 ± 0.60	18.11 ± 0.67	16.57 ± 0.65	14.90 ± 0.58	8.37 ± 0.44	6.12 ± 0.41
95 -100	13.82 ± 0.54	11.59 ± 0.53	11.17 ± 0.48	9.51 ± 0.42	6.77 ± 0.39	5.83 ± 0.41
100 -105	10.29 ± 0.42	7.52 ± 0.40	6.83 ± 0.33	7.10 ± 0.35	7.24 ± 0.42	4.62 ± 0.39
105 -110	8.47 ± 0.37	6.51 ± 0.36	4.70 ± 0.27	5.02 ± 0.28	5.31 ± 0.37	3.12 ± 0.30
110 -115	7.20 ± 0.35	4.50 ± 0.30	4.23 ± 0.29	4.39 ± 0.26	4.75 ± 0.35	3.96 ± 0.32
115 -120	4.14 ± 0.21	2.72 ± 0.24	2.83 ± 0.20	3.71 ± 0.23	3.97 ± 0.50	4.06 ± 0.30
120 -125	3.17 ± 0.26	2.27 ± 0.21	1.80 ± 0.17	3.59 ± 0.24	4.61 ± 0.31	2.74 ± 0.22
125 -130	2.49 ± 0.21	1.27 ± 0.15	2.00 ± 0.23	3.64 ± 0.24	4.36 ± 0.28	2.56 ± 0.20
130 -135	1.53 ± 0.19	1.06 ± 0.15	1.74 ± 0.18	3.00 ± 0.22	3.51 ± 0.25	1.38 ± 0.14
135 -140	1.38 ± 0.16	0.81 ± 0.13	0.86 ± 0.10	2.31 ± 0.18	3.71 ± 0.32	0.81 ± 0.11
140 -145	0.78 ± 0.11	0.63 ± 0.11	0.97 ± 0.11	1.99 ± 0.16	2.90 ± 0.26	0.63 ± 0.11
145 -150	0.37 ± 0.09	0.18 ± 0.11	0.51 ± 0.08	1.70 ± 0.16	2.21 ± 0.22	0.89 ± 0.16
150 -155	0.20 ± 0.07	0.26 ± 0.10	0.73 ± 0.15	1.33 ± 0.13	1.79 ± 0.20	
155 -160	0.17 ± 0.08	0.21 ± 0.08	0.38 ± 0.07	0.65 ± 0.09	0.98 ± 0.17	
160 -165		0.04 ± 0.09	0.25 ± 0.07		0.96 ± 0.13	
165 -170					0.49 ± 0.10	
170 -175					0.40 ± 0.10	
175 -180						

Table 17: ^{12}C $\frac{d\sigma}{d\Omega}$

E_γ (MeV)	260-280	280-300	300-320	320-340	340-360	360-380
θ_π						
($^\circ$)	(μb)	(μb)	(μb)	(μb)	(μb)	(μb)
0 - 5		21.85 ± 1.38	17.10 ± 1.15	9.03 ± 0.82	4.99 ± 0.56	1.98 ± 0.18
5 - 10	59.12 ± 2.07	58.87 ± 2.18	55.50 ± 2.22	45.85 ± 1.88	29.79 ± 1.37	21.91 ± 1.05
10 - 15	105.83 ± 3.39	106.02 ± 3.60	104.12 ± 3.64	105.10 ± 4.20	84.22 ± 3.62	73.00 ± 3.21
15 - 20	164.14 ± 5.09	156.94 ± 5.02	152.44 ± 5.18	144.23 ± 5.19	119.77 ± 4.67	118.10 ± 4.61
20 - 25	190.99 ± 5.92	178.34 ± 5.53	160.19 ± 5.29	138.08 ± 4.83	112.39 ± 4.05	109.95 ± 4.07
25 - 30	207.23 ± 6.42	200.57 ± 6.22	169.50 ± 5.42	129.74 ± 4.28	91.92 ± 3.13	83.33 ± 2.83
30 - 35	220.85 ± 6.85	208.42 ± 6.46	171.27 ± 5.48	124.27 ± 4.10	79.32 ± 2.70	60.66 ± 2.00
35 - 40	214.98 ± 6.66	181.81 ± 5.82	133.10 ± 4.39	94.38 ± 3.21	58.90 ± 2.18	48.43 ± 1.70
40 - 45	183.82 ± 5.70	142.49 ± 4.56	94.62 ± 3.22	61.82 ± 2.16	39.41 ± 1.50	34.86 ± 1.25
45 - 50	137.66 ± 4.54	99.79 ± 3.39	63.88 ± 2.30	39.00 ± 1.48	27.22 ± 1.12	23.84 ± 0.88
50 - 55	77.72 ± 2.80	56.53 ± 2.15	37.54 ± 1.50	26.92 ± 1.08	20.57 ± 0.93	19.64 ± 0.75
55 - 60	40.41 ± 1.54	29.38 ± 1.18	22.63 ± 0.95	18.24 ± 0.82	14.04 ± 0.67	13.31 ± 0.52
60 - 65	29.38 ± 1.20	18.64 ± 0.78	12.89 ± 0.58	9.42 ± 0.46	7.02 ± 0.39	6.31 ± 0.26
65 - 70	16.04 ± 0.71	12.35 ± 0.57	8.60 ± 0.42	7.23 ± 0.36	5.36 ± 0.30	4.21 ± 0.17
70 - 75	9.89 ± 0.49	8.17 ± 0.41	7.19 ± 0.35	5.55 ± 0.29	3.62 ± 0.22	2.85 ± 0.12
75 - 80	6.19 ± 0.34	6.40 ± 0.33	6.75 ± 0.34	4.38 ± 0.25	3.12 ± 0.20	2.12 ± 0.09
80 - 85	6.83 ± 0.37	6.98 ± 0.36	6.11 ± 0.32	3.83 ± 0.23	1.67 ± 0.14	1.11 ± 0.05
85 - 90	7.33 ± 0.39	6.83 ± 0.36	5.43 ± 0.30	3.18 ± 0.20	1.57 ± 0.14	1.08 ± 0.06
90 - 95	8.25 ± 0.44	6.58 ± 0.36	4.15 ± 0.27	2.21 ± 0.18	1.34 ± 0.13	0.87 ± 0.06
95 - 100	6.25 ± 0.42	5.66 ± 0.36	3.20 ± 0.25	2.02 ± 0.18	0.66 ± 0.10	0.80 ± 0.07
100 - 105	5.15 ± 0.38	3.73 ± 0.30	2.68 ± 0.23	1.68 ± 0.18	1.11 ± 0.14	0.48 ± 0.04
105 - 110	4.50 ± 0.36	2.99 ± 0.27	2.04 ± 0.20	1.18 ± 0.15	0.76 ± 0.12	0.16 ± 0.02
110 - 115	4.47 ± 0.31	3.01 ± 0.24	1.31 ± 0.14	0.83 ± 0.11	0.11 ± 0.04	0.22 ± 0.03
115 - 120	2.77 ± 0.22	1.80 ± 0.17	1.10 ± 0.12	0.61 ± 0.09	0.31 ± 0.06	0.10 ± 0.01
120 - 125	2.16 ± 0.19	1.04 ± 0.12	0.56 ± 0.08	0.35 ± 0.06	0.18 ± 0.05	0.02 ± 0.00
125 - 130	1.25 ± 0.13	0.84 ± 0.11	0.36 ± 0.07	0.17 ± 0.05		
130 - 135	1.20 ± 0.13	0.76 ± 0.11	0.32 ± 0.06	0.14 ± 0.04		
135 - 140	0.79 ± 0.11	0.19 ± 0.06		0.09 ± 0.04		
140 - 145	0.84 ± 0.13	0.26 ± 0.07				
145 - 150		0.20 ± 0.07				
150 - 155		0.23 ± 0.08				
155 - 160		0.06 ± 0.04				
160 - 165						
165 - 170						
170 - 175						
175 - 180						

Table 18: ^{40}Ca $\frac{d\sigma}{d\Omega}$

E_γ (MeV)	135-140	140-145	145-150	150-155	155-160	160-170
θ_π						
($^\circ$)	(μb)	(μb)	(μb)	(μb)	(μb)	(μb)
0 - 5			1.11 \pm 0.59	2.26 \pm 1.09	2.78 \pm 1.47	5.47 \pm 1.17
5 - 10	-0.09 \pm -0.14	0.85 \pm 0.53	2.40 \pm 0.87	3.74 \pm 0.83	9.01 \pm 1.38	16.32 \pm 1.16
10 - 15	0.08 \pm 0.07	2.07 \pm 0.99	4.34 \pm 0.76	11.97 \pm 1.39	18.24 \pm 1.50	34.20 \pm 1.61
15 - 20	0.30 \pm 0.31	1.97 \pm 0.86	7.60 \pm 1.10	18.38 \pm 1.36	30.22 \pm 1.75	61.99 \pm 2.36
20 - 25	0.87 \pm 0.55	4.09 \pm 1.31	11.49 \pm 1.02	26.11 \pm 1.67	41.98 \pm 2.01	86.19 \pm 3.10
25 - 30	1.14 \pm 0.32	5.05 \pm 1.46	15.18 \pm 1.26	32.25 \pm 1.64	55.16 \pm 2.37	101.93 \pm 3.57
30 - 35	0.83 \pm 0.23	6.71 \pm 1.75	19.69 \pm 1.24	36.96 \pm 1.70	60.83 \pm 2.43	109.70 \pm 3.62
35 - 40	1.10 \pm 0.23	7.21 \pm 1.82	21.25 \pm 1.53	42.24 \pm 1.86	70.56 \pm 2.75	114.56 \pm 3.90
40 - 45	1.59 \pm 0.35	8.37 \pm 2.05	22.37 \pm 1.36	38.56 \pm 1.70	65.67 \pm 2.63	89.18 \pm 3.12
45 - 50	1.55 \pm 0.26	8.39 \pm 1.93	23.80 \pm 1.29	42.67 \pm 1.83	62.85 \pm 2.58	102.83 \pm 3.70
50 - 55	2.11 \pm 0.26	8.54 \pm 1.89	21.94 \pm 1.08	40.47 \pm 1.74	62.47 \pm 2.56	66.93 \pm 2.61
55 - 60	1.22 \pm 0.25	8.31 \pm 1.89	20.58 \pm 1.11	34.51 \pm 1.55	58.50 \pm 2.46	76.20 \pm 3.12
60 - 65	1.87 \pm 0.25	8.60 \pm 1.94	19.33 \pm 1.60	33.91 \pm 1.53	45.41 \pm 2.09	58.29 \pm 2.22
65 - 70	2.11 \pm 0.30	7.87 \pm 1.79	18.67 \pm 0.99	27.44 \pm 1.37	33.41 \pm 1.77	41.41 \pm 1.78
70 - 75	1.62 \pm 0.22	7.72 \pm 1.79	15.81 \pm 0.92	21.00 \pm 1.20	28.69 \pm 1.66	31.90 \pm 1.47
75 - 80	1.65 \pm 0.25	6.79 \pm 1.64	13.58 \pm 1.06	19.48 \pm 1.19	22.67 \pm 1.50	22.38 \pm 1.16
80 - 85	1.42 \pm 0.23	5.40 \pm 1.40	11.29 \pm 0.79	14.95 \pm 1.05	18.11 \pm 1.36	16.31 \pm 1.03
85 - 90	1.34 \pm 0.25	5.62 \pm 1.43	8.31 \pm 0.61	9.86 \pm 0.86	9.65 \pm 1.09	5.32 \pm 0.79
90 - 95	1.26 \pm 0.28	4.66 \pm 1.22	6.00 \pm 0.49	8.66 \pm 0.78	8.08 \pm 1.41	3.66 \pm 0.76
95 -100	1.07 \pm 0.22	3.52 \pm 1.00	5.36 \pm 0.53	5.60 \pm 0.69	5.01 \pm 1.10	2.31 \pm 0.58
100 -105	0.91 \pm 0.23	2.78 \pm 0.82	4.32 \pm 0.42	4.81 \pm 0.68	4.12 \pm 0.90	1.92 \pm 0.55
105 -110	0.85 \pm 0.22	2.47 \pm 0.79	3.61 \pm 0.43	3.45 \pm 0.56	3.28 \pm 2.24	1.28 \pm 0.75
110 -115	0.54 \pm 0.20	2.24 \pm 0.74	2.00 \pm 0.34	3.22 \pm 0.67	1.69 \pm 0.55	0.79 \pm 0.78
115 -120	0.65 \pm 0.17	1.71 \pm 0.62	1.94 \pm 0.38	2.77 \pm 0.65		1.36 \pm 0.57
120 -125	0.80 \pm 0.37	1.30 \pm 0.51	1.58 \pm 0.32			1.38 \pm 0.52
125 -130	0.31 \pm 0.17	0.71 \pm 0.37	0.95 \pm 0.28			1.97 \pm 0.52
130 -135	0.40 \pm 0.16	0.63 \pm 0.31	0.64 \pm 0.63			2.50 \pm 0.59
135 -140		0.33 \pm 0.36	0.47 \pm 0.32			2.17 \pm 0.55
140 -145		0.58 \pm 0.32	0.26 \pm 0.77			2.54 \pm 0.53
145 -150		0.43 \pm 0.31	0.21 \pm 0.26			2.11 \pm 0.52
150 -155		0.37 \pm 0.28	0.34 \pm 0.26			0.84 \pm 0.47
155 -160		0.15 \pm 0.14				0.30 \pm 0.54
160 -165						0.41 \pm 0.61
165 -170						
170 -175						
175 -180						

Table 19: ^{40}Ca $\frac{d\sigma}{d\Omega}$

E_γ (MeV)	170-180	180-190	190-200	200-220	220-240	240-260
θ_π ($^\circ$)	(μb)	(μb)	(μb)	(μb)	(μb)	(μb)
0 - 5	12.60 \pm 1.58	7.83 \pm 1.39	14.02 \pm 2.00	26.33 \pm 2.82	63.96 \pm 8.06	112.97 \pm 8.02
5 - 10	28.06 \pm 1.71	50.30 \pm 2.41	57.68 \pm 3.00	102.33 \pm 5.32	260.68 \pm 10.69	314.83 \pm 11.33
10 - 15	61.51 \pm 1.85	93.48 \pm 3.46	138.71 \pm 5.13	257.42 \pm 8.75	460.43 \pm 27.63	537.47 \pm 17.20
15 - 20	100.51 \pm 3.52	151.85 \pm 5.16	227.31 \pm 7.73	406.65 \pm 12.61	601.91 \pm 43.34	678.70 \pm 23.75
20 - 25	128.65 \pm 9.91	219.16 \pm 7.01	317.50 \pm 10.48	505.23 \pm 15.66	589.63 \pm 65.45	667.08 \pm 22.01
25 - 30	156.09 \pm 4.99	255.15 \pm 8.16	366.33 \pm 13.19	515.70 \pm 15.99	504.26 \pm 15.63	550.85 \pm 19.83
30 - 35	163.83 \pm 5.24	252.27 \pm 8.07	341.19 \pm 11.60	474.08 \pm 14.70	395.32 \pm 12.26	380.82 \pm 12.19
35 - 40	165.30 \pm 5.29	244.13 \pm 7.81	312.24 \pm 10.30	388.27 \pm 12.04	285.85 \pm 9.15	243.31 \pm 8.03
40 - 45	159.77 \pm 5.27	224.25 \pm 7.40	257.16 \pm 8.49	264.92 \pm 8.21	177.78 \pm 6.22	125.31 \pm 4.76
45 - 50	139.81 \pm 4.61	188.63 \pm 6.22	208.78 \pm 6.89	130.52 \pm 4.57	81.68 \pm 3.68	57.11 \pm 2.97
50 - 55	113.01 \pm 3.84	144.46 \pm 4.91	143.09 \pm 4.58	71.76 \pm 2.87	30.19 \pm 2.20	29.74 \pm 2.08
55 - 60	88.99 \pm 3.11	100.36 \pm 3.51	74.50 \pm 3.20	40.44 \pm 1.86	12.51 \pm 1.33	29.98 \pm 2.25
60 - 65	70.86 \pm 2.55	72.23 \pm 2.96	47.58 \pm 2.38	18.29 \pm 1.06	12.65 \pm 1.21	38.38 \pm 2.46
65 - 70	50.52 \pm 1.97	52.62 \pm 2.37	28.78 \pm 1.70	17.29 \pm 1.09	18.17 \pm 1.42	36.51 \pm 2.19
70 - 75	33.62 \pm 1.48	26.05 \pm 1.49	15.86 \pm 1.22	19.18 \pm 1.11	18.22 \pm 1.26	27.34 \pm 1.72
75 - 80	20.37 \pm 1.10	14.77 \pm 1.20	13.78 \pm 1.17	26.17 \pm 1.41	19.93 \pm 1.32	15.16 \pm 1.15
80 - 85	12.60 \pm 1.03	8.17 \pm 0.83	15.26 \pm 1.24	29.55 \pm 1.57	18.66 \pm 1.31	12.10 \pm 0.97
85 - 90	6.26 \pm 0.82	9.08 \pm 0.90	14.43 \pm 1.13	25.72 \pm 1.36	13.40 \pm 1.13	9.80 \pm 0.98
90 - 95	5.08 \pm 0.76	10.63 \pm 0.97	20.37 \pm 1.45	23.66 \pm 1.30	7.42 \pm 0.88	5.15 \pm 0.80
95 -100	3.79 \pm 0.68	11.21 \pm 0.94	15.02 \pm 1.19	18.80 \pm 1.13	2.96 \pm 0.62	4.41 \pm 0.90
100 -105	5.27 \pm 0.80	11.61 \pm 1.03	13.06 \pm 1.14	15.46 \pm 0.99	4.77 \pm 0.69	6.18 \pm 0.90
105 -110	7.14 \pm 0.86	14.07 \pm 1.10	12.10 \pm 1.09	9.91 \pm 0.83	3.41 \pm 0.65	5.39 \pm 1.01
110 -115	8.78 \pm 0.93	11.50 \pm 1.02	13.80 \pm 1.16	6.02 \pm 0.63	2.97 \pm 0.97	4.12 \pm 0.83
115 -120	9.63 \pm 0.92	13.25 \pm 1.10	10.11 \pm 1.01	3.19 \pm 0.46	1.83 \pm 0.45	6.91 \pm 0.84
120 -125	10.08 \pm 1.03	9.01 \pm 0.89	8.39 \pm 0.94	2.10 \pm 0.44	3.03 \pm 0.55	3.28 \pm 0.51
125 -130	6.83 \pm 0.73	7.23 \pm 0.82	4.69 \pm 0.74	2.47 \pm 0.41	2.75 \pm 0.55	2.17 \pm 0.43
130 -135	7.59 \pm 0.77	5.75 \pm 0.73	3.47 \pm 0.63	2.60 \pm 0.40	1.04 \pm 0.50	
135 -140	7.42 \pm 0.96	5.25 \pm 0.68	2.06 \pm 0.62		2.82 \pm 0.59	
140 -145	4.47 \pm 0.64	2.05 \pm 0.44			1.25 \pm 0.40	
145 -150	3.11 \pm 0.50	1.12 \pm 0.33			1.72 \pm 0.42	
150 -155	1.95 \pm 0.39	2.07 \pm 0.41				
155 -160	1.05 \pm 0.43	0.74 \pm 0.25				
160 -165		0.58 \pm 0.28				
165 -170						
170 -175						
175 -180						

Table 20: ^{40}Ca $\frac{d\sigma}{d\Omega}$

E_γ (MeV)	260-280	280-300	300-320	320-340	340-360	360-380
θ_π ($^\circ$)	(μb)	(μb)	(μb)	(μb)	(μb)	(μb)
0 - 5	137.86 \pm 9.51	127.65 \pm 8.04	107.35 \pm 6.76	66.45 \pm 5.18	32.62 \pm 3.59	12.46 \pm 2.20
5 - 10	311.20 \pm 11.51	355.76 \pm 13.16	339.85 \pm 13.25	278.10 \pm 12.24	170.28 \pm 8.00	126.82 \pm 6.85
10 - 15	553.73 \pm 19.93	546.52 \pm 18.58	513.98 \pm 18.50	486.88 \pm 19.48	373.38 \pm 15.68	318.57 \pm 14.02
15 - 20	731.94 \pm 23.42	622.80 \pm 19.93	552.14 \pm 19.32	476.35 \pm 17.62	365.44 \pm 14.98	313.95 \pm 13.50
20 - 25	643.95 \pm 19.96	491.07 \pm 15.71	369.71 \pm 12.20	269.11 \pm 9.42	181.38 \pm 7.07	146.70 \pm 6.01
25 - 30	486.77 \pm 15.09	347.93 \pm 11.13	221.80 \pm 7.32	121.20 \pm 4.36	70.13 \pm 2.81	50.43 \pm 2.32
30 - 35	300.29 \pm 9.61	191.41 \pm 6.51	104.34 \pm 3.76	56.22 \pm 2.30	31.97 \pm 1.47	25.58 \pm 1.38
35 - 40	152.42 \pm 5.33	78.18 \pm 3.05	49.35 \pm 2.12	34.84 \pm 1.60	30.61 \pm 1.56	34.87 \pm 1.95
40 - 45	65.95 \pm 2.90	38.85 \pm 1.90	41.35 \pm 1.98	44.07 \pm 2.03	41.10 \pm 2.06	38.52 \pm 2.23
45 - 50	43.40 \pm 2.30	58.03 \pm 2.79	62.79 \pm 2.83	52.33 \pm 2.51	36.15 \pm 2.17	31.70 \pm 2.19
50 - 55	45.49 \pm 2.64	63.04 \pm 3.34	57.02 \pm 2.91	44.42 \pm 2.40	31.40 \pm 1.92	24.73 \pm 1.90
55 - 60	45.80 \pm 2.93	44.50 \pm 2.45	34.88 \pm 2.16	21.96 \pm 1.49	13.96 \pm 1.21	14.35 \pm 1.41
60 - 65	50.46 \pm 2.83	30.34 \pm 1.91	15.15 \pm 1.17	8.98 \pm 0.90	7.97 \pm 0.83	5.82 \pm 0.83
65 - 70	31.84 \pm 1.91	14.96 \pm 1.15	8.82 \pm 0.82	7.01 \pm 0.72	4.74 \pm 0.57	3.95 \pm 0.60
70 - 75	15.47 \pm 1.19	6.39 \pm 0.86	8.51 \pm 0.79	5.38 \pm 0.56	3.83 \pm 0.48	
75 - 80	7.05 \pm 0.76	4.88 \pm 0.65	4.88 \pm 0.55	3.33 \pm 0.43	1.94 \pm 0.33	
80 - 85	5.15 \pm 0.61	3.84 \pm 0.53	5.74 \pm 0.61	3.28 \pm 0.44		
85 - 90	6.79 \pm 0.77	8.16 \pm 0.80	5.38 \pm 0.59	2.11 \pm 0.38		
90 - 95	5.43 \pm 0.73	6.42 \pm 0.71	3.37 \pm 0.46	1.03 \pm 0.28		
95 -100	5.65 \pm 0.87	6.17 \pm 0.78	2.35 \pm 0.50	1.02 \pm 0.28		
100 -105	4.85 \pm 0.81	2.43 \pm 0.58	0.84 \pm 0.34			
105 -110	5.73 \pm 0.84	2.22 \pm 0.53	0.90 \pm 0.36			
110 -115	2.69 \pm 0.54	1.11 \pm 0.36				
115 -120						
120 -125						
125 -130						
130 -135						
135 -140						
140 -145						
145 -150						
150 -155						
155 -160						
160 -165						
165 -170						
170 -175						
175 -180						

Table 21: Integrated cross sections for ^{12}C and ^{40}Ca .

E_γ (MeV)	^{12}C	^{40}Ca
	σ (μb)	σ (μb)
135-140	3.83 ± 0.13	15.89 ± 0.56
140-145	15.21 ± 0.22	48.69 ± 3.09
145-150	41.68 ± 0.44	128.13 ± 1.95
150-155	60.53 ± 0.72	167.27 ± 2.49
155-160	112.67 ± 1.07	297.09 ± 3.66
160-170	146.31 ± 1.25	364.57 ± 3.96
170-180	212.75 ± 1.76	531.94 ± 5.45
180-190	315.20 ± 2.29	813.03 ± 6.93
190-200	358.66 ± 3.34	797.35 ± 8.47
200-220	483.18 ± 3.96	925.79 ± 9.32
220-240	575.67 ± 4.82	876.02 ± 17.37
240-260	526.47 ± 4.92	898.98 ± 9.95
260-280	522.86 ± 4.98	791.14 ± 8.62
280-300	446.44 ± 4.31	625.98 ± 6.90
300-320	338.52 ± 3.47	481.16 ± 5.76
320-340	264.27 ± 2.71	380.45 ± 4.92
340-360	179.16 ± 2.04	258.41 ± 3.97
360-380	165.54 ± 1.78	226.11 ± 3.65

B Derivation of formulae

B.1 The reconstructed pion mass

The total pion energy E_π can be written in terms of the pion mass m_π and the absolute value of the pion momentum p_π :

$$E_\pi = \sqrt{m_\pi^2 + p_\pi^2} \quad (43)$$

The pion momentum is, by momentum conservation, equal to the sum of the momenta of the pion decay photons:

$$\underline{p}_\pi = \underline{p}_1 + \underline{p}_2 \quad (44)$$

The absolute value of the pion momentum can be written as:

$$p_\pi = \sqrt{E_1^2 + E_2^2 + 2 E_1 E_2 \cos\psi} \quad (45)$$

where the absolute values of the photon momenta, which are the same as the photon energies, are E_1 and E_2 , and ψ is the opening angle between the pion decay photons in the lab.

The pion energy is, by energy conservation:

$$E_\pi = E_1 + E_2 \quad (46)$$

Combining equations 43, 45 and 46, m_π can be expressed as:

$$m_\pi = \sqrt{E_\pi^2 - p_\pi^2} \quad (47)$$

$$= \sqrt{(E_1 + E_2)^2 - (E_1^2 + E_2^2 + 2 E_1 E_2 \cos\psi)} \quad (48)$$

which can be rewritten as:

$$m_\pi = \sqrt{2E_1 E_2 (1 - \cos\psi)}. \quad (49)$$

B.2 The X formula

Using equations 43 and 45, the pion energy can be expressed as:

$$E_\pi = \sqrt{m_\pi^2 + E_1^2 + E_2^2 + 2 E_1 E_2 \cos\psi}. \quad (50)$$

Defining X as:

$$X = \frac{E_1 - E_2}{E_1 + E_2}, \quad (51)$$

the pion decay photon energies can be expressed in terms of X and E_π :

$$E_1 = \frac{E_\pi}{2}(1 + X) \quad (52)$$

$$E_2 = \frac{E_\pi}{2}(1 - X) \quad (53)$$

and substituting equations 52 and 53 into eq. 50, the X formula can be obtained:

$$E_\pi = \sqrt{\frac{2 m_\pi^2}{(1 - X^2)(1 - \cos\psi)}} \quad (54)$$

References

- [1] H. de Vries et al. Nuclear charge-density-distribution parameters from elastic electron scattering. *Atomic Data and Nuclear Data Tables*, 36, 495, 1987.
- [2] D. Drechsel et al. Medium Effects in Coherent Pion Photo- and Electroproduction on He-4 and C-12. *Nuclear Physics A660*, 423, 1999.
- [3] E. Oset and W. Weise. Photon-nucleus scattering and coherent π^0 photoproduction in the Δ -hole model . *Nucl. Phys.*, A402, 612, 1983.
- [4] R. A. Schrack et al. *Physical Review*, 127, 1772, 1962.
- [5] J. Lefrançois et al. Coherent Photoproduction of π^0 on Helium. *Il Nuovo Cimento*, 65A(333), 1969.
- [6] B. Bellinghausen et al. Measurement of coherent π^0 photoproduction on light nuclei in the P_{33} region. *Nucl. Phys.*, A358, 333, 1969.
- [7] B. Bellinghausen et al. Coherent π^0 Photoproduction on ^{12}C , ^{13}C and ^{16}O in the $\Delta(1232)$ Resonance Region. *Zeitschrift für Physik*, A309, 65, 1982.
- [8] A. S. Belousov et al. Photoproduction of π^0 mesons on complex nuclei at small energies in the region of the $\Delta(1232)$ resonance. *Sovjet Journal of Nuclear Physics*, 53, 379, 1991.
- [9] P. Argan et al. . *Phys. Rev.*, C21, 1416, 1980.
- [10] I. V. Glavanakov et al. Photoproduction of neutral pions on ^{12}C and ^6Li at threshold. *Phys. Lett.*, 178B, 155, 1986.
- [11] E. Mazzucato et al. Neutral pion photoproduction on carbon near threshold. *Phys. Lett.*, 185B, 25, 1989.
- [12] L. Jammes et al. Total cross section measurement on π^0 photoproduction near threshold on complex nuclei. *Phys. Lett.*, 227B, 21, 1989.

- [13] D. R. Tieger. Measurement of the Reaction ${}^4\text{He}(\gamma, \pi^0){}^4\text{He}$ for $e_\gamma = 290$ mev. *Phys. Rev. Lett.*, 53, 755, 1984.
- [14] V. Bellini et al. Coherent π^0 photo-production on ${}^4\text{He}$ at Intermediate Energies with Polarized Photons. *Nuclear Physics*, A646, 55, 1999.
- [15] F. Rambo et al. . *Nucl. Phys.*, A660, 69, 1999.
- [16] J. Arends et al. . *Zeitschrift für Physik*, A311, 367, 1983.
- [17] G. Koch et al. Cross Sections and Angular Distributions for ${}^{12}\text{C}(\gamma, \pi^0)$. *Phys. Lett. B* 218,2, 1989.
- [18] G. Koch et al. Differential Cross Sections for Coherent and Incoherent Neutral-Pion Photo-production from Calcium . *Phys. Rev. Lett.* 63,5, 1989.
- [19] M. Schmitz. *Experimentelle Untersuchung der Photoproduktion neutraler Pionen an C-12 im Bereich der Delta-Resonans*. PhD thesis, University of Mainz, Germany, 1996.
- [20] B. Krusche. Private communication.
- [21] K. S. Krane. *Introductory Nuclear Physics*. Wiley, 1988.
- [22] I. Blomquist and J. M. Laget. . *Nucl. Phys.* A280. 405-428, 1977.
- [23] S. Kamalov. Private communication.
- [24] W. O. Lock and D. F. Measday. *Intermediate Energy Nuclear Physics*. Methuen, 1970.
- [25] S. Boffi. *Electromagnetic Response of Atomic Nuclei*. Oxford University Press, 1996.
- [26] A. A. Chumbalov et al. . *Zeitschrift für Physik*, A328, 195-208, 1986.
- [27] D. Drechsel and O. Hanstein. Photoproduction of Pions - Results from Dispersion Theory. *Proc. of the Conference 'Perspectives in Hadronic Physics', Trieste, May 12-16, 1997*.

- [28] E. Oset and W. Weise. Photon-nucleus Scattering and Coherent π^0 Photo-production in the Δ -hole Model. *Nucl. Phys.*, A368, 375-393, 1981.
- [29] J. Ahrens et al. The Mainz Microtron MAMI: A facility portrait with a glimpse at first results. *Nuclear Physics News*, 4(2), 1994.
- [30] S. J. Hall et al. A Focal Plane System for the 855 MeV Tagged Photon Spectrometer at MAMI B. *Nucl. Instr. and Meth. in Phys. Research A*, A 368, 1996.
- [31] I. Anthony et al. Design of a tagged photon spectrometer for use with the Mainz 840 MeV microtron. *Nucl. Inst. Meth.* , A301, 230, 1991.
- [32] CRC. *Handbook of Chemistry and Physics*, 74th edition. 1993-94.
- [33] R. Novotny. Performance of the BaF₂ calorimeter TAPS. *Nuclear Physics B (Proc. Suppl.)*, 61B, 1998.
- [34] M. Röbig. Eichung des TAPS-Detektorsystems mit Höhenstrahlung. Master's thesis, University of Giessen, 1991.
- [35] A. R. Gabler. Ansprechverhalten des Detektorsystems TAPS für monochromatische Photonen im Energiebereich $E_\gamma = 50 - 780$ MeV. Master's thesis, University of Giessen, 1993.
- [36] V. Hejny. *Photoproduktion von eta-Mesonen an Helium 4*. PhD thesis, University of Giessen, 1998.
- [37] M. Pfeiffer. Private communication.
- [38] R. Sanderson. *Photo-production of Neutral Pions on O-16 and Pb-208*. PhD thesis, University of Glasgow, in preparation.
- [39] K. Molenaar. Performance of TAPS in the tagged photon beam of MAMI. Master's thesis, University of Groeningen, 1992.

- [40] Application Software Group, Computing and Networks Division, CERN. GEANT - Detector Description and Simulation Tool;
- [41] G. Koch. *Photoproduktion von neutralen Pionen an Kohlenstoff und Calcium im Bereich der Produktionsschwelle*. PhD thesis, University of Giessen, 1988.
- [42] T. Takaki et al. Photoproduction of Neutral Pions to Discrete Nuclear States. *Nuclear Physics A443* 570-588, 1985.
- [43] V. A. Tryasuchev and A. V. Kolchin. Inelastic photo-production of mesons on nuclei with γ deexcitation of the excited recoil nuclei. *Sov. J. Nucl. Phys.*, 54 (3), 1991.
- [44] F. James. Minuit - Function Minimization and Error Analysis, Reference Manual.
- [45] G.J.Miller and R.O.Owens. The Treatment of Data from a Neutral Meson Spectrometer. *Nucl. Instr. and Meth. in Phys. Research A*, 390, 257-266, 1997.
- [46] R. Sanderson. Private communication.

